Nonlinear optical techniques for ultrafast laser diagnostics

Development of femtosecond LIF, LIGS, CARS and backward lasing

Ruchkina, Maria

2021

Document Version:
Publisher's PDF, also known as Version of record

[Link to publication](#)

Citation for published version (APA):
Ruchkina, M. (2021). *Nonlinear optical techniques for ultrafast laser diagnostics: Development of femtosecond LIF, LIGS, CARS and backward lasing*. [Doctoral Thesis (compilation), Combustion Physics]. Department of Physics, Lund University.

Total number of authors:
1

Nonlinear optical techniques for ultrafast laser diagnostics

Development of femtosecond LIF, LIGS, CARS and backward lasing

MARIA RUCHKINA
DIVISION OF COMBUSTION PHYSICS | FACULTY OF ENGINEERING | LUND UNIVERSITY

Alignment of femtosecond Ti:Sapphire laser at Division of Combustion Physics, Lund University

LUND
UNIVERSITY

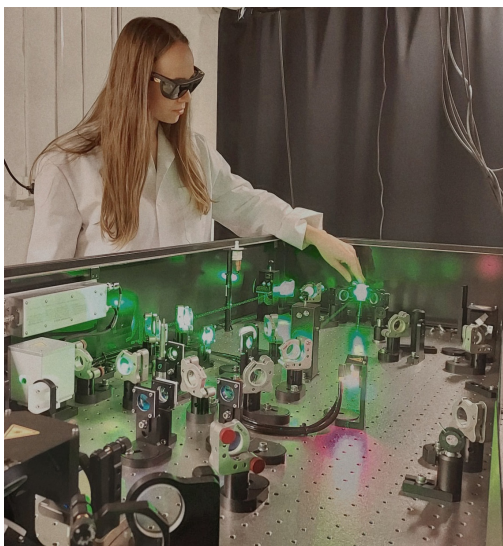Nonlinear optical techniques for ultrafast laser diagnostics

Nonlinear optical techniques for ultrafast laser diagnostics

Development of femtosecond LIF, LIGS, CARS and backward lasing

Maria Ruchkina

LUND
UNIVERSITY

Organization		Document name	
Organization LUND UNIVERSITY Division of Combustion Physics Department of Physics P.O.Box 118 SE-221 00 Lund, Sweden		**Document name** DOCTORAL DISSERTATION	
		Date of issue 2021-12-10	
		CODEN LUTFD2/TFCP-239-SE	
Author: Maria Ruchkina		Sponsoring organization	

Title and subtitle

Nonlinear optical techniques for ultrafast laser diagnostics. Development of femtosecond LIF, LIGS, CARS and backward lasing

Abstract

The thesis work concerns development and application of four versatile nonlinear optical techniques, based on exploiting ultrashort laser pulses, for diagnostic purposes in gases and flames. The four techniques, all laser-based, are two-photon laser-induced fluorescence (TPLIF), hybrid femtosecond/nanosecond (fs/ns) rotational coherent anti-Stokes Raman scattering (fs/ns RCARS), fs-laser-induced grating spectroscopy (fs-LIGS), and backward lasing. Special characteristics of fs-laser pulses, such as short pulse duration, high peak power even at low pulse energy, and broad spectral bandwidth, advance the development of these techniques to a new level.

In the TPLIF project, two-photon excited fluorescence of CO in CH_4/air flames was investigated and compared for ns, picosecond (ps), and fs-laser excitation. Moreover, based on fs-laser excitation, simultaneous interference-free two-photon excited fluorescence imaging of H and O atoms in turbulent flames was performed for the first time. In comparison with previous studies, it has been demonstrated that significantly larger measurement areas can be visualized in single-shot acquisitions.

A concept for lasing in the backward direction, facilitated by fs-laser excitation, was developed and demonstrated for range-resolved detection of H atoms in flames. The technique shows great potential for stand-off measurements in devices with only one optical access. On the fundamental level, studies were performed to uncover the physical mechanism responsible for the lasing effect.

With the developed hybrid fs/ns RCARS technique, the RCARS signal can be recorded with a high spectral and temporal resolution, simultaneously, allowing Raman linewidths to be measured on a single-shot basis. This capacity is of great importance for thermometry as it, in principle, eliminates the need for pre-knowledge about the chemical composition and availability of simulated linewidths. With increased fs-laser pulse energy, additional lines in the spectrum were observed due to Stark splitting.

The pioneering work on fs-LIGS was performed in heated flows of N_2 gas with temperatures varying from room temperature to 750 K. The thermal grating was formed by resonant multi-photon absorption, based on 800-nm fs pulses, and the generated LIGS signals were detected time-resolved in single-shot acquisitions. The results show that the method works very well for single-shot thermometry in nitrogen, with a measurement uncertainty of $\pm$ 1 K for room temperatures and $\pm$ 14 K for 600 K, as an example. Increasing the laser pump energy above a certain threshold causes ionization and generates a plasma density grating.

It is my hope and belief that the developed laser-based diagnostic techniques can contribute important tools for the larger research community in thermal energy conversion, and support the urgent transition to a sustainable energy system.

Key words: laser diagnostics, femtosecond laser, noninear interaction, ultrafast spectroscopy, multi-photon excitation, laser-induced fluorescnece, rotational coherent-Anti-Stokes Raman scattering, laser-induced grating spectroscopy, lasing, backward lasing

Classification system and/or index terms (if any)	
Supplementary bibliographical information	**Language:** English
ISSN and key title 1102-8781	**ISBN** 978-91-8039-075-0 (print) 978-91-8039-076-7 (pdf)
Recipient's notes	**Number of pages** 166	Price
	Security classification	

I, the undersigned, being the copyright owner of the abstract of the above-mentioned dissertation, hereby grant to all reference sources permission to publish and disseminate the abstract of the above-mentioned dissertation.

Signature _(signature)_   Date 2021-11-16

Nonlinear optical techniques for ultrafast laser diagnostics

Development of femtosecond LIF, LIGS, CARS and backward lasing

Maria Ruchkina

LUND
UNIVERSITY

Abstract

The thesis work concerns development and application of four versatile nonlinear optical techniques, based on exploiting ultrashort laser pulses, for diagnostic purposes in gases and flames. The four techniques, all laser-based, are two-photon laser-induced fluorescence (TPLIF), hybrid femtosecond/nanosecond (fs/ns) rotational coherent anti-Stokes Raman scattering (fs/ns RCARS), fs-laser-induced grating spectroscopy (fs-LIGS), and backward lasing. Special characteristics of fs-laser pulses, such as short pulse duration, high peak power even at low pulse energy, and broad spectral bandwidth, advance the development of these techniques to a new level.

In the TPLIF project, two-photon excited fluorescence of CO in CH_4/air flames was investigated and compared for ns, picosecond (ps), and fs-laser excitation. Moreover, based on fs-laser excitation, simultaneous interference-free two-photon excited fluorescence imaging of H and O atoms in turbulent flames was performed for the first time. In comparison with previous studies, it has been demonstrated that significantly larger measurement areas can be visualized in single-shot acquisitions.

A concept for lasing in the backward direction, facilitated by fs-laser excitation, was developed and demonstrated for range-resolved detection of H atoms in flames. The technique shows great potential for stand-off measurements in devices with only one optical access. On the fundamental level, studies were performed to uncover the physical mechanism responsible for the lasing effect.

With the developed hybrid fs/ns RCARS technique, the RCARS signal can be recorded with a high spectral and temporal resolution, simultaneously, allowing Raman linewidths to be measured on a single-shot basis. This capacity is of great importance for thermometry as it, in principle, eliminates the need for pre-knowledge about the chemical composition and availability of simulated linewidths. With increased fs-laser pulse energy, additional lines in the spectrum were observed due to Stark splitting.

The pioneering work on fs-LIGS was performed in heated flows of N_2 gas with temperatures varying from room temperature to 750 K. The thermal grating was formed by resonant multi-photon absorption, based on 800-nm fs pulses, and the generated LIGS signals were detected time-resolved in single-shot acquisitions. The results show that the method works very well for single-shot thermometry in nitrogen, with a measurement uncertainty of $\pm$ 1 K for room temperatures and

$\pm$ 14 K for 600 K, as an example. Increasing the laser pump energy above a certain threshold causes ionization and generates a plasma density grating.

It is my hope and belief that the developed laser-based diagnostic techniques can contribute important tools for the larger research community in thermal energy conversion, and support the urgent transition to a sustainable energy system.

Popular science summary

Nobel laureate and theoretical physicist, Richard Feynman once said that the test of all knowledge is experiment. Basically, we can simply test all the questions and doubts we have about the world or the nature and find out the "truth". One common knowledge is that everything is made of atoms, small particles wondering around and interacting with each other. Imagine looking in a glass of water, what do you see? A smooth transparent liquid and no traces of atoms. If you magnify it billon times you will see little groups of spheres representing hydrogen and oxygen atoms. Each group is called a molecule. We do not see these little groups with a naked eye because they are very small, atoms are approximately 10^{-8} cm in radius. To get an idea about how small an atom is you could make the following illustration – the relationship between the size of an atom and apple is the same as the relationship between the apple and the Earth. There are different sorts of apples as well as atoms, like apple "Golden" or "Granny Smith". In order to tell them apart it is enough to just look at them or even taste them, with atoms it is a little bit more complicated. One of the features atoms have which can sort them apart is energy states. Imagine a guitar string, a slight pluck at the string will give a low mode of vibration, the fundamental tone, which corresponds to a ground energy state. The higher the vibration frequency on the guitar string, the higher energy state. One thing I did not tell you about the atoms is that they have electrons, small seeds, like in an apple. These electrons do not sit still, they occupy different energy states of an atom. If you drop a bag of apples, it might have such a strong energy impact that some seeds (electrons) will jump up to a higher energy state. However, they cannot stay there forever, they have to go down and when they do so they may emit a photon of light, which has a specific fingerprint – a wavelength. Identifying this fingerprint is the way to tell the atoms apart.

What is a photon, or light or wavelength? Before the 20th century all the nature phenomena could be accurately explained by classical Newtonian physics. Though, it could not explain the interaction between the photons (particles forming light) and matter, which consists of atoms. Here we leave classical physics behind and meet the bizarre quantum physics. Light is a form of energy, which can be described by a colour, a wavelength. A red coloured object receiving the white light from the sun will reflect the red and absorb the other colours (which is why we perceive the object as red). Different colours of a light correspond to a different quantum of energy, or

frequency. Meaning that light with higher frequency will have higher energy. So blue or violet light has higher energy compared to red light.

Worldwide there is currently a big concern about the future of our environment. Complex chemical processes, involving the interaction of a large number of species (atoms and molecules), is behind the emission of pollutants and greenhouse gases. It is hence crucial to understand how the emissions are formed, since the pollutants might be hazardous for our health as well as lead to climate change, e.g., global warming. Based on such information we can gain knowledge and design more environmentally friendly sustainable combustion systems. The tricky thing with making good measurement in gases in practical devices, such as engines, is that it is often very difficult to get access to the volume of interest, and even if one could reach in with a measurement probe, like a thermometer, it would not work as it would perturb the chemistry and flow in the gas, or even melt, making the measurement more or less useless. Clearly, non-intrusive techniques that can measure remotely are needed. Present-day research makes it feasible with lasers. A very simple characterization of a laser is that it is a device that can produce a very intense and highly directional ray of light.

In this thesis, I used laser-based diagnostic methods to detect and image very reactive atoms and molecules in gases and flames. I was the first PhD student in the Combustion Physics Division to use a femtosecond (fs) laser for this purpose. If not Donna Strickland and Gérard Mourou, who got the Nobel Prise in 2018 for developing the technique which paved the way for today's powerful fs-lasers, I would not be here doing my PhD.

A femtosecond laser pulse obviously has ultrashort duration, which is equal to 10^{-15} seconds or $1/1\ 000\ 000\ 000\ 000\ 000$ of a second. Such ultrashort pulses have several unique features, which make them very attractive for research and applications. They allow measurements with exceptional temporal resolution, provide ultrahigh peak power, which is extremely advantageous for so-called nonlinear techniques, and the pulses are spectrally very broad (many colours in one pulse of light), allowing multiple species to be detected at the same time.

In the thesis I present four measurement techniques, which are based on the application of fs-laser pulses. All the techniques are nonlinear, in a sense that the induced signal depends nonlinearly on the applied electric field, which is provided by the intense laser pulse.

1. Laser-induced fluorescence (LIF) technique is a method used in the thesis project for detecting, measuring and imaging trace species with a laser beam tuned to an ultra-violet (UV) wavelength. The species measured were H and O atoms as well as the CO molecule.

2. The backward-lasing technique is a remote sensing technique and highlight of the thesis. We focused a UV laser beam in a gas and received a new beam

with a different colour emitted both in the forward and backward direction without using any mirrors (see Fig. I)! This new beam of light has very similar properties as a laser beam, i.e. coherent and directional, it carries the information about the constituent of the gas.

3. In the coherent anti-Stokes Raman scattering (CARS) technique three laser beams are focused and intersected in a gas, and the result of their nonlinear interaction with the molecules in the gas gives rise to a fourth laser-like signal beam. This beam carries information about the molecules in the gas, including the details about their speed of rotation, or rotational frequencies. This information has a direct connection to the temperature of the gas. With this technique the concentration of the gas can be measured as well.

4. The laser-induced grating spectroscopy (LIGS) technique is a little bit similar to CARS, here two fs-laser beams form a density grating in a gas. Afterwards, a third laser beam crosses the grating and reads out information about the temperature in the gas, and as a result we receive a fourth beam which carries the read information. This temperature measurement technique is also suited for high pressure environments.

At this moment, with all the freshly developed techniques based on fs-laser excitation we can "test" our knowledge about the environment and possibly make a positive impact. I hope these techniques will find their way to be further applied in physical and chemical science, atmospheric research as well as in industry. Although the techniques developed in this project require quite heavy and sizeable equipment, the rapid technical development and intense research makes it possible to envision portable devices for remote sensing with backward lasing concept within a decade or so.
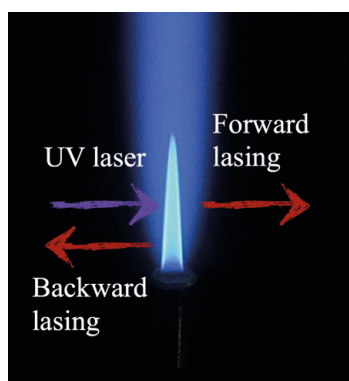

Figure I. Representation of forward and backward propagating laser beams created in a flame by the UV laser beam.

Populärvetenskaplig sammanfattning*

Nobelpristagaren och teoretiska fysikern Richard Feynman, har en gång sagt att måttstocken för all kunskap är experimentet. Enkelt uttryckt, allt vi behöver göra är att experimentellt pröva de frågor och tvivel vi har om världen och på så sätt finna "sanningen".

De flesta känner till att världen är uppbyggd av atomer, oerhört små partiklar som interagerar med varandra. Tänk dig ett glas med vatten, varför ser du en genomskinlig vätska men inte ett spår av atomer när du tittar på det? Först om vi förstorade glaset ungefär en miljard gånger skulle vi börja se små grupper av partiklar, uppbyggda av sfärer som representerar atomer av väte och syre. Tillsammans bildar de vattenmolekyler. För att förstå hur liten en atom är (bara ungefär 10^{-8} cm i radie) kan vi göra följande jämförelse, relationen i storlek är ungefär den samma mellan en atom och ett äpple som mellan ett äpple och jordklotet. Liksom för äpplen finns det atomer av olika sorter, vill vi skilja på ett Golden Delicious och ett Granny Smith så räcker det med att titta och kanske smaka. Med atomer blir det lite mer komplicerat, en egenskap atomer har som gör det möjligt för oss att faktiskt skilja dem åt är något som kallas energinivåer. Tänk er en gitarrsträng som sätts i svängning, en knäpp på strängen ger en lågfrekvent vibration, en grundton som kan liknas vid atomens grundenerginivå. En mer högfrekvent ton motsvarar en högre energinivå. En atom har även något som kallas elektroner. Elektronerna sitter inte still utan befinner sig i olika distinkta energinivåer (omloppsbanor) i atomen. Om atomen utsätts för en stöt stor nog, likt om du tappar en påse äpplen i golvet från tillräckligt högt upp, kan några elektronerna "hoppa upp" till en högre energinivå. De kan dock inte stanna på denna högre energinivå för alltid utan kommer att "ramla" tillbaka till grundnivån, och när detta sker kan ljus sändas ut, en foton, som bär med sig ett unikt fingeravtryck - våglängden på ljuset. Genom att studera detta fingeravtryck kan vi skilja atomer från varandra.

Vad är då en foton, ljus och våglängd? Före 1900 talet förklarades alla observerade naturliga fenomen med klassisk (Newtons) fysik. Teorin kunde dock inte förklara interaktionen mellan fotoner (ljuspartiklar) och materia, som alltså består av atomer. Här lämnar vi klassisk fysik bakom oss och möter kvantfysikens bisarra värld. Ljus är en form av energi och kan beskrivas av en färg eller, mer specifikt, en våglängd.

---

* Översättning av Robert Berglund och Joakim Bood

När ett objekt som vi uppfattar som rött, t.ex. ett glas rödvin, träffas av vitt ljus, som innehåller alla färger, kommer de röda våglängderna att transmitteras medan de andra färgerna absorberas vilket alltså är anledningen till att vi uppfattar vinet som rött. Det är alltså den specifika sammansättningen av molekyler i vinet som då de belyses med synligt ljus gör att det får sin specifika färg. Olika färger av ljus motsvarar olika kvanta av energi eller frekvens. Ljus med högre frekvens har högre energi, vilket svarar mot blå/lila ljus, vilket har högre frekvens och därmed även högre energi än rött ljus.

Världen idag präglas av stor klimatoro. Komplexa kemiska processer som innefattar ett mycket stort antal olika atomer och molekyler ligger bakom utsläpp av föroreningar och växthusgaser. Kunskap om hur utsläpp bildas är därför mycket viktigt eftersom föroreningar kan vara skadliga för hälsan och bidrar till växthuseffekten. Med sådan kunskap kan vi t.ex. utveckla mer miljövänliga och hållbara förbränningsprocesser.

För traditionella mättekniker finns ofta två betydande begränsningar/svårigheter. Dels påverkar en fysisk mätprob, t.ex. ett termoelement, själva mätobjektet, vilket för mätning i gaser innebär att gasflöde och kemiska processer förändras. Detta leder till otillförlitliga, i vissa fall gravt felaktiga, mätresultat. Den andra stora begränsningen är att mätområdet kan vara så svårtillgängligt att mätproben inte kan appliceras. Dessa begränsningar motiverar utveckling av laserbaserade mättekniker. Sådana tekniker kan nämligen erbjuda beröringsfria mätningar och om det finns så kallad optisk access, dvs ett hål eller ett fönster på mätobjektet, kan mätningar göras precis i det område där processen man vill undersöka sker.

En mycket förenklad beskrivning av en laser är att det är en apparat som kan producera en riktad sammanhållen ljusstråle med hög intensitet.

I detta avhandlingsarbete har jag utvecklat och tillämpat ett antal olika laserbaserade mättekniker för att detektera och visualisera förekomsten av väldigt reaktiva atomer och molekyler i olika gaser och laboratorieflammor. Jag var den första doktoranden vid Avdelningen för Förbränningsfysik som utnyttjade en femtosekundlaser (fs) för detta ändamål. Om det inte vore för Donna Strickland och Gerard Mourou, som tilldelades Nobelpriset i fysik 2018 för utvecklandet av tekniken som banade väg för dagens kraftfulla fs-lasrar, hade jag inte kunnat doktorera i detta ämne.

En femtosekund-laser genererar laserpulser som har extremt kort pulslängd. En femtosekund (fs) är lika med 1/1 000 000 000 000 000 sekund och den fs-laser som använts i detta arbete har en pulslängd på ca 100 fs. Den korta pulslängden ger upphov till en rad unika egenskaper hos pulserna, vilket gör dem mycket attraktiva inom många olika forskningsområden och tillämpningar. Dessa ultrakorta pulser gör det t.ex. möjligt att studera fenomen med exceptionell tidsupplösning. På grund av att pulserna är ultrakorta har de väldigt hög toppeffekt, vilket är mycket viktigt i så kallade icke-linjära tekniker. Dessutom är fs-pulserna väldigt breda spektralt, det

vill säga en puls innehåller ett ganska brett spektrum av färger, vilket i sin tur möjliggör växelverkan med många olika ämnen (atom/molekyl) samtidigt.

I avhandlingen presenteras och diskuteras fyra olika mättekniker baserade på fs-laserpulser. Samtliga tekniker är ickelinjära, i det avseendet att den inducerade mätsignalen beror ickelinjärt på det pålagda elektriska fältet, vilket i det här fallet utgörs av en ultrakort laserpuls av hög intensitet. Nedan summeras, mycket kortfattat, dessa fyra mättekniker.

1. Två-foton laserinducerad fluorescence (LIF) är en teknik som utvecklats och använts för detektion och visualisering av några spårämnen av stor betydelse i förbränning och atmosfärskemi, nämligen väteatomer (H), syreatomer (O) och kolmonoxid (CO). Alla dessa tre ämnen har sina starka energinivåövergångar i det vakuumultravioletta (VUV) området, vilket är anledningen till att två-fotonexcitation används.

2. Bakåtriktad lasring är en ny mätteknik som utvecklats för fjärranalys. I korthet går den teknik ut på att en fs-laserpuls i UV-området fokuseras i en gas och om våglängden matchar en resonans hos en atom eller molekyl kan en ny laserliknande stråle, med en färg specifik för den aktuella atomen/molekylen, genereras både i framåt- och bakåtriktningen (se Fig. II). Genom att detektera den bakåtriktade ljusstrålen med hög tidsupplösning kan närvaron av ett visst ämne (atomer) lokaliseras, även på ett avstånd av flera meter. Detta resultat utgör en av avhandlingsarbetets höjdpunkter.

3. I tekniken koherent anti-Stokes Ramanspridning (CARS) korsas tre fokuserade laserstrålar i en gas, resultatet av deras ickelinjära interaktion med molekylerna i gasen ger upphov till en ny laserlik signalstråle. Signalstrålen bär information om molekyler i gasen, inklusive deras rotationsfrekvenser. Denna information är direkt knuten till gasens temperatur och tekniken kan därmed användas för termometri. I detta arbete har tekniken vidareutvecklats genom att kombinera fs-laserpulser med en nanosekundlaserpuls och detektera den våglängdsupplösta signalen med en ultrasnabb kamera (streakkamera).

4. Laserinducerad gitterspektroskopi (LIGS) är teknik som i viss mån är lite lik CARS, så till vida att laserstrålar korsas och att signalen kommer i form av en koherent stråle. I fs-LIGS, som här utvecklats, formar två korsade fs-laserstrålar ett densitetsgitter i gasen. En tredje, kontinuerlig, laserstråle infaller mot gittret, varpå en fjärde stråle skaps som bär information om gasens egenskaper, t.ex. dess temperatur. De erhållna resultaten demonstrerar att tekniken kan användas för termometri i gas fas. Tekniken har även en god potential för mätning i miljöer med högt tryck.

Med dessa nya eller vidareutvecklade mättekniker baserade på fs-laserexcitation adderas nya/förbättrade möjligheter att diagnosticera olika fysikaliska och kemiska processer. Utöver tillämpningar inom förbränningsforskningen, är det min

förhoppning och övertygelse att dessa tekniker även kommer vara av betydande värde för forskning och tillämpningar inom andra vetenskapliga områden, såsom grundforskning inom fysik och kemi, och atmosfärsvetenskap, men även för industriella tillämpningar. Utrustningen som krävs för dessa tekniker är i dagsläget relativt tung och skrymmande. Med den snabba tekniska utvecklingen, i kombination med intensiv forskning, är det dock inte orimligt att föreställa sig portabla varianter av teknikerna inom något årtionde.
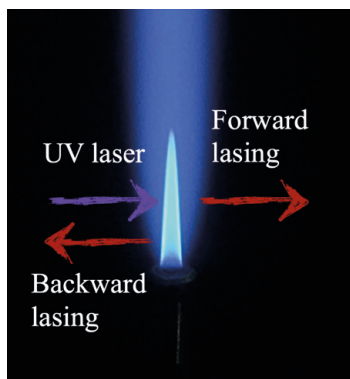

Figure II. Representation av framåt- och bakåtriktad laser ljusstrålarna generterad i laboratorium flamma av UV-laserstrålen.

List of papers

I.   **M. Ruchkina**, P. Ding, M. Aldén, J. Bood and C. Brackmann. Two-photon-excited fluorescence of CO: experiments and modelling
Optics express 27 (18), 25656-25669, 2019

II.   P. Ding, **M. Ruchkina**, Y. Liu, M. Alden, J. Bood. Femtosecond two-photon-excited backward lasing of atomic hydrogen in a flame
Optics letters 43 (5), 1183-1186, 2018

III.   P. Ding, **M. Ruchkina**, Y. Liu, M. Alden, J. Bood. Gain mechanism of femtosecond two-photon-excited lasing effect in atomic hydrogen
Optics letters 44 (9), 2374-2377, 2019

IV.   **M. Ruchkina**, P. Ding, A. Ehn, M. Aldén, J. Bood. Single-shot, spatially-resolved stand-off detection of atomic hydrogen via backward lasing in flames
Proceedings of the Combustion Institute 37 (2), 1281-1288, 2019

V.   A. Hosseinnia, **M. Ruchkina,** P. Ding, P-E. Bengtsson, J. Bood. Simultaneous temporally and spectrally resolved Raman coherences with single-shot fs/ns rotational CARS
Optics Letters 45 (2), 308-311, 2020

VI.   **M. Ruchkina**, D. Hot, P. Ding, A. Hosseinnia, P-E. Bengtsson, Z. Li, J. Bood, A-L. Sahlberg. Laser-induced thermal grating spectroscopy based on femtosecond laser multi-photon absorption
Scientific Reports 11 (1), 1-13, 2021

Related work

VII.   P. Ding, **M. Ruchkina**, D. Del Cont-Bernard, A. Ehn, DA. Lacoste, J. Bood. Detection of atomic oxygen in a plasma-assisted flame via a backward lasing technique.
Optics letters 44 (22), 5477-5480, 2019

VIII.   D. Del Cont-Bernard, **M. Ruchkina,** P. Ding, J. Bood, A. Ehn, DA. Lacoste. Femtosecond two-photon laser-induced fluorescence imaging of atomic hydrogen in a laminar methane–air flame assisted by nanosecond repetitively pulsed discharges.
Plasma Sources Science and Technology 29 (6), 065011, 2020

IX.   P. Ding, **M. Ruchkina**, D. Del Cont-Bernard, A. Ehn, DA. Lacoste, J. Bood. Temporal dynamics of femtosecond-TALIF of atomic hydrogen and oxygen in a nanosecond repetitively pulsed discharge-assisted methane–air flame.
Journal of Physics D: Applied Physics 54 (27), 275201, 2021

X.   A. Hosseinnia, **M. Ruchkina**, P. Ding, J. Bood, P-E. Bengtsson. Single-shot fs/ns rotational CARS for temporally and spectrally resolved gas-phase diagnostics.
Proceedings of the Combustion Institute 38 (1), 1843-1850, 2021

XI.   P. Ding, C. Brackmann, **M. Ruchkina**, L. Wang, L. Yuan, Y. Liu, B. Hu and J. Bood. Femtosecond laser-induced quantum beating superfluorescence of atomic oxygen in flame.
Physical review A 104, 033517, 2021

XII.   P. Ding, **M. Ruchkina,** Z. Wang and J. Bood. Signature of femtosecond laser-induced superfluorescence from atomic hydrogen in flames.
Submitted to Physical review A, October 2021

Summary of papers

Paper I

Two-photon-excited fluorescence of CO: experiments and modelling

M. Ruchkina, P. Ding, M. Aldén, J. Bood and C. Brackmann. *Optics express 27 (18), 25656-25669, 2019*

The excitation with transform-limited fs-laser pulses provide photolytic interference free fluorescence measurements. Two-photon excited fluorescence of CO molecule was measured in CH_4/air flame. A model based on rate-equation analysis of four energy levels of carbon monoxide (CO) molecule has been developed. Experimental and simulated fluorescence signals of CO have been compared for laser excitation pulses emitting in nano-, pico- and femtosecond regime; they showed good quantitative agreement. Overall, the developed model has a potential to be applied to arrange suitable diagnostic configurations and retrieve quantitative data.

I prepared and performed the experiment with the femtosecond laser excitation together with Christian Brackmann and Pengji Ding, together we recorded the excitation spectra, emission spectra and the fluorescence profiles of CO molecule. I performed the analysis of the received data together with Christian Brackmann and Joakim Bood. In the manuscript I contributed to the results section and described the experimental setup for the femtosecond laser experiment. I took part in the revision of the manuscript as well.

Paper II

Femtosecond two-photon-excited backward lasing of atomic hydrogen in a flame

P Ding, M Ruchkina, Y Liu, M Alden, J Bood. *Optics letters 43 (5), 1183-1186, 2018*

In this paper, the concept of a backward lasing technique in flame has been developed and introduced for the first time. A bi-directional lasing at 656 nm of H atom has been observed in a premixed CH_4/air flame. A backward propagating beam

has been characterized temporally and spatially. The presence of the lasing threshold was discovered. The divergence of the backward lasing beam was estimated to approximately 17 mrad and the lasing laser pulse energy was estimated to approximately 27 pJ, while the duration of the backward lasing pulse was estimated to 20 ps for the current conditions. Altogether, the experiment has shown that a backward lasing technique has a great potential for single-ended diagnostics.

I took part in the performance of all the experimental campaign with Pengji Ding and did some data analysis. I took part in reviewing the manuscript and discussing the ideas. I have also presented the work at CLEO (Laser Science to Photonic Applications) conference in 2018.

Paper III

Gain mechanism of femtosecond two-photon-excited lasing effect in atomic hydrogen

P. Ding, <u>M. Ruchkina</u>, Y. Liu, M. Alden, J. Bood. *Optics letters 44 (9), 2374-2377, 2019*

The physical mechanism behind the backward lasing technique has been revealed. It has been proposed that amplified spontaneous emission takes place. Gain dynamics of the backward lasing have been studied, the spectra of the forward and backward lasing have been compared. The optical gain coefficient was measured by injecting a seeding pulse into the gain region. The gain coefficient is equal to 52 cm^{-1}. By varying the temporal delay between the seed pulse and the pump laser pulse the lifetime of the gain was revealed to last for approximately 3.5 ps (FWHM). The forward lasing has a one order of magnitude stronger intensity and broader spectrum compare to the backward lasing.

I took part in the performance of all the experimental campaign with Pengji Ding and did some data analysis. I took part in reviewing the manuscript.

Paper IV

Single-shot, spatially-resolved stand-off detection of atomic hydrogen via backward lasing in flames

<u>M. Ruchkina</u>, P. Ding, A. Ehn, M. Aldén, J. Bood. *Proceedings of the Combustion Institute 37 (2), 1281-1288, 2019*

The paper presents an experimental demonstration of single-shot, spatially-resolved stand-off detection of atomic hydrogen in flame. The method has been demonstrated

in two CH_4/O_2 jet flames, where the spacing between the flames has been varied; and in a single flame. The highest temporal resolution of 1.65 nm has been obtained. The backward lasing signal has been compared and qualitatively agreed with two-photon side fluorescence.

I was main responsible for the experiment and the paper. I and Pengji Ding participated together in the experimental campaign and we performed the data analysis. I prepared the figures for the manuscript with the help of Andreas Ehn. All the authors contributed to writing and revising the manuscript. I have also presented the work at 37th International Symposium on Combustion in 2018.

Paper V

Simultaneous temporally and spectrally resolved Raman coherences with single-shot fs/ns rotational CARS

A. Hosseinnia, M. Ruchkina, P. Ding, P-E. Bengtsson, J. Bood. *Optics Letters 45 (2), 308-311, 2020*

The concept of using fs/ns configuration for studying the molecular coherences in rotational CARS has been demonstrated for the first time. It has been shown that the full temporal and spectral evolution of Raman coherences can be observed in a single-shot basics. While demonstrating the technique in N_2 gas and air new interesting phenonium like Stark effect and frequency beating arose.

I participated in infinite aligning and taking the experimental data together with Ali Hosseinnia and Pengji Ding. I took part in numerous discussions with all the authors. I designed the experimental setup figure and described the experimental part in the manuscript. I took part in reviewing the manuscript.

Paper VI

Laser-induced thermal grating spectroscopy based on femtosecond laser multi-photon absorption

M. Ruchkina, D. Hot, P. Ding, A. Hosseinnia, P-E. Bengtsson, Z. Li, J. Bood, A-L. Sahlberg. *Scientific Reports 11 (1), 1-13, 2021*

Femtosecond laser-induced thermal grating spectroscopy (LITGS) has been observed in a configuration based on crossing two 800 nm femtosecond laser beams and continuous-wave 532 nm beam. The concept has been investigated in a configuration based on multi-photon absorption, which up to now has only been realized with resonant excitation using narrowband lasers. Fluorescence studies

have been performed in order to investigate possible multi-photon absorption pathways. The feasibility of the technique has been investigated in a heated N_2 gas flow with temperatures varying from 295 to 750 K. The experimental results have been well supported by modelled signals. Measurements have been performed in Argon gas and air as well.

I was the main coordinator and executer for the experiment. I performed the experiment together with Dina Hot, Pengji Ding and Anna-Lena Sahlberg. I carried out the simulations and analysed the data with assistance of Dina Hot and Joakim Bood. I took part in numerous discussions with all the authors. I wrote most part of the manuscript and produced most of the figures. I took part in reviewing the manuscript. I have also presented the work at online Gordon Research Conference (GRC Connects) on Laser Diagnostics in Energy and Combustion Science in July 2021 while being a co-chair for the conference.

*In all the aforementioned papers I was the main responsible for the performance of the femtosecond laser system.

Table of Contents

1 Introduction and motivation

The Earth's climate is a complex system, its components are changing drastically, small deviations in initial values can result in huge differences at a later stage. This year's Nobel Prize laureates in Physics Syukuro Manabe and Klaus Hasselmann demonstrated through their research that the increased concentration of carbon dioxide (CO_2) in the atmosphere leads to increased temperature on Earth, and it has also been proved that human activities have a huge impact on the carbon dioxide emissions in the atmosphere [1]. Yet, CO_2 comprises a very small portion of the Earth's atmosphere, only around 0.04%, then how can it have such a huge impact on the climate? Carbon dioxide can absorb the Earth's infrared radiation and release the absorbed energy, heating up the surrounding atmosphere. If the level of carbon dioxide is doubled, the Earth's temperature might be increased by 2℃ [1]. Conversely, a decrease of the carbon dioxide level in the atmosphere will lead to a temperature drop. To have a stable temperature in the atmosphere, it is important to have an energy balance between the sun's radiation towards the ground and the radiation from the ground. According to NOAA's 2020 Annual Climate Report the global land and ocean surface temperature has been raised by 1℃ over the past 150 years [2]. Both natural and human sources contribute to the changes in the atmosphere according to Klaus Hesselmann's research work.

We can reduce our impact by making a transition to a sustainable society as stipulated by the global sustainable development goals of AGENDA 2030 [3] and the Paris agreement on climate change, i.e. to keep the global temperature increase below 1.5 °C [4]. Environmental sustainability of energy systems represents the transition from fossil fuel-based energy systems towards renewable form of energy systems. This means that there is a need for development of cleaner energy systems that reduce hazardous emissions and pollutions. Bioenergy, for example, is one type of renewable energy, generated while burning biomass fuel. However, the use of the wood in a biomass power plant contributes to deforestation. Therefore, further development of renewable alternatives from, e.g., biomass, ammonia or metal combustion, is needed. Combustion is a process characterized by complex chemistry, involving various thermal conversion processes. Knowledge about it is essential for increasing the efficiency of combustion processes and lowering emissions of pollutants. This requires techniques that can measure atomic and molecular concentrations and temperatures non-intrusively with high spatial and temporal resolution, sometimes in geometries with limited optical access. These

requirements are met by laser-based diagnostic techniques. The research on laser-based diagnostic techniques can be divided into two different areas: (1) development of new techniques, which can enable completely new information to be extracted, but also complement or improve already existing laser-based diagnostic techniques, and (2) application of the excising techniques for direct measurements in the atmosphere or combustion environment.

Focus of the present work

The motivation of the thesis work is to make a contribution to the cutting-edge research towards a sustainable energy system, by developing novel laser-based diagnostic techniques for measuring temperature and minor species concentrations in the atmosphere and combustion environments. During the thesis project four different nonlinear techniques based on exploiting ultrashort femtosecond (fs) laser pulses were developed. Ultrashort laser pulses possess a number of attractive diagnostic features like exceptional temporal resolution, extreme peak power and broad spectral coverage. A state-of-the-art Ti:Sapphire laser system, providing pulses of 125-fs duration, at 800-nm wavelength, at a pulse repetition rate of 10 Hz, pumps two tuneable optical parametric amplifiers, providing fs laser pulses with a wavelength tunability in the range from 190 to 1600 nm. This laser system is utilized to pursue (a) two-photon laser-induced fluorescence (TPLIF), (b) coherent-anti-Stokes Raman scattering (CARS), (c) laser-induced grating spectroscopy (LIGS) and (d) backward lasing techniques.

Two-photon laser-induced fluorescence is a technique based on a selective absorption of two laser photons followed by emission of fluorescence. The combination of high peak power and low pulse energy of the fs laser provides efficient excitation, while effectively reducing interfering processes like photolysis. This scheme provides improved measurement accuracy. Many chemical species, which are of great importance in combustion and atmospheric research, have their absorption resonances in the vacuum ultraviolet (VUV) regime (wavelength < 200 nm), and hence the radiation needed to excite these species is absorbed by the atmosphere. However, using two photons, with wavelengths above 200 nm, mitigates this problem. The technique was applied for measuring the relative concentrations of hydrogen and oxygen atoms on a single-shot basis in turbulent flames.

The chemistry of biomass-derived renewable fuels, having complex chemical compositions, implies that carbon monoxide CO is present as a key intermediate species. Femtosecond two-photon LIF was also developed and applied for quantitative measurements of CO concentrations. The experimental results provide

a good foundation for developing a model, which is designed for understanding the optimal diagnostic arrangement for measuring CO and other species in combustion.

Backward-lasing is the concept of a mirror-less remote laser with a constituent of the ambient gas as active medium. The fs laser was used to drive a two-photon pumping for stand-off measurements of H atoms in flames. It is demonstrated that temporally-resolved backward lasing signals from H atoms provide detection with high (millimetre-range) spatial resolution. This result is very promising and further development could potentially revolutionize the remote-sensing field. Possible physical mechanisms responsible for the lasing mechanism were investigated in the thesis work as well.

Coherent-Anti-Stokes Raman scattering is an established diagnostic technique for temperature and concentration measurements in combustion-related environments. In this work a novel concept is developed for probing rotational Raman coherences, simultaneously spectrally and temporally resolved, in nitrogen and air on a single-shot basis, by employing fs-laser pulses for the excitation and nanosecond (ns) laser pulses for probing, hence the name hybrid fs/ns rotational CARS.

Laser-induced grating spectroscopy is utilized for measuring thermodynamic properties of the medium. The idea of the technique is based on creating a density grating in the medium using two crossed fs-laser pulses and probing its dynamics with another continuous-wave laser beam. Employing fs-laser excitation it is possible to create a thermal grating through multi-photon absorption. The temperatures measured with this technique in the thesis work range from room temperature up to 750 K.

Thesis outline

The primary goal of the thesis work is a demonstration of the feasibility of the aforementioned fs-laser excitation-based techniques as measurement tools for both fundamental studies and remote non-intrusive diagnostics of various gaseous environments. Chapter 2 covers a theoretical description of the nonlinear process of multi-photon excitation. Chapter 3 gives an introduction to the nonlinear diagnostic techniques, namely TPLIF, Lasing, hybrid fs/ns-CARS and fs-LIGS. The concepts connected with the use of fs-laser pulse excitation are discussed as well. Chapter 4 expands and complements the results presented in papers I-VI with some experimental and theoretical discussions. Finally, chapter 5 summarizes the results and gives some future perspectives of the discussed diagnostic techniques. A femtosecond laser based on the chirped-pulse amplification (CPA) technique is utilized, for the first time in the Lund group, during this thesis project, and is described in detail in appendix A. This chapter describes the optical parametric amplification and frequency mixing systems as well.

2 Nonlinear excitation processes

In a quantum-mechanical system, an atom/molecule can have its electrons take definite energy values, called energy levels. If an atom/molecule gets excited by an external energy source it drives electrons to a higher lying energy level. Electrons occupying one high lying energy level cannot remain there forever. Sooner or later the atom/molecule has to deexcite and the electron falls down to the lower energy level, and sometimes it results in radiation of a photon in the form of light. Unless the level, the electrons ended up at is virtual, or in other words "imaginary", and, as long as the population stays there for enough time to absorb another photon generated by an external energy source it can get to an even higher energy level. This interpretation is true for the multi-photon absorption process which allows the transitions to the energy levels not accessible by one photon. In combustion diagnostics many species of interest have their resonances way down in the vacuum ultraviolet, unfortunately, these wavelengths get absorbed by the atmosphere or by the combustion gases. To mitigate this problem multi-photon excitation schemes have been applied.

Lifetime of a virtual level

In the thesis project all the diagnostic techniques undergo non-linear excitation involving one or more virtual levels (virtual states). However, the knowledge of the exact position of the virtual level (or exact measurement of the energy), or its lifetime is not possible according to the uncertainty principle. One thing we do know about virtual levels, however, is that they are located next to the real energy levels.

To shed more light on the "lifetime" of a virtual state, a two-photon absorption process is considered as illustrated in Fig. 2.1a. In this figure $|g\rangle$ is the ground state, $|e\rangle$ is the upper energy state at which the two-photon absorption terminates, $|v\rangle$ is a virtual state and $|m\rangle$ is an intermediate real state, which is located in the vicinity of the virtual state. When a photon of frequency ω_1 illuminates an atom/molecule, the atom/molecule is excited to the virtual state $|v\rangle$. Then, the atom/molecule may absorb another photon, of frequency ω_2, and get to the upper energy state $|e\rangle$ (excited state), but this requires that the second photon ω_2 arrives in a short enough time so that the atom /molecule excited by the first photon still remains in the virtual

state $|v\rangle$. If it takes too long time until the second photon arrives, the upper state $|e\rangle$ will not be reached.
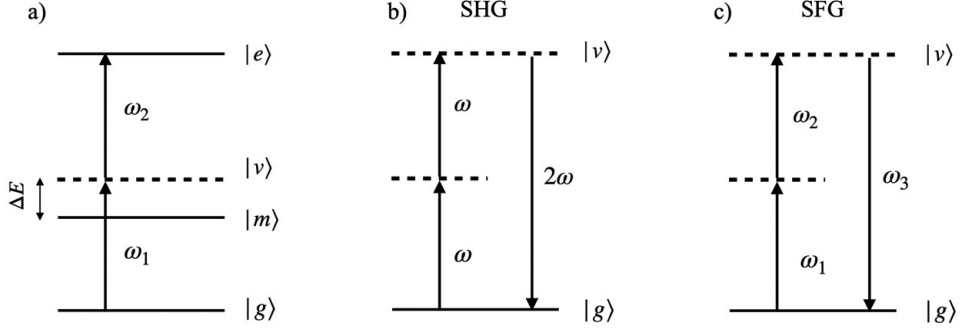

Figure 2.1. a) Energy level diagram decribing two-photon absorption process (nonparametric). Energy level diagram describing b) second-harmonic generation (SHG) and c) sum-frequency genertaion (SFG) as a parametric a process.

The occupation time period of the virtual state $|v\rangle$ is given by the energy-time Heisenberg uncertainty principle:

$$\Delta E \cdot \Delta t \geq \frac{\hbar}{2},$$

where $\hbar = h/2\pi$, h is the Planck constant, and ΔE is the energy difference between the virtual level $|v\rangle$ and nearest real energy level $|m\rangle$. It means that the second photon should arrive to the virtual level in the time period $\Delta t = \frac{\hbar}{2\Delta E}$.

If the virtual state is located close to a real energy state, then the lifetime of the virtual state is relatively long because ΔE is small, which means that there will be more time available for the second photon ω_2 to arrive in time. High intensity fs-laser pulses, as employed in this thesis project, are beneficial for driving two-photon transitions via virtual levels since they provide very high photon flux in each pulse, which increases the probability for the second photon ω_2 to be absorbed, and thus the efficiency of the two-photon excitation process.

Two-photon absorption

It should be noted that in the two-photon absorption process, as illustrated in Fig. 2.1a, an atom/molecule transfers the population from the ground state to the excited state by quasi-simultaneous absorption of two photons. Thus, the two-photon atomic transition rate scales with the square of the laser intensity I^2 [5]

as $W_{ge} = \frac{\alpha_{ge} I^2}{\hbar \omega}$, where α_{ge} describes the strength of two-photon absorption transition $|g\rangle \rightarrow |e\rangle$. The energy difference between the ground and excited state is equal to the sum of energies of the two photons absorbed. Thus, the fluorescence signal resulting from a two-photon excitation process scales as the square of the laser intensity. Analogously, for an eight-photon excitation process, it will be proportional to $\sim I^8$ (paper VI). As already alluded to, high-intensity fs-laser pulses are beneficial for driving nonlinear processes, such as multi-photon absorption.

It should be noted that from a diagnostical point of view, when performing two-photon excitation laser-induced fluorescence experiments, the laser beam is typically focused in a region of interest; meaning that the fluorescence signal will be maximum at this point and decrease with increasing distance from the focus. This is in stark contrast to one-photon excitation, where the fluorescence signal intensity is independent of the laser focusing.

Parametric and nonparametric processes

In a parametric process the initial and final quantum-mechanical states are identical. Two examples of parametric processes are shown in Fig. 2.1b and Fig. 2.1c. The opposite process is called nonparametric, in which the population is transferred from the ground state $|g\rangle$, to another real energy state $|e\rangle$, as shown in Fig. 2.1a. Multi-photon excitation is an example of such a process. The fundamental difference between the two processes is illustrated in Fig.2.1. Coherent-anti Stokes Raman scattering (CARS), studied in the thesis work (paper V), is an example of a parametric process, as can be seen in the energy-level diagram shown in Fig. 3.12.

Second-harmonic generation (SHG) is another example of a parametric process, where power of an incident beam ω is transferred to radiation at the doubled frequency, 2ω, i.e., the second harmonic. An energy-level description of SHG is shown in Fig. 2.1b. Sum-frequency generation (SFG) is another example of a parametric process, similar to SHG, where the power of two incident photons of different frequencies ω_1 and ω_2 is converted into radiation at the sum-frequency $\omega_3 = \omega_1 + \omega_2$. An energy-level description of SFG is shown in Fig. 2.1c. Both SHG and SFG processes are employed in the fs-laser system (appendix A) used in the thesis project, for more description of these processes the reader is referred to [6].

3 Diagnostic techniques

During the last couple of years ultra-short-pulsed lasers have been widely applied for different diagnostic methods due to their extreme peak power, broad spectral selectivity, and ultra-short pulse duration. In our laboratory we have also utilized a state-of-the-art fs-laser system (see a broader description of the system in appendix A) for developing spectroscopic diagnostic techniques [5]. The aim of this chapter is to give a brief description of these concepts. Laser-induced fluorescence (LIF) was used to visualize and, in some cases, quantitatively measure the concentration of carbon monoxide (CO) (paper I), atomic oxygen and hydrogen. The backward-lasing (BL) technique was developed and employed in order to detect atomic hydrogen in a CH_4/ O_2 and CH_4/air flame (papers II-IV). Novel variants of Coherent anti-Stokes Raman scattering (CARS) and laser-induced grating spectroscopy (LIGS) were developed and utilized for temperature measurements in gas (papers V-VI). The role of fs-pulse excitation in these techniques is discussed as well.

3.1 Laser-Induced Fluorescence

Laser-induced fluorescence (LIF) is a well-known and widely used versatile technique for measuring minor species concentrations and distributions. In the thesis project the technique was mainly employed in flame studies for measuring concentration profiles [7] (paper I) and 2-dimensional (2D) fluorescence imaging (see section 4.1.2). For the combustion research community it is important to obtain reliable experimental data about species concentrations and distributions in flame fronts (reaction zones) and post-flame regions (product zones) in both laminar and turbulent flames, in order to validate models and theories. Pioneering works on applications of LIF to measure flame radicals and combustion intermediate species were performed by Kohse-Höinghaus [8], Crosley and Smith [9], and Aldén et al. [10-13].

For describing the LIF process a simple two-level energy model [5] can be considered (see Fig. 3.1). Laser-induced fluorescence is usually described as a two-step process. In the first step, level E_2 gets populated after absorption of a photon of light, whose wavelength matches the energy separation between the ground state and the excited state (E_2-E_1). Such energy transfer is called resonant excitation or

resonant absorption, and is denoted b_{12} (absorption rate constant). In the second step, several processes might occur. The atoms can deexcite down to the lower level E_1 while chaotically emitting photons, a process known as spontaneous emission, or fluorescence, and denoted in the Fig. 3.1 as A_{21} (spontaneous emission rate constant). If a photon is resonantly absorbed by an atom which is already excited into level E_2, the excess energy can be transferred into emission of a photon. In this process, called stimulated emission, designated b_{21}, the emitted photon obtains exactly the same phase and the same direction as the incoming photon. De-excitation from the upper energy level E_2 can also happen without emitting any photons. One of these processes is called quenching – a radiationless collisional energy transfer and represented by a rate constant Q_{21}. With the use of a strong laser field the upper energy level E_2 can be depleted by a photo-dissociation or photoionization. These processes are described by P and W_{2i}, which are the corresponding rate constants. Photo-dissociation is only relevant for molecules, and implies that the excited molecule makes a rapid transfer to a nearby dissociative energy state, which ultimately results in formation of fragments. Such a process is also referred to as photolysis or photofragmentation.
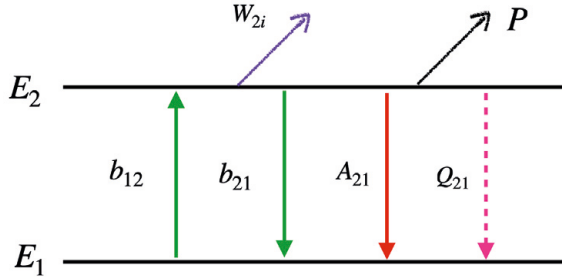

Figure 3.1. A simple two energy level fluorescence model diagram with the indicated transitions.

The two-level model gives two simple rate equations describing the temporal derivatives of the populations N_1 and N_2.

$$\frac{dN_1}{dt} = -b_{12}N_1 + (Q_{21} + A_{21} + b_{21})N_2 \tag{3.1}$$

$$\frac{dN_2}{dt} = -(b_{21} + Q_{21} + A_{21} + W_{2i} + P)N_2 + b_{12}N_1 \tag{3.2}$$

We are interested in the time dependence of the emitted fluorescence, which is proportional to the population in the upper state, i.e. $N_2(t)$. If we assume that the exciting laser pulse has a duration that is much shorter than the lifetime of the fluorescence signal, and only consider $N_2(t)$ after the laser pulse has disappeared, then b_{12} and b_{21} can be neglected. Also, assuming insignificant photodissociation and ionization, i.e. $P = W_{2i} = 0$, we can simplify Eq. 3.2:

$$\frac{dN_2}{dt} = -A_{21}N_2 - Q_{21}N_2 \qquad (3.3)$$

With the initial condition $N_2(0) = N_2^0$, where N_2^0 is the population in the upper state just after the pump pulse has disappeared, Eq. 3.3 has the solution:

$$N_2(t) = N_2(\tau_L)e^{-(A_{21}+Q_{21})t} = N_2 e^{-t/\tau}, \qquad (3.4)$$

where τ_L is the duration of the laser pulse. The fluorescence signal is thus described by a mono-exponential decay function with a 1/e-lifetime $\tau = 1/A_{21} + Q_{21}$, which is often referred to as the fluorescence lifetime. As evident from this expression, the fluorescence lifetime decreases with increasing quenching rate. Since A_{21} is a constant that often is available in the literature, fluorescence lifetime measurement is a way to measure the quenching rate.

If we make measurements in a combustion environment at atmospheric pressure, then the quenching rate is typically very high due to atomic/molecular collisions and becomes the primary mechanism responsible for the deexcitation. The fluorescence efficiency, also referred to as fluorescence (quantum) yield, depends on all deexcitation processes, but if P and W_{2i} are insignificant it becomes [5]:

$$\Phi = \frac{A_{21}}{A_{21}+Q_{21}}, \qquad (3.5)$$

and if $Q_{21} \gg A_{21}$ it simplifies further to $\Phi = A_{21}/Q_{21}$. In order to measure species concentrations quantitively, knowledge about the fluorescence efficiency, hence the quenching rate, is required. This essentially requires knowledge about the deactivation rates of all species colliding with the excited atom/molecule during the fluorescence measurements, which is quite difficult, since the chemical composition often is unknown. Prior to my PhD work quantitative fluorescence and quenching studies have been performed in our research group with the use of picosecond (ps) laser excitation [14]. With the fs-pulses used in the present work, it is possible to take a further step in this development. Sometimes, quenching can completely be avoided if we deliberately make photoionization (W_{2i}) or predissociation (P) the dominant deexcitation channel. This, however, requires very high intensity or that the pumped state is predissociative. In this case Eq. 3.5 changes and the fluorescence efficiency is given by: $\Phi = \frac{A_{21}}{A_{21}+Q\ (P\ or\ W_{2i})}$.

Another approach to mitigate the problem with quenching is saturation regime, where the fluorescence is insensitive to a further increase in laser intensity and the stimulated emission rate (b_{21}) becomes larger than the quenching rate Q_{21}. Working in this regime maximizes the fluorescence signal and minimizes the dependence on the quenching term and laser intensity fluctuations. The problem is that it is difficult to obtain complete saturation for all the frequencies under the absorption profile (spatial, spectral and temporal "wings" of the laser pulse). This restricts the overall detectability of the fluorescence signal.

3.1.1 Two-photon excitation

Several atoms of interest in combustion and atmospheric research possess their absorption lines below 200 nm. Even if today's tuneable lasers can produce light below 200 nm, it would be very hard to perform an experiment with such lasers under atmospheric conditions, since the atmosphere absorbs wavelengths below 200 nm, which is why this regime is referred to as vacuum ultra violet (VUV). A solution to this problem is to use simultaneous absorption of two or more photons in order to excite these high-lying energy states. If two photons are used for the absorption the method is hence called two-photon LIF (TPLIF). This technique was first demonstrated by Bradshaw and Davis [15] for detecting NO under atmospheric conditions. Two-photon laser-induced fluorescence as well facilitates quantitative measurements of atoms and molecules such as O [16-18], H [19-24], CO [7, 25, 26], OH [27, 28], Kr [29]. Optically, hydrogen has been detected via two-step saturated fluorescence using Lyman-α radiation at 234 nm and Balmer-α fluorescence detection at 656 nm [19], two-photon excited fluorescence with 205-nm excitation wavelength [24] and other multi-photon excitation schemes [30]. The two-photon excitation process for hydrogen atoms is demonstrated in Fig. 3.2a, where two photons of 205 nm wavelength are used to transfer the energy from $1s^2S$ to $3s^2S$. The fluorescence is then emitted at 656 nm from the $3s^2S \rightarrow 2s^2P$ decay.
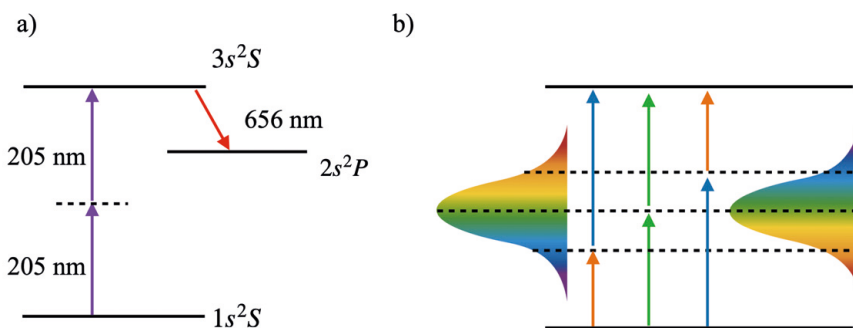

Figure 3.2. a) Two-photon excitation scheme for H atom detection. b) Schematic illustration of multiple photon-pair excitation with a broad-bandwidth fs-laser.

Femtosecond pulses are spectrally broad and one might think that excitation with a broad bandwidth would be very inefficient due to the very narrow absorption lines of atoms. However, the entire bandwidth of fs-pulses provides a combination of different photon pairs, with different frequencies but the same phase, and their collective work gives a big contribution to the multi-photon excitation process. See the schematic illustration in Fig. 3.2b.

3.1.2 Photolytic interferences

In a photodissociation process (see the illustration in Fig. 3.3) a parent molecule, AB, is excited to an upper unbound state, usually by a UV photon, creating an excited complex (AB)*, which rapidly breaks apart into two fragments, A and B. Now, consider a study in which it is of interest to detect A atoms in a gas of unknown composition, and a UV laser is tuned to a resonance in that atom in order to induce fluorescence, then if the molecule AB is present in the gas, additional A atoms might be produced through photodissociation. This situation leads to fluorescence from the naturally present A atoms and from the additional A atoms produced by photodissociation of AB, which result in a measurement error, i.e. the A atom concentration is overpredicted. This type of undesired effect is called photolytic interference.
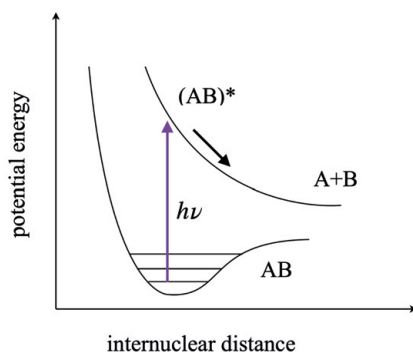

Figure 3.3. Illustration of photodissociation of AB molecule by a UV photon.

For H atom detection in combustion environments, photolytic interferences may originate from vibrationally excited H_2O in the product zone and vibrationally excited OH. Under rich flame conditions significant precursors for photolytic interference are CH_3 and C_2H_2 [21].

Femtosecond laser provides high peak power despite the relatively low pulse energy, which is a combination that provides efficient multi-photon excitation (high peak power) with minimum photolytic interferences (low pulse energy). It has been reported that there is no evidence of photolytically produced H atoms for TPLIF detection in $CH_4/O_2/N_2$ Bunsen flames using a 205-nm fs laser beam collimated to 1 mm in diameter with a maximum pulse energy of 8 μJ [22]. In hydrocarbon flames the use of ps laser has been demonstrated to reduce interferences from CO_2 photolysis in TPLIF measurements of O atoms [17]. For H atom detection in CH_4 and H_2 flames, ps-excitation has also shown to reduce photolytic interferences [20]. However, the use of fs-laser pulses, rather than nanosecond (ns)- or ps-laser pulses, as demonstrated by Kulatilaka et al.[16, 23] brings more advantages for quantitative

diagnostics of combustible gases. If with high-energy ns-laser pulses the detected fluorescence signal is susceptible to laser-induced photolytic interferences, then the use of ps-laser excitation mitigates this problem. Nevertheless, the spectral bandwidth of the ps-laser pulse is sufficient enough to drive multi-photon excitation, the peak power of the laser is lower compare to the fs laser. Transform-limited fs-laser pulses have hight peak power as well as the broad spectral bandwidth, which results in an efficient excitation due to the pairing of multiple in-phase photons [16] as it is demonstrated in Fig. 3.2b.

Investigation of the normalized spatial profile of the fluorescence signal for different pulse energies is a common approach for studying potential photolytic interferences [21]. As long as the spatial profile of the fluorescence signal remains the same with increasing laser pulse energy, no photolytic interference is present, as illustrated in Fig. 4.1b. If at a certain laser pulse energy, the profile changes, then that is an indication of photolytic interference. This is the approach used in the present thesis project for fs-TPLIF measurements of H and O atoms.

3.1.3   Measurement configuration

One of the advantages of the LIF technique is that it has a relatively simple measurement configuration. As an example, 2D-LIF is done by creating a laser sheet with a cylindrical lens and the induced fluorescence, for example in a flame, is collected and imaged onto an intensified CCD camera (iCCD) oriented orthogonally in relation to the propagation direction of the laser beam, as shown in Fig. 3.4. In order to collect and image the isotropically radiating fluorescence, the camera has to be equipped with a collection lens. Usually, a narrow band filter is mounted next to the camera lens in order to supress background emission and only collect the emission at the wavelength of interest. Another means for suppression of background luminescence, such as chemiluminescence and Planck radiation, is gated detection. This approach is very efficient in experiments with pulsed lasers, where a short-lived signal, such as fluorescence, is promptly induced by the laser pulse. Using a detector, such as an iCCD camera, that can be gated, i.e. be "open" only while the signal of interest is emitted, the continuous background luminescence can be massively suppressed.
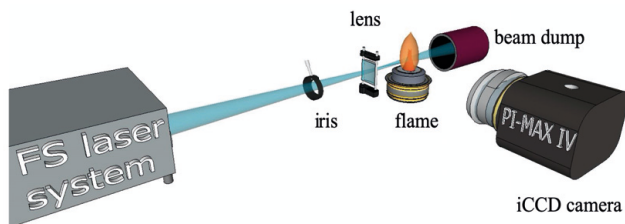

Figure 3.4. Sketch of a basic LIF setup.

14

3.2 Lasing

Mirrorless lasing is an umbrella term for describing laser-like radiation in the presence of single-pass optical gain. It shares common features with laser light such as coherence, low divergence, and high directionality. Lasing in the forward direction is usually achieved in an elongated gain volume along the propagation of a pump laser beam. At the same time, lasing may also be achieved in the backward direction with a backward-lasing beam retracing the pump laser beam path. Backward lasing (BL) has generated a special interest in the research community, not least within environmental monitoring, since it could potentially revolutionize the remote-sensing field, providing a sensitive method for stand-off detection of hazardous pollutants, gaseous leakages, and greenhouse gases.

Backward lasing has the potential to significantly increase the detection sensitivity compared to conventional light detection and ranging (LIDAR), where the generated signal is of incoherent nature and only a small fraction of it can be collected and detected, as schematically illustrated in Fig. 3.5. In addition, the LIDAR signal decreases with distance (R) as $^1/_{R^2}$. These limitations do not exist for the BL technique.
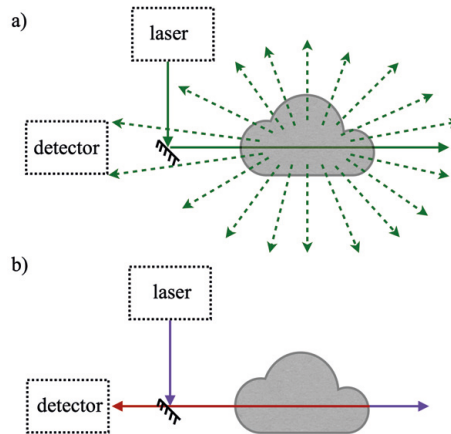
Figure 3.5. Schematic illustration of the difference between a) traditional LIDAR and b) the backward lasing technique.

3.2.1 Lasing approaches

Lasing occurs from the population inversion between two energy levels of a gas in a focal volume created by the pump laser beam. Two main approaches have been utilized for accomplishing backward lasing: (1) optical filamentation [31-36] and (2) multi-photon excitation of the molecules/atom present in a gas [37-40].

Optical filaments, described by a weakly ionized plasma channel, can be generated by extremely intense ultrashort laser pulses, where the laser intensity can reach 10^{13}- 10^{14} W/cm^2. The principle of laser filamentation lies in a dynamic interplay between self-focusing and plasma defocusing. The self-focusing is described by a change of a refractive index due to the presence of a strong electric field, which can happen when the peak power exceeds a critical value. This phenomenon is also known as optical Kerr effect. At very high laser intensities, the refractive index of the medium changes nonlinearly, $n(I) = n_0 + n_2 I$, where n_0 is the linear refractive index, n_2 is the non-linear refractive index, and I is the intensity of the laser pulse. The optical Kerr effect induces refractive index variation and, for a Gaussian pulse, makes it higher in the central part than at the edges of the laser beam profile. As a result, the medium starts acting like a positive lens. The intensity of such a self-focused beam becomes so high that it ionizes the medium, i.e. generates a plasma. The plasma has a negative effect on the refractive index $n = -\frac{p_e}{p_{cr}}$, where p_e is the electron density and p_{cr} is the critical plasma density (for 800 nm fs-laser pulse $p_{cr} \sim 1.7\ 10^{21}$cm^{-3} [41]). As a result, the plasma acts as a negative, i.e. divergent, lens. The combined action of self-focusing and defocusing, generating a thin (~100 μm) self-sustained channel, is called a laser filament. This effect is schematically illustrated in Fig. 3.6a.
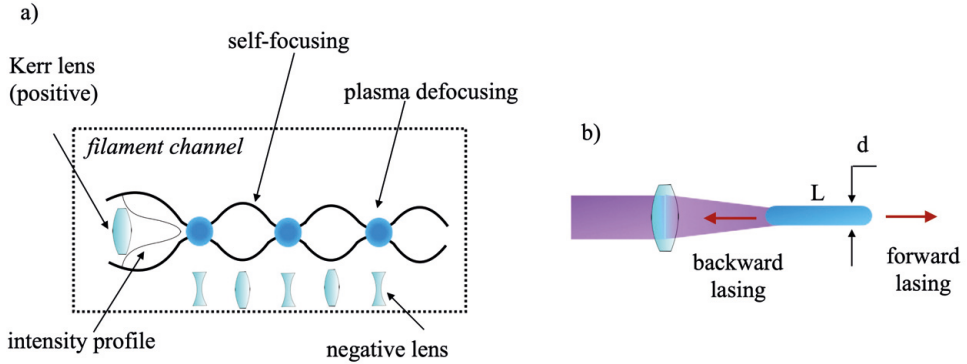

Figure 3.6. a) Illustration of a laser filament as a combined effect of self-focusing and plasma defocusing. b) Gain region along the propagation direction of a pump laser beam.

An attractive property of optical filaments is generation of broadband emission, so called supercontinuum or white light, sometimes ranging from UV to IR wavelengths [41]. The strong spectral broadening is a result of another non-linear optical effect called self-phase modulation, which is a consequence of the temporal variation of the refractive index, i.e. $n(t) = n_0 + n_2 I(t)$. As a result, new frequencies are produced and the pulse exhibits a rainbow-like emission, typically with a high intensity white colour in the centre and bluish colour (high frequencies)

in the outer circle [42]. Absorption spectroscopy based on white light from an optical filament has been utilized for atmospheric studies [33, 34] and backward lasing action through optical filamentation in N_2 has been reported in [35, 36, 40].

The second approach to generate BL is based on resonant multiphoton excitation. In flames, where atomic radicals like O [10], H [43], C [44] are naturally present two-photon excitation has been found to generate stimulated emission [45], i.e. "lasing" generated in both the forward and backward direction. Two-photon induced stimulated emission in atomic oxygen was first observed by Aldén et al. [10]. In their work they utilized nanosecond pulsed laser tuned to 226 nm to excite naturally present atomic oxygen in a flame via two-photon excitation from $2p^3P$ to $3p^3P$. As a result of the population inversion created between the pumped $3p^3P$ and $3s^3S$ state, stimulated emission at 845 nm was observed between these states.

The high intensity of femtosecond laser pulses available nowadays allows efficient multi-photon excitation without the need for high pulse energies, as demonstrated by Dogariu et al. [37]. The backward-lasing studies reported in this thesis (papers II-IV) are primarily focused on investigating the potential for single-ended stand-off detection of H atom in flames and, are based on the same femtosecond two-photon excitation scheme as the fluorescence studies (see Fig. 3.2). Population inversion was established between $3s^2S$ and $2s^2P$, and stimulated emission was generated at 656 nm and detected in both the forward and backward direction.

The lasing direction is determined by the geometry of the gain region. High gain is established in the focal volume of the pump laser along the propagation direction of the beam. It resembles a pencil-shaped excitation volume as a free-space single-pass cavity, as shown in Fig. 3.6b. High L/d ratio allows exponential amplification of the stimulated emission in both the forward and backward directions, where L is the longitudinal length and d is the transverse diameter of the excitation volume. The amplification is related to the gain coefficient g and L as: $amplification = e^{gL}$.

3.2.2 Generation mechanisms

Laser-like (or stimulated) emission has been observed and reported on in the three publications on mirrorless lasing in the thesis project (papers II-IV) [46-48]. However, the physical mechanisms behind these observations still remains unsettled and highly debated in the research community. Three main mechanisms are proposed: (1) superradiance (SR), (2) superfluorescence (SF) and (3) amplified spontaneous emission (ASE). Main features of these processes will be presented below.

We are already familiar with spontaneous emission, i.e. fluorescence, where atoms/molecules in the probe volume interact independently from each other. The emission obeys an exponential decay with a decay time τ_{sp} (see Fig. 3.7a),

the radiation pattern is in this case isotropic. If the number of atoms/molecules in the probe volume is significantly increased, the atoms/molecule are not interacting independently anymore, and may start emitting collectively together at a much higher rate and intensity compared to the spontaneous emission. Such an emission process in called superradiance or superfluorescence [49]. This collective emission process has a radiation duration of $\sim \tau_{sp}/N$ (see Fig. 3.7b), where N is the number of radiators (i.e. excited atoms/molecules) in the probe volume. The peak intensity of the emission is proportional to N^2.
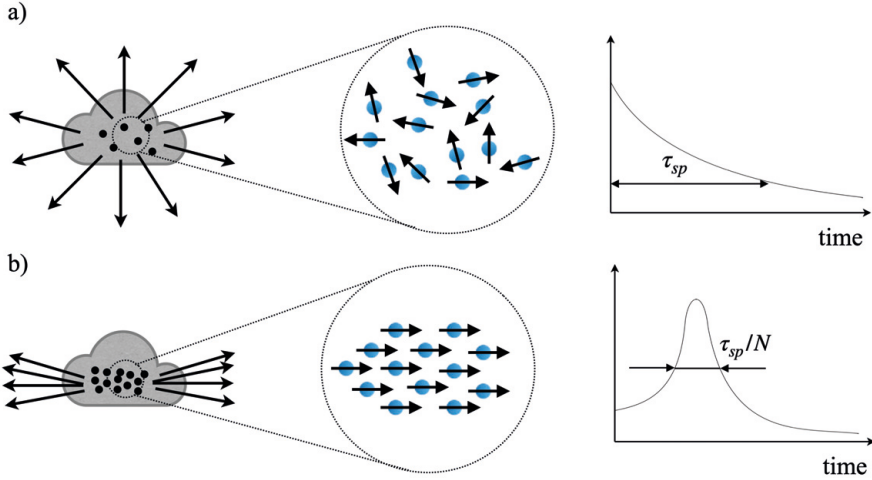

Figure 3.7. Illustration showing a) an ordinary isotropic sponteneous emission process with a dephasing time τ_{sp} and b) a superradiant anisotropic process, where all the atoms radiate together with a similar phase. The process decays with τ_{sp}/N.

The phenomenon of SR in a cavity-free system was first predicted by Dicke in 1954 [50]. The superradiant emission is a cooperative process between the atomic dipoles in an initially inverted quantum system (correlated), meaning that the phases of dipoles belonging to different atoms build up a giant macroscopic dipole and exhibit atomic coherence, which results in coherent emission. The emission rate increases with increasing number of coupled dipoles.

Superfluorescence shares similar behaviour with SR. The difference is that SF is a cooperative emission from an uncorrelated system [51], where there is initially no coherence and no macroscopic dipole present. In this case the system is started by ordinary fluorescence emission, whereupon a macroscopic dipole is created within a delay time τ_D. This process eventually results in strong coherent emission. The three-level energy system, illustrated in Fig. 3.8, shows the difference between SR and SF.
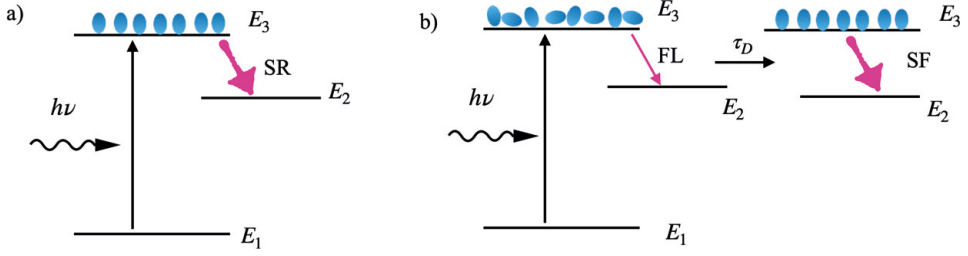
Figure 3.8. Illustration of a) superradiance (SR) and b) superfluorecence process (SF), which starts as ordinary fluorecnece and develops the coherence in a time period τ_D.

Both SR and SF show a strong dependence on the concentration in the probe volume and on the dephasing collisions [52]. Further nonlinear effects that might arise in SR and SF are frequency chirping [49] and beating [53].

The third mechanism, ASE, exhibits spontaneous emission from a purely incoherent system, where all excited atoms act individually with random phase relationships between their dipole moments. Here, the system does not build up a macroscopic dipole. When population inversion is established, the spontaneous emission is amplified by stimulated emission within a single-pass gain through the probe volume. The resulting emission will undertake a direction defined by the geometry of the gain medium, i.e. forward or backward. Amplified spontaneous emission grows in a non-linear manner as the pump beam travels through the probe volume and its intensity is linearly dependent on the concentration of excited atoms/molecules, as opposed to SF and SR, which depend quadratically on the concentration. It should be noted that the emission observed for a given experimental configuration can be a mixture of ASE and SR or SF.

The identification of the physical mechanisms responsible for mirrorless lasing in the forward and backward direction is clearly not trivial. Features of SR, SF and ASE might be quite similar to each other, for example, they all show the presence of a laser threshold, low beam divergence and directionality. The exact distinction between these processes requires measurements of the collisional dephasing time, collective damping time, single pass gain, total number of excited atoms, etc. [54].

3.2.3 Spatially-resolved detection with backward lasing technique

In analogy with LIDAR, it is possible to use the backward lasing technique for obtaining remote range-resolved information about the medium by temporally resolving the backward lasing signal. However, in a contrast to LIDAR, which is fundamentally limited by the non-directional, essentially isotropic, emission from the region of interest, the highly directional backward lasing signal drastically improves the signal collection efficiency and thereby the detection sensitivity.

With excitation based on fs-laser pulses, as utilized in the current thesis work, it is possible to use the concept of backward-lasing for excellent single-shot spatially resolved stand-off detection of atomic species flames (papers II and IV).

Figure 3.9 describes how range resolved information can be achieved with the BL technique. In an experiment with two narrow welding flames, the locations of H atoms in the two flames are revealed by temporally resolving the backward lasing signal, as illustrated in Fig. 3.9a. The temporal profiles were recorded with a streak camera (see Fig. 3.9b), located ~2 m away from the measurement volume.
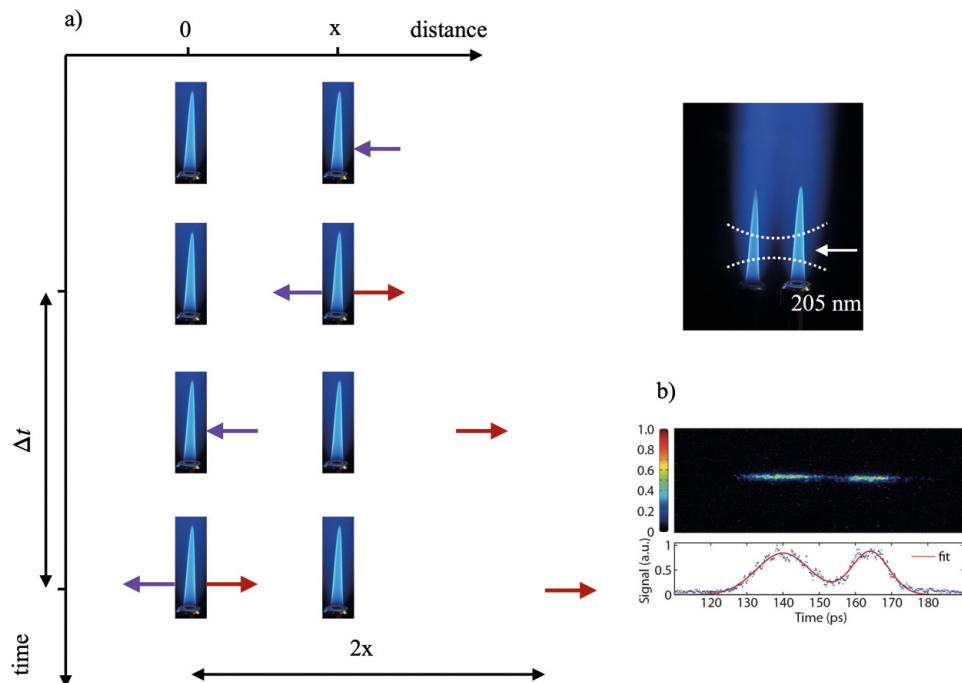

Figure 3.9. a) Illustration of the backward lasing concept for obtaining spatially resolved information about the presence of hydrogen atoms in two flames. A femtosecond pump laser pulse of 205 nm wavelength interacts with the first flame and generates a 656 nm signal pulse travelling backwards, by the time the pump pulse reaches the second flame the backward lasing pulse generated from the first flame will already travel the distance equal to the separation between the flames. By the time the backward lasing pulse will be generated from the second flame the distance will hence be doubled. b) Single-shot data showing the temporal profile of the 656 nm backward lasing signal originating from the two flames recorded with a streak camera [46] (paper IV).

As evident from Fig. 3.9, range resolution is easily achieved from the time-resolved signal, through the relation $x = \frac{c \cdot t}{2}$, where x is the distance to the location of the species of interest, c is the speed of light, and t is the arrival time of the signal on the detector. This is exactly the same expression as for conventional LIDAR.

The minimum distance resolved with the current technique is 1.6 mm [46] (paper IV), as demonstrated in the results shown in Fig. 3.10, where the distance between the two reaction zones, containing H atoms, is resolved.
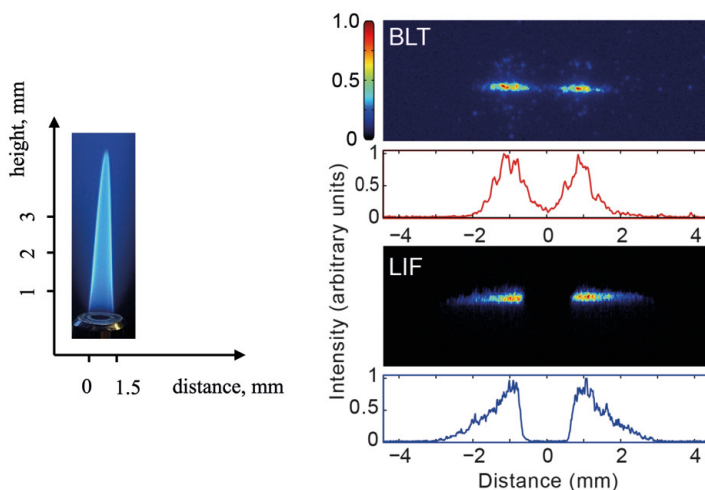

Figure 3.10. Single-shot measurement of the spatial profile of atomic hydrogen captured with the backward lasing technique (BLT) and LIF, respectively, in a welding torch flame of 1.5 mm diameter at 3 mm height above the burner [46] (paper IV).

A comparison between the spatial profiles of the hydrogen signals obtained by BLT and LIF (Fig. 3.10) shows qualitative similarities, such as that two peaks are observed, showing that it is possible to distinguish the two reaction zones. However, the shapes of the hydrogen distributions obtained with the two techniques are different. Understanding this difference requires knowledge about the physical mechanisms involved in the signal generation process. This is also a requirement to be able to quantify the hydrogen concentration.

One important step towards understanding the lasing generation mechanism is to study the gain dynamics , which was done in the current thesis work, and reported in paper III [48]. Although more work is still needed for quantification of concentrations, the technique holds great potential for single-ended diagnostics, which in some applications, where the optical access is severely limited, might be the only measurement option. In such applications BL could be of great value, despite currently being restricted to qualitative measurements.

3.3 Coherent anti-Stokes Raman scattering

When an atom or molecule is irradiated by an external light field several processes might occur. If the energy of the incoming photon matches the energy separation between two energy levels of the atom/molecule, the photon might be absorbed causing a resonant transition from the lower to the higher energy level. The energy gained by this process may be released as spontaneous emission or fluorescence as described in section 3.1. If the energy of the incoming photon does not correspond to the energy separation between two energy levels, then another form of light-matter interaction may occur, namely scattering, which, opposed to absorption, is not a resonant phenomenon. There are two major types of scattering: elastic scattering, i.e. the photon energy (or wavelength) of the incident and scattered light is exactly the same, and inelastic scattering, for which the photon energy of the scattered light has either increased or decreased compared to the incident light. Rayleigh and Mie scattering are different types of elastic scattering, while Raman scattering is an inelastic process. The phenomenon of Raman scattering is named after Sir Chandrasekhara Venkata Raman, who first observed it in 1928 [55]. Coherent anti-Stokes Raman scattering (CARS) is a technique based on the Raman effect, but it differs significantly from spontaneous Raman scattering in terms of light-matter interaction, which is nonlinear, and signal characteristics, which is coherent, as opposed to spontaneous Raman scattering which is a linear and incoherent technique.

3.3.1 Brief introduction to rotational Raman scattering

If a molecule is affected by an external electrical field E, a dipole moment can be induced, i.e. the molecule becomes polarized. The induced dipole moment is given by:

$$\mu = \alpha E, \tag{3.6}$$

where α is the polarizability of the molecule, which is a molecule-specific property that describes the tendency of the electron cloud to get deformed by an external electrical field. The polarizability may change as the molecule rotates. If a linear molecule is rotating at a circular frequency ω_{rot} its polarizability will be time-dependent (if it is anisotropic):

$$\alpha = \alpha_0 + \frac{1}{2}\Delta\alpha \cos(2\omega_{rot}t), \tag{3.7}$$

where α_0 is the mean polarizability and $\Delta\alpha = \alpha_\parallel - \alpha_\perp$, i.e. α ranges from $\alpha_0 + \Delta\alpha$ to $\alpha_0 - \Delta\alpha$ as the molecule rotates. The factor 2 in Eq. 3.7 appears because the polarizability for a linear molecule returns to its initial value twice each revolution. The electric field provided by a laser has an oscillatory nature, i.e.

$E(t) = E_0 \cos(\omega t)$. Inserting this E-field and Eq. 3.7 into Eq. 3.6 results in an expression revealing that the induced dipole moment has three components, where one term, oscillating at the same frequency as the applied electrical field, corresponds to elastic Rayleigh scattering. The other two terms, which are upshifted and downshifted in frequency, respectively, corresponds to inelastic Raman scattering. These two components are called Stokes (downshifted) and anti-Stokes (upshifted) lines respectively. The strength of the Raman lines is typically $\sim 1/1000$ of the strength of the Rayleigh line [56].

For a system consisting of N molecules per unit volume, the microscopic polarizability, α, is replaced with the macroscopic quantity susceptibility, χ. The induced polarization, which is thus equal to dipole moment per unit volume, is then described as

$$P = N\mu = \varepsilon_0 \chi E, \tag{3.8}$$

where ε_0 is a vacuum permittivity. For high intensities, such as those provided by short-pulse lasers, the induced polarization will be slightly distorted and depend nonlinearly on the applied electric field. Of particular interest for CARS is the third-order nonlinear polarization, which can be expressed $P^{(3)} \sim \chi^{(3)} E^3$, where $\chi^{(3)}$ is the third-order (nonlinear) susceptibility.

Rotational coherent anti-Stokes Raman spectroscopy (RCARS) utilized in the thesis work, is a coherent non-linear four-wave mixing technique, based on the non-linear response of molecules through the third-order susceptibility. For a fundamental description of the nonlinear process it is recommended to follow the references [57, 58]. The RCARS technique is widely used for temperature and major species concentration measurements in gas mixtures. In RCARS, Raman transitions between rotational states within the same vibrational state are probed, and the selection rule for allowed transitions is $\Delta J = 2$ for diatomic molecules. Rotational CARS was demonstrated for the first time in 1976 [59] and since then it is considered to be one of the most accurate techniques for temperature measurements in combustion environments.

3.3.2 Basic principle of rotational CARS

Three laser beams are involved in the generation of a RCARS signal. First two beams, denoted as pump (ω_p) and Stokes (ω_S) coherently excite rotational Raman resonances of the molecules, then a third beam (ω_{pr}) interacts with the excited states and creates a fourth beam called the anti-Stokes or CARS signal (ω_{CARS}). This beam is generated from the crossing region of the three incident beams, as illustrated in Fig. 3.11a, and it occurs as a result of the laser interacting with the medium through the third-order susceptibility $\chi^{(3)}$. The RCARS signal thus carries information about the Raman resonances (also called Raman coherences) present in the crossing

region. As illustrated in Fig. 3.11a the phase-matching condition $\vec{k}_{CARS} = \vec{k}_p + \vec{k}_{pr} - \vec{k}_S$ has to be fulfilled in order to generate a strong CARS signal. The phase-matching geometry outlined in Fig. 3.11a is a so-called planar BOXCARS configuration. In this configuration, due to the conservation of momentum, the CARS signal is generated in a direction that is close to the pump beam $\vec{k}_p$. In this thesis work, the pump and Stokes beams were generated by a broadband fs-laser beam. This variant of RCARS is therefore called dual-broadband rotational CARS, an approach that is very well established based on nanosecond pulsed lasers [60, 61]. This dual-broadband approach implies that many photon pairs are used to drive each Raman resonance. The probe beam ω_{pr} is provided by a nanosecond single-mode laser, which leads to high spectral resolution in probing the Raman resonances.
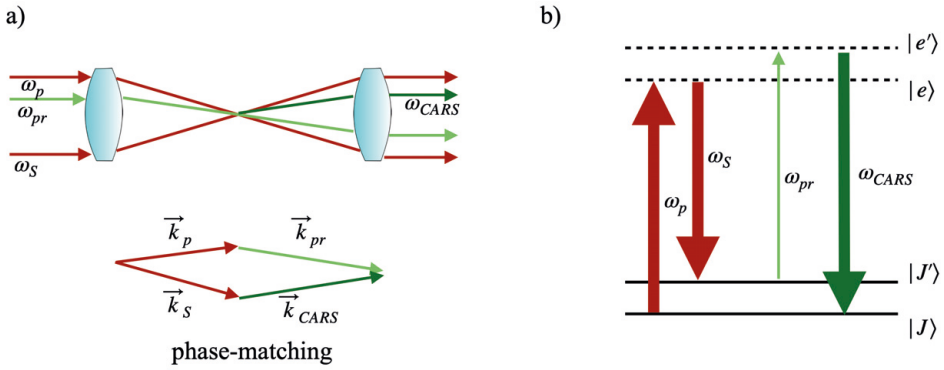

Figure 3.11. a) Basic phase-matching scheme for a planar BOXCARS configuration used in the thesis work, whrere ω_S and ω_p are the frequencies of a broadband fs-laser source and ω_{pr} is a narrowband frequency of a ns-laser sourse; b) correponding energy level diagram, where $|e\rangle$ and $|e'\rangle$ are virtual states; the diffrence between the rotational levels $|J\rangle$ and $|J'\rangle$ is called Raman frequency shift ($\omega_p - \omega_S$).

3.3.3 Rotational Raman linewidths

The linewidths of the rotational Raman lines are important since they affect the resonant part of the third-order susceptibility, and therefore also the shape of the RCARS spectrum. The rotational Raman linewidths are related to the rotational relaxation rate, which has a certain value for each rotational Raman line, depending on the temperature, pressure, and gas composition. The rotational Raman linewidth is inversely proportional to the lifetime of the excited Raman coherence τ_J [62]:

$$\Gamma_J = (2\pi c \tau_J)^{-1}, \tag{3.9}$$

where c is the speed of light and J is the rotational quantum number of the lower rotational state of the Raman transition. Equation 3.9 reveals that it is possible to determine the rotational Raman linewidths by measuring the lifetimes of the rotational Raman coherences. This means that a method that can record the RCARS signal with both high spectral resolution and high temporal resolution, would allow temperature measurements based on experimentally obtained Raman linewidths. The hybrid fs/ns rotational CARS method discussed in the next section has exactly this capacity. The procedure of receiving the temperature information based on experimentally obtained Raman linewidths is discussed more in detail in related work (paper X) [63].

3.3.4 Hybrid fs/ns CARS

The lifetimes of rotational Raman coherences are very short, on the order of 100 ps. In order to study these, measurement techniques with high temporal resolution are thus required. Using ultrafast lasers, i.e. picosecond or femtosecond lasers it is possible to separate in time the coherent excitation of the rotational Raman coherences and the dephasing due to molecular collisions [62, 64-66] and the prompt nonresonant part of the signal can be suppressed.

In non-stationary environments, such as in turbulent flames, the gas composition is typically unknown and may vary significantly both spatially and temporally, which requires that the Raman linewidths are measured in-situ on a single-shot basis for accurate temperature evaluation. Several combinations of pump/Stokes and probe pulses have been proposed, as depicted in Fig. 3.12. In the first one, illustrated in Fig. 3.12a, the coherent excitations are prepared by fs-laser pulses and probed by a ps-laser pulse [66]. The broadband pump/Stokes pulses excite all rotational Raman coherences, which are then probed, after a certain delay, by the ps probe pulse, forming an RCARS signal containing all rotational Raman resonances. However, in order to determine the lifetimes of the rotational Raman coherences, and thus the corresponding linewidths, sequential measurements have to be done for a large number of delays between the fs-excitation pulses and the ps-probe pulse. Obviously, this approach cannot be rated as a single-shot technique, which prevents studies in turbulent environments, and it is also time consuming. Figure 3.12b however, shows an approach that allows time-resolved detection of the Raman coherences on a single-shot basis, provided that the RCARS signal is detected with a streak camera. Picosecond laser pulses are used to excite the Raman coherence and a long ($\sim$ 5 ns) single-mode nanosecond laser pulse is used to probe the coherence [67]. This approach is promising as the ns-laser pulse captures the whole decay of the Raman coherence in a single shot, however, the relatively narrow linewidth of the ps-pulses only allows excitation of one or two rotational resonances, i.e. the full RCARS spectrum cannot be generated in a single-shot recording. Of course, the full RCARS spectrum can be obtained by tuning the wavelength of

the Stokes laser pulse, but this is time consuming and, again, prevents measurements under turbulent conditions.
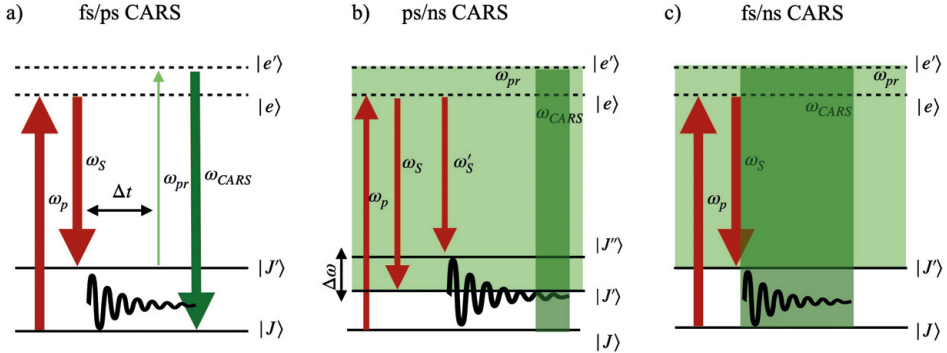

Figure 3.12. a) fs/ps CARS, where Δt is a delay between pump/Stokes and probe beam, b) ps/ns CARS, where $\Delta \omega$ is a wavelength tuning range for Stokes beams, c) fs/ns CARS.

The method illustrated in Fig. 3.12c provides the possibility to study the full temporal and spectral evolution of the rotational Raman coherences on a single-shot basis [63, 68]. A solution to the limited bandwidth of ps-laser excitation pules is, of course, to use broadband fs-laser pulses for coherent excitation of the whole manifold of Raman coherences. Just like in the ps/ns approach, a single-mode nanosecond laser pulse is used to probe the coherences, and the spectrally dispersed RCARS signal is detected by a streak camera, providing high temporal resolution. The technique is called hybrid fs/ns CARS. The pump and Stokes femtosecond laser pulses used in the thesis work are near Fourier-transform limited and have a pulse duration of 125 fs, corresponding to a linewidth of 150 cm^{-1} (FWHM). A convolution of both pulses gives an effective spectral coverage of 210 cm^{-1} (FWHM).

The ability of the hybrid fs/ns CARS technique to measure Raman linewidths on a single-shot basis is of great value for accurate gas-phase thermometry, as the technique does not require any pre-knowledge about collider molecules and their number densities in the probe volume.

In most of the experiments performed within the thesis work the laser pulse energy for pump and Stokes fs-pulses was kept rather low, ~ 40 μJ for both pulses. Increasing the pulse energy above ~ 100 μJ leads to significant broadening of the spectral lines as well as additional spectral lines appearing at low Raman shifts, which are consequences of the Stark effect present at the high electric fields imposed by the excitation pulses [68, 69]. This phenomenon is briefly introduced in section 4.3.3.

3.4 Laser-induced grating spectroscopy

Laser-induced grating spectroscopy (LIGS) is a non-linear optical technique used for gas-phase diagnostics. Similar to CARS and Lasing, the LIGS signal appears as a highly directional beam of low divergence. Laser-induced grating spectroscopy is mainly applied for measuring temperature [70-73], speed of sound [74, 75], thermal diffusivity [76] and, occasionally, species concentrations [77]. A laser-induced grating arises from a nonlinear interaction between two laser beams (see two red-coloured beams in Fig. 3.13) and the medium, forming an interference pattern with a spacing Λ between the fringes.
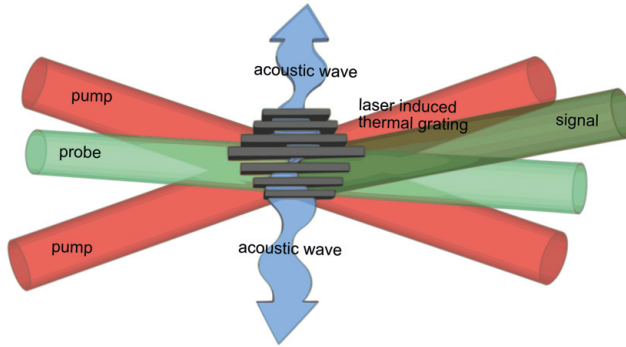

Figure 3.13. Schematic illustration of the alignment principle in LIGS.

The interference fringes period is described as $\Lambda = \frac{\lambda_{pump}}{2\sin\left(\frac{\theta}{2}\right)}$, where λ_{pump} is the wavelength of the pump laser beam and θ is the crossing angle between the two pump beams.

A periodic modulation of the complex refractive index of the medium can be formed by resonant and non-resonant mechanisms. A *thermal* grating is formed by resonant light absorption, resulting in collisional relaxation and heat release, which occur along the high intensity fringes. A grating can also be formed by electrostriction, and this is generated at any given frequency of the laser light, i.e. a non-resonant interaction, and such a grating is hence called *electrostrictive*. The modulation is in this case built up through compression of the molecules by an intense electric field.

The modulation formed by either thermalization or electrostriction results in alteration of the material characteristics and properties such as refractive index and density. As a result, two rapid counter-propagating acoustic waves are formed (see Fig. 3.13). For a thermal grating, the rapid energy exchange between the medium and the excited molecules in it drives the formation of the acoustic waves. For an electrostrictive grating, on the other hand, the rapid motion of the dipole

moments of the molecules in the polarized medium drives the formation of the acoustic waves [78].

The wavelength of the acoustic waves is characterized by the interference fringe spacing Λ. The two acoustic waves form a standing wave and thereby a density modulation of the medium. The oscillation frequency of the acoustic wave is characterized as $f_{osc} = 1/T_{osc}$, where T_{osc} is the oscillation period. It can be shown that the oscillation period of the electrostrictive grating equals half the oscillation period of the thermal grating [78]. Further, the oscillation period is directly related to the fringe spacing and sound velocity v_s through $T_{osc} = \Lambda/v_s$.

The formation and dynamics of a laser-induced grating are probed by a third beam (see the light green-coloured beam in Fig. 3.13), intersecting the grating at the first-order Bragg angle, given by $\sin(\theta_B) = \lambda_{probe}/2\Lambda$. All the three beams are usually aligned in a folded BOXCARS configuration in order to achieve optimum phase matching.

3.4.1 Multi-photon excitation in fs-LIGS

Traditionally, ns-lasers have been employed in order to form a laser induced thermal grating by a direct single-photon resonant absorption. In such a case, the laser wavelength has to be tuned to match a resonant transition of a specific atom/molecule present in the medium. Using fs-laser pulses, the demand for a specific laser wavelength to form a thermal grating is significantly relaxed, since the wide bandwidth and high intensity typically provide numerous possible paths into an excited state through multi-photon excitation. For example, the 800-nm fs-pulses of a Ti:Sapphire laser, can create thermal gratings in N_2, O_2, and Ar, of which the former two are major species in combustion environments.

With our fs-laser system, generating light at 800-nm wavelength, we can achieve high enough laser intensity, despite the relatively low pulse energy, to drive multi-photon absorption without causing any disturbances like photodissociation [22] or photoionization.
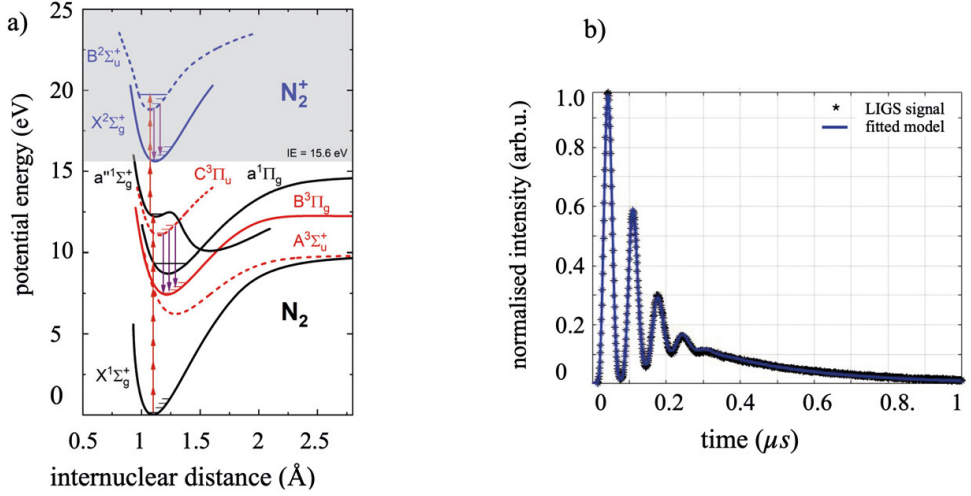
Figure 3.14. a) Energy level diagram of N_2 [70], b) LIGS signal recorded in N_2 gas flow at room temperature and a corresponding fitted model based on Eq. 3.10.

Figure 3.14 shows that it is possible to reach the $a''^1\Sigma_g^+$ state in N_2 by an 8-photon absorption process (red arrows), resulting in fluorescence in the second positive band ($C^3\Pi_u \rightarrow B^3\Pi_g$).

The method is non-intrusive, it does not result in any heat deposition to the interaction volume like it was observed in [79] , where with the hight laser intensity the temperature of the gas was raised. Additionally, ionization of N_2 is avoided by keeping the laser intensity below 1 mJ (see a broader discussion in paper VI). If the laser intensity is increased above this limit, multi-photon excitation beyond the ionization threshold (IE) at 15.6 eV occurs, which leads to the formation of a plasma grating [70].

3.4.2 LIGS signal model

In order for the fs-LIGS technique to be applicable for diagnostics, a model that can simulate signals is needed. The approach used here has been adopted from work done by Hemmerling et al. [80]. In their work they have investigated the O_2 molecule in the $b^1\Sigma_g^+$ excited state in order to distinguish and describe the conditions for the grating formation. They propose a three-stage collisional relaxation model to describe temporal profiles of LIGS signals, including contributions from electronic, vibrational, and rotational energy transfer.

Furthermore, the redistribution of the rotational energy in the ground and excited states is assumed to be "instantaneous", i.e., it occurs on a time scale much shorter than the laser pulse duration (in cases with ns-laser excitation). The vibrational and

electronic relaxation are both driven by molecular quenching, and their time scale is characterized by a time constant τ_f, which is longer than the duration of the laser pulse. This relaxation is hence much slower than the "instantaneous" process and assumed to be "finite".

An experimental LIGS signal together with a fit to a model is shown in Fig. 3.14b. The model assumes a stationary density modulation of a standing acoustic wave across the probe volume. Following the approach by Hemmerling et al.[80] and solving the linearized thermodynamic equations the way it was proposed by Kozlov et al.[81] it is possible to characterize the overall medium response on the laser field and thermalization, and describe the evolution of a temperature and acoustic component over time. The model is presented in Eq. 3.10.

$$
LIGS\ signal \propto \left\{ M_i \cdot \left[cos(2\pi f_{osc}t) \cdot exp\left(-\left(\frac{t}{\tau_{tr}}\right)^2\right) - exp\left(-\frac{t}{\tau_{th}}\right) \right] + \right.
$$

$$
M_f \cdot \left[\left(\frac{k_f}{1+k_f^2} \cdot sin(2\pi f_{osc}t) + \frac{1}{1+k_f^2} \cdot cos(2\pi f_{osc}t) \right) \cdot exp\left(-\left(\frac{t}{\tau_{tr}}\right)^2\right) - \right.
$$

$$
\left. \frac{\left[exp\left(-\frac{t}{\tau_{th}}\right) - exp\left(-\frac{t}{\tau_f}\right) \right]}{\tau_f \cdot \left(\frac{1}{\tau_f} - \frac{1}{\tau_{th}} \right)} - \frac{1}{1+k_f^2} \cdot exp\left(-\frac{t}{\tau_f}\right) \right] +
$$

$$
\left. M_e \cdot sin\left(2\pi f_{osc}t\right) \cdot exp\left(-\left(-\frac{t}{\tau_{tr}}\right)^2\right) \right\}^2 \tag{3.10}
$$

M_i, M_f and M_e are dimensionless coefficients which scale the contributions to the LIGS signal as a result of instantaneous, finite energy exchange and electrostriction, respectively. The contribution from electrostriction is considered due to the presence of the strong electric fields provided by the pump laser beams. However, for the low fs-laser pulse energies used in the present work, this parameter is predicted to have insignificant influence on the modelled signals (paper VI) [70]. The quantity f_{osc} is the oscillation frequency of the acoustic wave, a key parameter that is extracted for prediction of the temperature T (see Eq. 3.12 in section 3.4.3). The acoustic transit time, $\tau_{tr} = \frac{W_0}{2\sqrt{2}v_s}$, determines the rate at which the oscillations of the signal will decay while travelling thought the probe volume using a beam with radius W_0 at the focus. Finally, the modulation of the acoustic waves due to thermal diffusion is described by the constant τ_{th}, given by

$$\tau_{th} = 2\left(\frac{\Lambda}{2\pi}\right)^2 \left(\frac{K}{\rho C_p}\right)^{-1}, \tag{3.11}$$

where K is the thermal conductivity, ρ is the gas density, C_p is the heat capacity at constant pressure, and $k_f = 2\pi f_{osc}\tau_f$ describes the decay of signal oscillations during the finite relaxation process with a time constant τ_f.

3.4.3   Temperature measurements

In this thesis project, the feasibility of fs-LIGS as a measurement technique for temperature has been investigated. For this purpose, temperature measurements have been performed in a heating gas tube (see the photograph in Fig. 3.15). It is an open T-shaped quartz gas tube surrounded by an electrical wire and insolation, where the gas is supplied from the bottom. The tube can heat the gas up to 800 K. The pump laser beams and the probe beam overlap in the measurement volume in the middle of the T-opening of the tube. A thermocouple type K is inserted through a small opening from the top of the tube, and is eventually located approximately 2-3 mm from the measurement volume. The temperatures evaluated from the LIGS data are compared with the corresponding temperatures measured by the thermocouple.
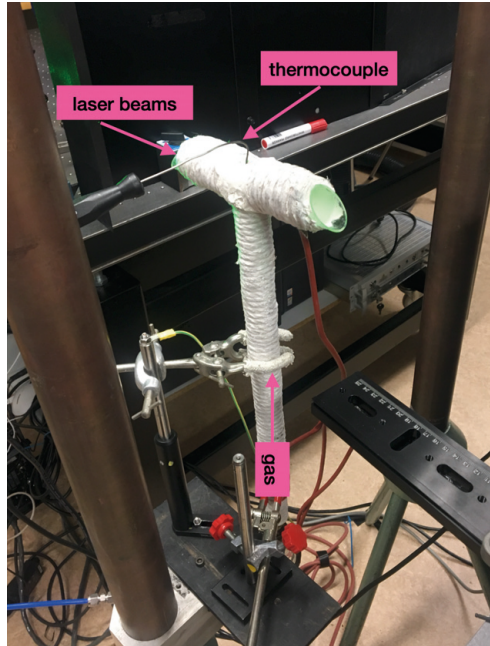

Figure 3.15. Photograph of a heating tube installed at the measurement volume.

For an ideal gas the sound velocity is given by $v_s = \sqrt{\frac{\gamma}{M} RT}$, where γ is the ratio (C_p/C_v) between the heat capacity at constant pressure C_p and the heat capacity at constant volume C_v, M is the molar mass, R is the ideal gas constant and T is the temperature, which can be expressed:

$$T = \frac{M}{\gamma R} \left(\frac{\Lambda}{t_{osc}} \right)^2 = \frac{M}{\gamma R} (\Lambda f_{osc})^2. \tag{3.12}$$

Thus, by determining the oscillation frequency of the signal, it is possible to extract the temperature of the gas as long as M and γ are known, which requires that the concentrations of the major species in the gas mixture are known.

The temperature accuracy increases with increasing number of resolved oscillation peaks in the signal. At high temperatures, diffusion of the gas in the probe volume becomes faster and the number of resolved oscillation peaks decreases, resulting in lower temperature accuracy. In this thesis work, it has been found that the commonly used method to determine the oscillation frequency from Fourier transform analysis of the LIGS signal is not well suited due to the relatively low number of resolved oscillation peaks. Instead, determining the oscillation frequency f_{osc} by fitting the model using a least-square fitting routine has proven to give a more accurate prediction of the gas temperature (paper VI) [70].

4 Applications of the diagnostic techniques

This chapter expands and complements the results presented in papers I-VI, and adds some interesting observations. The section about femtosecond two-photon-laser induced fluorescence presents some additional measurements, demonstrating the absence of photolytic interferences in the experiments with H-atom LIF. Furthermore, non-published results from recent experiments on simultaneous single-shot imaging of O and H atoms in turbulent flames are presented as well.

Since publishing the three papers on backward lasing (papers II-IV), additional research has recently been done in the direction of understanding the nature of the lasing generation. Recent results indicate that superfluorescence might be an important contribution to the backward lasing signal from hydrogen atoms in flames.

This chapter also contains important information, based on practical experience from laboratory work, on alignment of both hybrid fs/ns CARS and fs-LIGS experiments. At the end, some observations, not covered in the paper about fs-LIGS (paper VI), namely signals from a plasma grating and challenges in temperature evaluation, are discussed.

4.1 Femtosecond two-photon-excited fluorescence measurements

In this section, recent, unpublished, results on simultaneous detection and imaging of hydrogen and oxygen atoms in flames using fs-TPLIF are shown and discussed. However, before discussing these results, some data demonstrating that photolytic interferences are negligible in the current experiments are presented.

4.1.1 Photolytical interferences in TPLIF measurements

The experiments were conducted in a flame on a modified McKenna burner, which consists of an inner central tube of 2 mm diameter and an outer porous plug having

a diameter of 60 mm. Separate premixed CH_4/air gas mixtures entered the central tube and the surrounding plug through mass flow controllers. A photo of the flame is shown in Fig. 4.1. The central jet flame was stabilized on the burner by an outer flame generated on the plug. The equivalence ratio was $\phi = 0.9$ for the outer flame and $\phi = 1.3$ for the inner jet flame.

An image of the fluorescence signal from H atoms present in the laminar CH_4/air flame is shown in Fig. 4.1a. A thin laser sheet was formed using a 300 mm cylindrical lens, transecting through the centre of the jet flame about 20 mm above the burner surface. Fluorescence from H atoms, exited by a 205-nm fs-laser beam, can be observed primarily in the reaction zone of the flame. Several accumulated images of H-LIF were taken for different laser pulse energies, using an intensified CCD camera (iCCD) equipped with a 655-nm bandpass filter for suppression of flame luminescence and background. Cross section profiles of the recorded images are shown in Fig. 4.1b. The different colours correspond to different laser output energies, measured with a power meter just after the cylindrical lens. Note that the radial profiles are normalized to the peak signal intensity. It is evident that the shape of the profiles remains unchanged and no significant deviation is observed as the laser pulse energy is increased, similar result was observed by Kulatilaka et al.[22]. Hence, this result suggests that no photolytic interferences are induced and, hence, we capture only fluorescence from atomic hydrogen that is naturally present in the CH_4/air flame. It was concluded that the excitation laser intensity should be kept below 3×10^{14} W/m^2 to ensure that photolytic interferences are not induced.
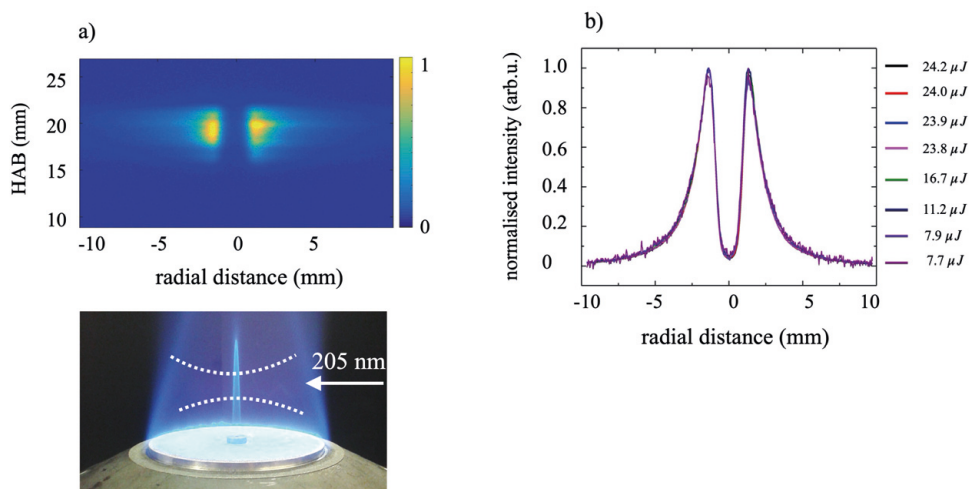

Figure 4.1. a) TPLIF image of H signal in CH4/air flame (upper panel), picture of a flame stabilized on the McKenna burner (lower panel). b) Radial signal profiles recorded for different laser pulse energies. The cross section area of the laser sheet is estimated to be 0.7 mm^2.

In order to ensure that the hydrogen fluorescence was induced by a two-photon absorption process, a laser-pulse-energy-dependence study was performed. Hydrogen fluorescence intensity versus laser pulse energy is plotted in a log-log diagram as shown in Fig. 4.2. The red line corresponds to a linear fit to the data points (empty circles). The slope of the fitted line is close to 2, which shows that the LIF signal increases linearly with the square of the laser pulse energy, which confirms two-photon excitation. This result also suggests that photoionization, photolytic production of hydrogen atoms, and stimulated emission are insignificant within the present interval. This is perhaps not surprising as the pump laser was focused with a cylindrical lens, forming a laser sheet, which keeps the laser intensities (power per unit area) low enough for these processes to be observable.
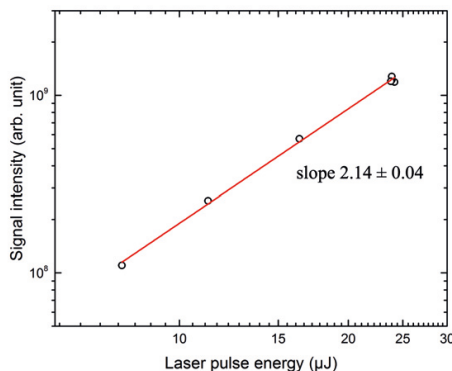

Figure 4.2. Laser pulse energy dependence of the 656 nm TPLIF signal. The red line is a fit of $S \propto I^k$, where the best fit is obtained for k=2.14±0.04.

4.1.2 Simultaneous femtosecond two-photon-excited fluorescence imaging of O and H in turbulent flames

In this work, single-shot simultaneous imaging of hydrogen and oxygen atoms is performed for the first time and demonstrated in various turbulent flames. Qualitative two-dimensional images of oxygen and hydrogen fluorescence for different ϕ values of a CH_4/O_2 jet flame stabilized on a McKenna burner (described above) are achieved by focusing the laser beam into a 4 mm high sheet. A cylindrical lens with $f = 150$ mm is used to focus the 205 nm laser beam, with a pulse energy of $\sim 35 \mu J$, for excitation of H atoms, while another cylindrical lens, with $f = 300$ mm, is used to focus the 226 nm laser beam, with a pulse energy of $\sim 45 \mu J$, for excitation of O atoms. The laser beams intersect at a small angle ($< 1°$) in the probe volume. Two externally triggered iCCD cameras are used to capture 656 nm and 845 nm fluorescence emission for H and O atoms, respectively. The acquisition of the two cameras is synchronized, and the two excitation pulses arrive at the probe volume with a constant temporal separation of only a few nanoseconds, which is much less than the time scale of the turbulent chemistry of the flame. Proper

synchronization between the cameras is confirmed by comparing the shot-to-shot variation of the flame chemiluminescence captured simultaneously with both cameras.

The stoichiometry of the flames is varied from lean to rich flame (from $\phi = 0.8$ to $\phi = 1.3$). The irregular motion of the flame flow is described by the Reynolds number (Re) for the CH_4/O_2 mixture. The total flow was 14 l/min and Re > 8000 for all investigated ϕ values, which puts the experimental condition in the turbulent regime. Obviously, a more accurate characterization of the flow field and the degree of turbulence, requires calculations of the Kolmogorov, chemical reaction, and integral time scales, and positioning the estimated conditions into the Borghi diagram.

The results are presented in Fig. 4.3. Experimental and simulated radial concentration profiles of H and O are shown Fig. 4.3a-c, corresponding to $\phi = 0.8$, $\phi = 1$, and $\phi = 1.3$, respectively. Experimental (solid) and simulated (dashed lines) profiles are qualitatively consistent. As can be seen, the experimental profiles for all ϕ values repeat the trends of the simulated profiles, i.e. they show similar growth and decay pattern.

The fluorescence data corresponding to the experimental profiles is taken at 1 mm above the burner surface, where the flame is assumed to be relatively stable. Each experimental signal is an average of 100 single-shots taken by the two different iCCD cameras, equipped with appropriate narrow-band transmission filters for H and O fluorescence, respectively. Each single-shot image was compensated for the spatial inhomogeneity of the laser beam profile by dividing each file with a profile extracted from measurements in laminar flames. The data matrices corresponding to each single-shot image have also been adjusted, in order to account for differences in magnification, degree of rotation, and translation between the H and O images taken with the two different cameras. The concentration (vertical axis) values are obtained through calibration measurements in a laminar flame of $\phi = 1.2$.
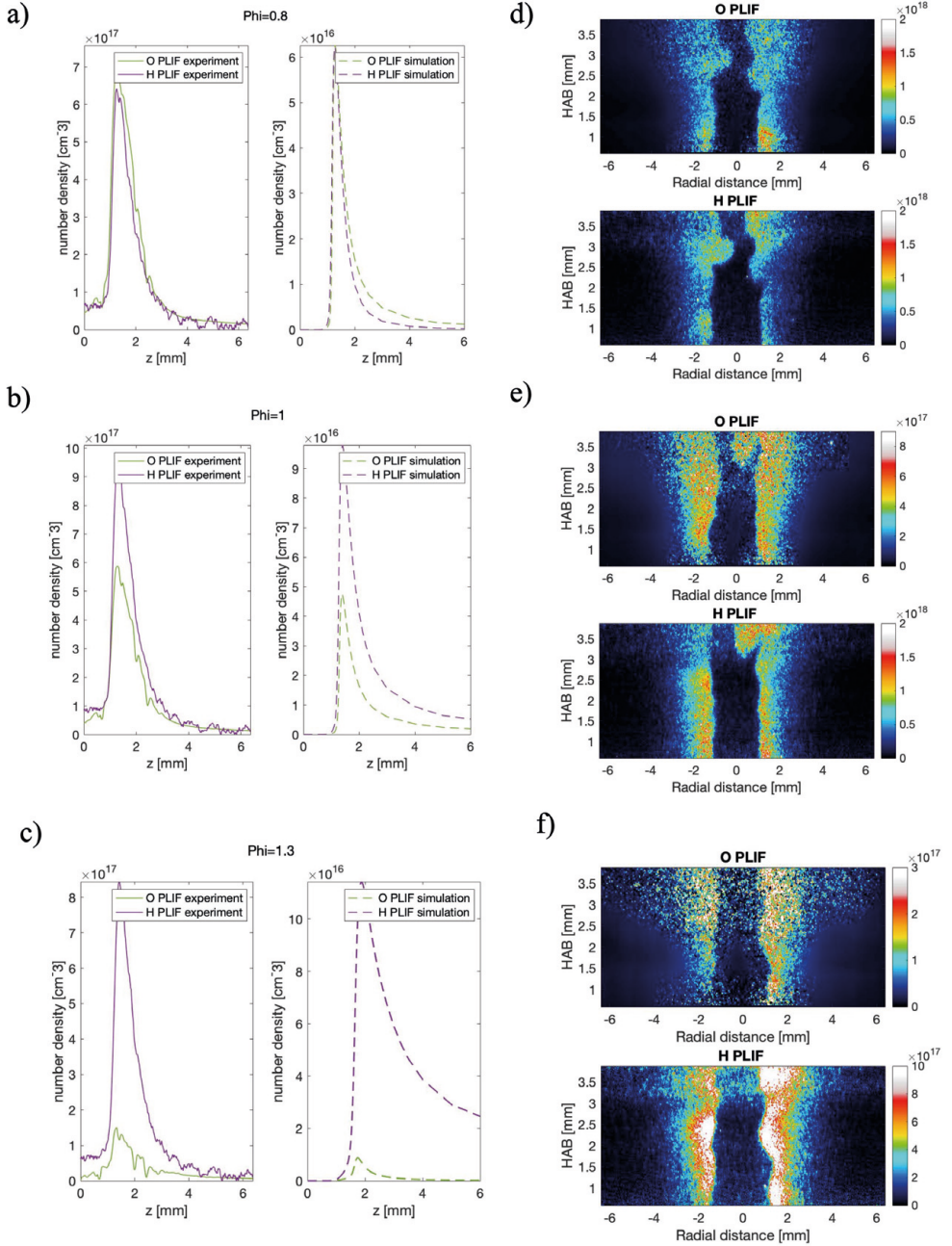
Figure 4.3. Experimental and CANTERA software simulation data (dashed lines) compared for O and H PLIF for different phi values, a) $\phi = 0.8$, b) $\phi = 1.0$ and c) $\phi = 1.3$. 2D single-shot images of O and H atoms in a turbulent flame for different phi values d) $\phi = 0.8$, e) $\phi = 1.0$ and f) $\phi = 1.3$.

The simulations are based on laminar flame conditions. At high flow speeds such a flame would stabilize far away from the burner. Therefore, the simulated H profile has a much longer decay compared to the experimental profile for the rich flame (compare the purple-coloured curves in Fig. 4.3c). The discrepancy might also be due to variation in the laser sheet thickness. Another observation that can be made from Fig. 4.3a-c is that the experimental H profile decays at around 2.5 mm radial position regardless of ϕ value.

At a first glance it seems that simulations and experimental data agree very well, however, there are some discrepancies. Initially, it was assumed that close to the burner (at 1 mm height above the burner) the turbulence should not affect the profiles very much, which was not a proper assumption. With turbulent flows, the fuel enters the burner with high flow velocity, which results in a rapid formation of radicals. Therefore, some discrepancies between the simulated (laminar) and experimental (turbulent) profiles are expected.

Two-dimensional single-shot images recorded in the flames are presented in Fig. 4.3d-f. The colorbar (cm^{-3}) reflects the concentrations for each ϕ value for both the O and H data. The shape of the structures present in the H and O images agree very well, which confirms that the same turbulent event is captured. The images indicate that the H-atom distributions extend further into the unburned gases compared with the corresponding O-atom distributions, which might be explained by the higher diffusivity of the lighter H atoms, allowing them to penetrate deeper into the unburned region.

4.2 Backward lasing

In the work presented in paper III the dominating mechanism responsible for lasing is suggested to be amplified spontaneous emission (ASE) [48]. However, in the forward direction, the results suggest that ASE occurs simultaneously with a four-wave mixing (FWM) process and the signal is also found to be stronger in the forward direction, as can be seen in Fig. 4.5. One result that supports that an FWM process is involved in the forward-lasing is the observed spectral broadening, as can be seen in Fig. 2 in paper III. Such spectral broadening is not observed for the backward lasing, and therefore it was concluded in paper III that this emission is dominated by ASE.

Since ASE and superfluorescence (SF) have several properties in common, such as the presence of a distinct pump laser intensity threshold, gain provided by population inversion, low divergence, and high signal directionality. These similarities make it difficult to determine the mechanism behind the generation of lasing. The main difference between ASE and SF is that the latter process requires close proximity between the excited atoms to emit collectively, which is not the case

for ASE. Pure SF thus requires that all excited atoms emit cooperatively, which in turn demands that they must be able to interact strongly with each other in a time that is short compared to their dephasing time (T_2). Recent work from our research group provides new experimental results that indicate the occurrence of SF from atomic hydrogen in a CH_4/O_2 flame (see related work, paper XII) and the following section discusses these recent findings.
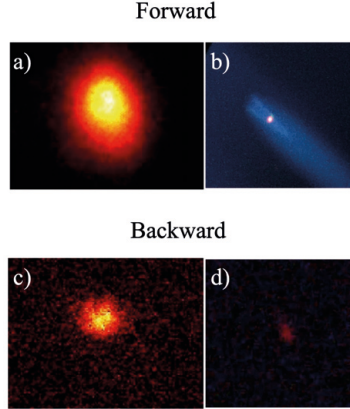

Figure 4.5. Spatial profiles of a) forward and c) backward lasing recorded with CCD camera, and corresponding photographs taken by a phone camera for b) forward and d) backward lasing, respectively.

4.2.1   Signature of SF

As discussed in section 3.2.2, SF exhibits a few characteristic properties that differ significantly from ASE, namely, the peak emission intensity depends quadratically on the number density of the interacting atoms, the time duration of the SF pulse is inversely proportional to the number density of interacting atoms, and the SF pulse is emitted after a time delay τ_D which is proportional to $N^{-1/2}$ [51, 82, 83]. Studies of the forward lasing signal generated by oxygen atoms in a flame, presented in [53] (paper XI), show that the lasing signal is emitted with a delay that decreases with increasing concentration, which is a typical signature of SF.

We have recently performed similar measurements for hydrogen atoms (see related work, paper XII). In this work, the time delay τ_D for both forward and backward lasing pulses is studied as the input pump laser pulse energy is varied, effectively changing the concentration of excited hydrogen atoms. The result of this study, which is shown in Fig. 4.6b, indicates that the lasing pulse exhibits SF nature. It is noteworthy that a similar dependence has been observed in the work presented in paper IV. While keeping the focus of the pump laser beam midway between two flames, the distance between the flames was varied. The recorded backward lasing

signals (normalized) are shown in Fig. 4.6a. The pump laser intensity decreases with increasing distance from focus, which means that the number density of excited atoms also decreases with increasing distance to focus. As can be seen in Fig. 4.6a, the duration of the lasing signal becomes longer with decreased pump laser intensity. The observed temporal broadening of the backward lasing pulse may thus be an indication of SF, for which the time duration to build up the atomic coherence increases with decreasing concentration of excited atoms.
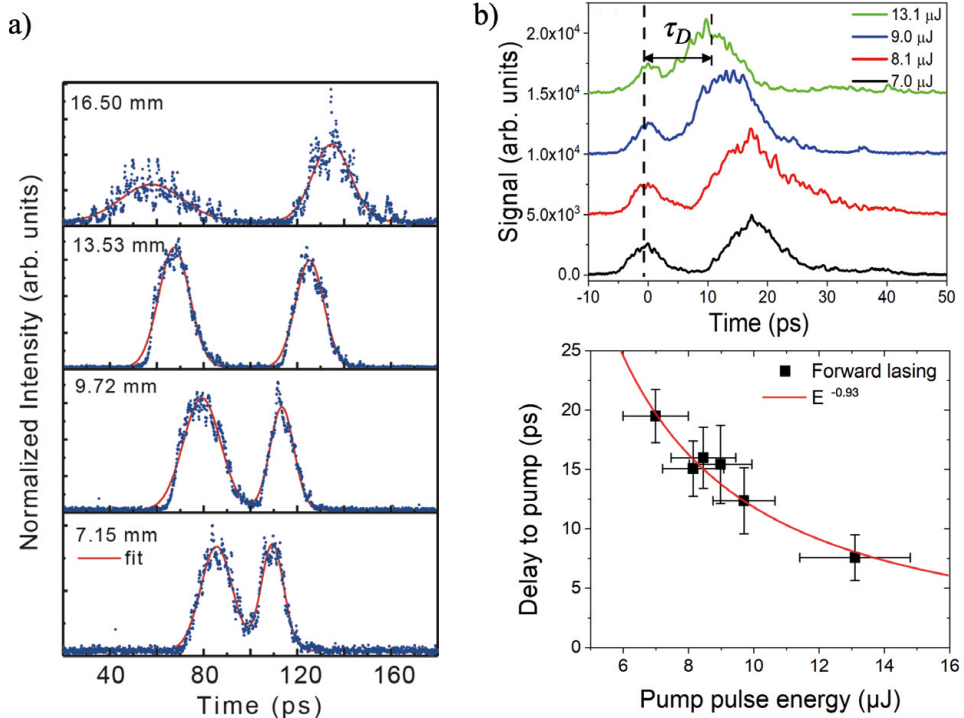

Figure 4.6. Signatures of SF. a) Single-shot temporal profiles of a H-atom backward lasing for four different distances between two flames (paper IV) [46]. b) Temporal profiles of forward lasing signals from H atoms at four different pump laser pulse energies. The lower panel shows the delay, τ_D, of the forward lasing pulse as a function of a pump pulse energy. The red solid line corresponds to the best fit (see related work, paper XII).

Occurrence of a collective emission can be categorized in the various regimes, shown in Fig. 4.7 [54, 84]. Single-pass gain through the excitation volume of length L varies with the collisional dephasing time T_2 as $gL = \frac{2T_2}{\tau_r}$ [84], where τ_r is the cooperative lifetime, or general lifetime of a collective emission signal in the cross-sectional area A expressed as $\tau_r = \frac{8\pi AT_1}{3N\lambda^2}$ [84]. Where T_1 is the spontaneous emission decay at the wavelength λ, and N is a total number of excited atoms in the gain

volume. The delay time for the SF is expressed as $\tau_D = \tau_r \left[\frac{1}{4} \ln\sqrt{2\pi N} \right]^2$ [84]. Under the experimental conditions presented in the related work (paper XII) it is assumed that the nature of the lasing emission falls into the SF regime.

It can be seen from the figure that SF regime is divided into several sub-regimes labelled pure SF, weak-oscillatory SF, strong oscillatory SF and damped SF. Collisional dephasing described by T_2 in damped SF regime is not sufficient enough to prevent the system from building the macroscopic dipole moment and

$T_2 > (\tau_r \tau_d)^{1/2}$. If the total number of atoms N is larger than the maximum number of atoms which can emit cooperatively $N_c = \frac{8\pi c T_1 A}{3\lambda^2 L}$ [84] the SF signal experiences a temporal ringing behaviour, which was not the case for the H-atom SF (paper XII), however, it was be observed in the O-atom SF signal [53] (paper XI).
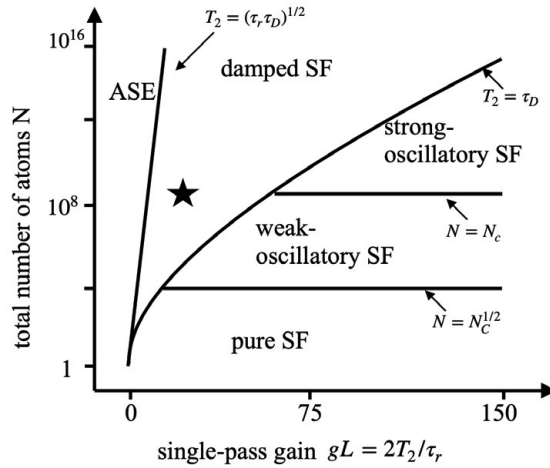

Figure 4.7. Regimes of collective lasing emission (adapted from [84]). Experimental parameters for the H-atom SF (see related work, paper XII) correspond to the damped SF regime, which is marked by the star.

As an extension to the work presented in paper IV, a flame experiment with varying ϕ values in the probe volume was performed. The hydrogen atom concentration profile depends on the ϕ value, as can be seen in the simulated profiles shown in Fig. 4.8a. Maximum hydrogen concentration is obtained for $\phi = 1.2$. The experiments were done in two welding flames separated by 7.15 mm. As can be seen in in Fig. 4.8b, presenting the results, the shape of the backward lasing signal varies with the ϕ value. The two peaks, corresponding to the two flames are well resolved for $\phi = 0.8, 1.0,$ and 1.2, but not for $\phi = 0.6$.
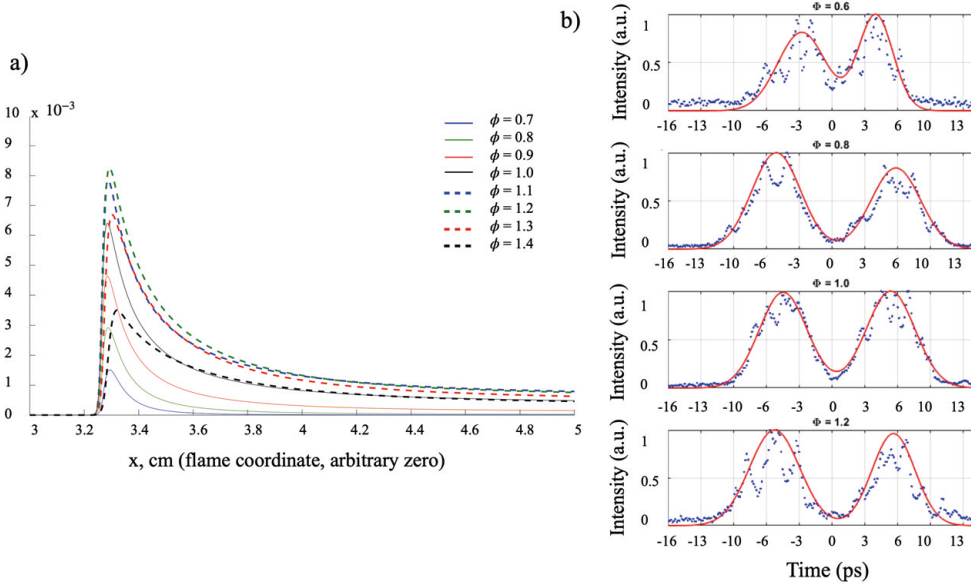
Figure 4.8. a) H concentration profiles for different ϕ values of a CH_4/air flame, simulated using CHEMKIN. b) Experimental results of lasing pulse duration for different ϕ values for CH_4/O_2 flame.

4.3 Hybrid fs/ns CARS and fs-LIGS study

Paper V [68] on hybrid fs/ns CARS demonstrates a breakthrough for applied gas-phase diagnostics. For the first time fully spectrally and temporally-resolved RCARS signals were recorded in a single-shot acquisition using a spectrograph and a streak camera. Interesting phenomena, such as Stark effect and beating, were briefly reported on in the paper. Paper VI [70] on fs-LIGS demonstrates for the first time a possibility to realize the LITGS technique based on multi-photon excitation. The technique was demonstrated in a nitrogen gas flow at temperatures varying from room temperature to 750 K. At increased fs-laser pulse energies a plasma grating phenomenon was observed. Some additional experimental aspects and results, not included in papers V and VI, are discussed below.

4.3.1 Aligning two fs-laser beams for CARS and LIGS experiment

One major challenge with nonlinear techniques, like CARS and LIGS, is alignment of the pump beams (pump/Stokes beams). With the use of fs-laser pulses this challenge becomes even greater, since this adds significant difficulty in achieving temporal overlap of the two pulses. First, the two laser beams, both ω_1 and ω_2 in Fig. 4.9a, needs to be parallel before the lens. This alignment is optimized by

checking that they have the same separation in the near and the far field. With the lens in place, the criteria for a good overlap in time and space is that an interference pattern is formed on a screen positioned at some distance beyond the intersection, as illustrated in Fig. 4.9a. In order to observe the pattern, the laser energy for both ω_1 and ω_2 should be relatively high, around 2 mJ.
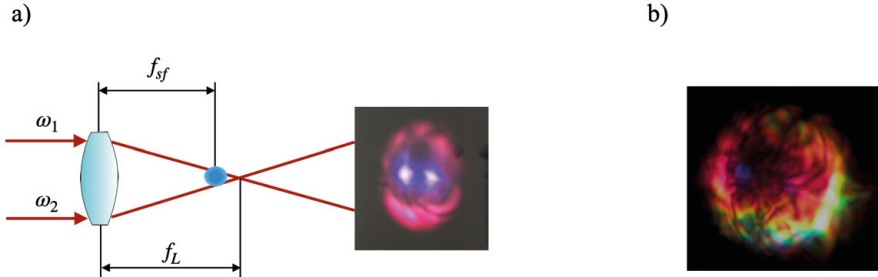
a)   b)

Figure 4.9. a) Two fs-laser beams ω_1 and ω_2 form interference pattern (image taken by a phone camera) when they are ovelapped in time and space, b) supercontinioum production from two overlapped fs-laser beams ω_1 and ω_2 in time and space, image taken by a phone camera.

With increased laser pulse energy, the laser beams ω_1 and ω_2 can experience self-focusing, and as a result, form filaments. Consequently, some more colours will occur in the observed interference pattern, as shown in Fig. 4.9b. Hence, for high laser pulse energies, there will be two focal points to consider, one due to self-focusing, f_{sf}, and one corresponding to the focal length of the lens, f_L. Since the two pump beams cross at the focal length of the lens, f_L, it is important to align the probe beam so that it intersects the pump beams at f_L, not at f_{sf}. Another aspect that should be taken into account is that the pump beams will have different foci due to self-focusing if they have different pulse energies, which will add some complexity to the alignment procedure.

4.3.2   Temporal alignment of the probe pulse in hybrid fs/ns CARS

A temporal diagram of the hybrid fs/ns RCARS concept is illustrated in Fig. 4.10a. Two Fourier-transform limited fs-pulses, pump (ω_1) and Stokes (ω_2), overlap in time and space and generate rotational Raman coherences, which are probed by a ns-single-mode probe pulse (ω_3). Figure 4.10b illustrates the position of the RCARS signal, i.e. the Raman coherences, relative to the ns-probe pulse both in time and wavenumber. As can be seen from both panel a and b in the figure, the probe pulse is positioned in time so that its maximum intensity coincides with the two fs pump pulses. In this way, the RCARS signal is maximized and the temporal decay of the probed coherences, whose duration is on the order of 100 ps, is minimally affected by the temporal shape of the ns probe pulse, which is virtually

flat in the vicinity of its maximum. In the spectral domain, the probe pulse is very narrow, since it is provided by a single-mode laser. The effective spectral bandwidth of the excitation of Raman coherences is a convolution between the pump and Stokes laser pulses, which implies a spectral coverage of $\sqrt{2} \times 150\ cm^{-1} = 210\ cm^{-1}$ (FWHM). The 3-D diagram shown in Fig. 4.10b, corresponds to measurements in ambient air, averaged over 200 single-shots. As can be seen, the CARS signal coincides with the peak of the ns-probe pulse, which corresponds to time zero.
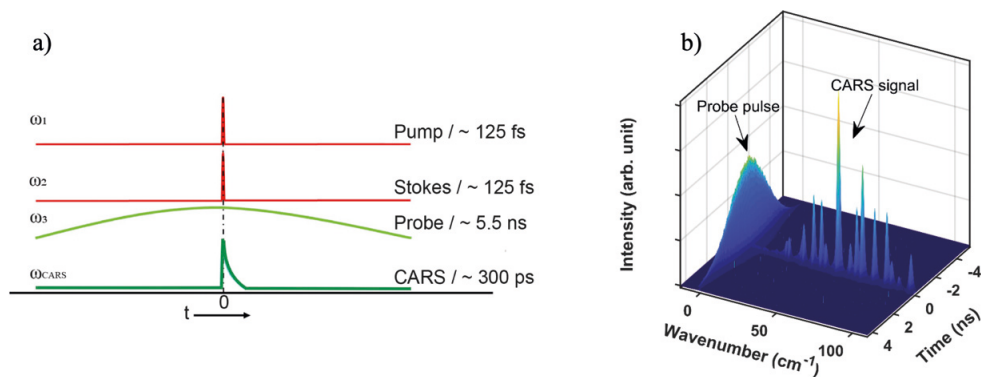
Figure 4.10. a)Temporal diagram of fs/ns RCARS [68]. b) Experimentally recorded RCARS signal in air relative to the ns-probe pulse [85].

4.3.3 Stark splitting in RCARS

Stark effect occurs when atoms/molecules are perturbed due to the presence of a strong external electrical field, and it leads to interesting phenomena from a fundamental molecular physics point of view, such as shifting the energy levels (Stark shift) and causing degenerate levels to split (Stark splitting). A detailed and fundamental description of the Stark effect in CARS spectroscopy is presented in the papers by Rahn et al. [86] and Farrow and Rahn [87]. Reference [86] concerns Stark shift in vibrational CARS through interaction between the applied field and the polarizability derivative, while [87] discusses Stark splitting of pure rotational Raman transitions through interaction between the applied field and the polarizability anisotropy. Clearly, with the fs laser pulses used in the present work, the rotational Raman coherences may be perturbed by the high electrical field imposed on the molecules by these laser pulses. Stark splitting, resulting in additional spectral lines, was observed in the work presented in paper V for a laser intensity of 1 TW/cm². Increasing the laser intensity to 10 TW/cm² generates significantly more pronounced Stark effect, which is illustrated in Fig.4.11. Spectral broadening of the rotational Raman coherences is obvious; however, the effect is essentially vanished after around 400 ps. This observation might indicate a

possibility to obtain temperature information by analysing the signal remaining after 400 ps (see Fig. 4.11b). However, this would require further experimental studies and modelling work.
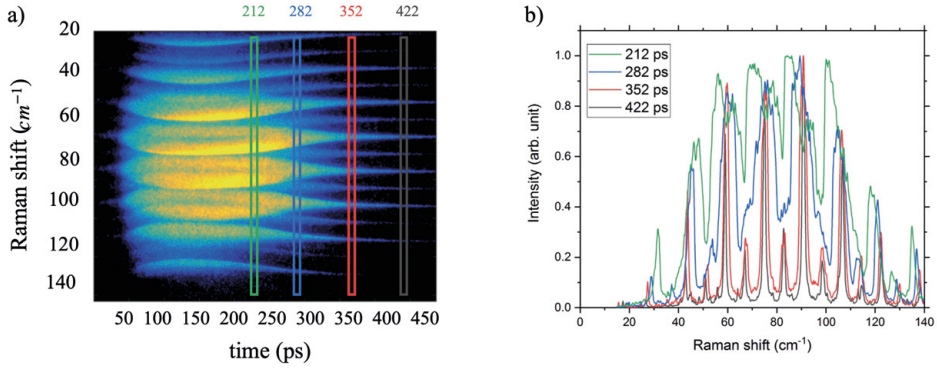

Figure 4.11. a) Single-shot data showing perturbed Raman coherences in N_2 gas due to Stark effect. b) Vertical cross sections, i.e. CARS spectra, at four different temporal positions, extracted from the data shown in a).

4.3.4 Possibility of observing LIGS signal during CARS experiment

It is obvious that LIGS and three-beam CARS experimental configurations are quite similar to each other. If the polarizations of the pump/Stokes beams are the same there is a chance of establishing an efficient grating pattern and observing a LIGS signal in a planar BOXCARS configuration [88], even though the probe beam does not enter the crossing region of the pump/Stokes beams at the first-order Bragg angle (see section 3.4). Indeed, we observed a strong green signal, delayed by 20 ns relative to the CARS signal, and this beam was used to align the spectrometer and a streak camera during the CARS measurements. This interesting observation triggered the idea of performing the fs-LIGS experiment.

4.3.5 Plasma grating dynamics in fs-LIGS

In paper VI it is reported that increasing the laser pump pulse energy above 700 µJ changes the shape of the thermal LIGS signal in N_2 gas substantially. It is no longer possible to see a clear modulation pattern since the hydrodynamics in a plasma grating is significantly different compared to a thermal grating. In order to bring some light on the dynamic processes in a plasma grating, one of the 125-fs laser pump pulses was delayed relative to the other one. The results are shown in Fig. 4.12, where zero delay signifies the time when two 125-fs laser pulses are temporally overlapped. One would perhaps expect that the signal should disappear

after about 175 fs (convolution of two 125 fs-laser beams) but it is present for much longer delays, even at a nanosecond delay.
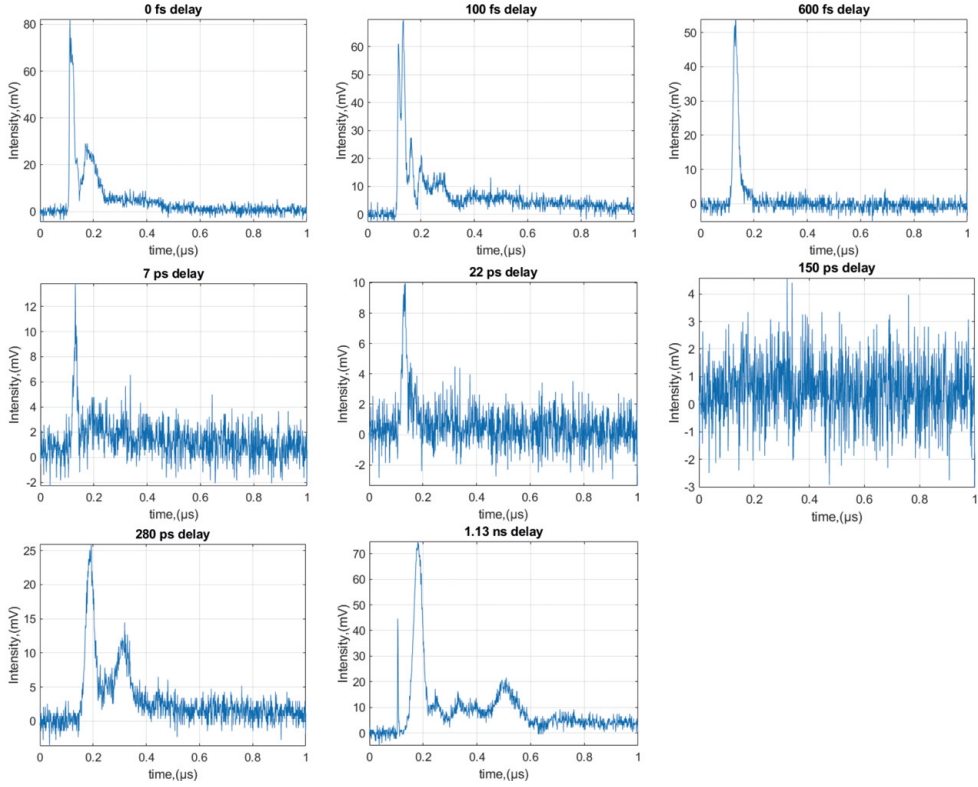

Figure 4.12. Single-shot LIGS signals recorded with pump pulses of 2.5 mJ pulse energy, exhibiting the dynamics of a plasma grating for different delays between the pump pulses. The signal completely disappears with one of the pump beams blocked. Nutral density filter were employed for the signals before 150 ps delay.

The data in the Fig. 4.12 presents randomly selected single-shot measurements. It is difficult to draw any definite conclusions from these results, but a few observations can be done. For the two delays, for which the two pump pulses still overlap (0 and 100 fs delay), the time-resolved LIGS signal lasts for a few hundred ns. For the delays 600 fs, 7 ps, and 22 ps, the signal is essentially a single peak with a duration of tens of ns, and the signal intensity decreases with increasing delay. At a delay of 150 ps, the signal has basically disappeared. Then for even larger delays, such as 280 ps, a clear signal is present again, now containing two rather distinct peaks. At even longer delay, i.e. 1.13 ns, an even stronger signal is observed, containing a high initial peak followed by several lower peaks within a time period of 300-400 ns. The behaviour that the LIGS signal dies off and comes back at some

delay could perhaps be dynamics caused by collision-assisted free electron recombination processes in the gas [89]. It should be noted that the plasma grating is generated by two crossing filaments and the interference fringes might be washed out by a combination of collision-assisted free electron recombination and ambipolar electron diffusion [89]. To understand the plasma grating dynamics under the conditions prevailing in our study, and find out whether there is any potential for diagnostics, like thermometry, much more research is needed. It would, for example, be interesting to repeat the measurements with a detector providing higher temporal resolution, for example streak camera, which offers picosecond resolution.

Figure 4.13 shows results from a study where LIGS signals were recorded for different temperatures in air (red line), nitrogen (green line), and argon (blue line). The pump pulses were temporally overlapped and the pulse energy was 2.5 mJ. As evident from the figure, the peak intensity of the LIGS signal does not change significantly when the temperature is changed. This observation is valid for all three gases. However, it can be noticed that the number of oscillations decreases with increasing temperature due to thermal diffusion, which is consistent with the results from LITGS measurements at 700 µJ pump pulse energy, as can be seen in Fig. 7 of paper VI [70].
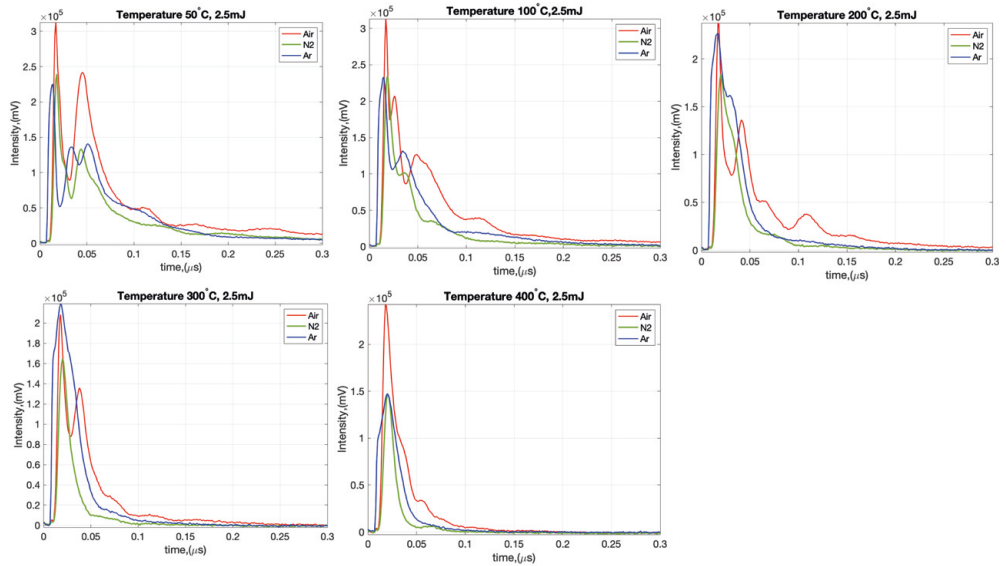

Figure 4.13. Single-shot signals from a plasma grating at different temperatures, ranging from 50 to 400 °C (373 K – 753K) in air, N_2 and Ar gases. The pump laser pulses were temporally overlapped and the pulse energy was 2.5 mJ.

4.3.6 Temperature evaluation for the fs-LIGS signal

At elevated temperatures, it takes longer time for the gas to be heated in a tube, shown in Fig. 3.15 and, in order to reach steady-state temperature conditions the gas flow must be relatively low (< 5 l/min). However, during the recording time of the signal with the PMT (photomultiplier tube) and the oscilloscope (~ 10 sec for 100 accumulations) the temperature might vary. The data can be recorded by a hardware accumulation and by a single-shot recording. The hardware accumulated signal does not explicitly correspond to one specific oscillation frequency, since the temperature changes during one accumulation period. During the accumulation process the oscilloscope reads out every single-shot, stores it and after accumulating 100 shots it does the averaging. However, each 100 sweep has its weight constant and noise signal and during the accumulation, the noise level might be accumulated in a random manner, which increases the uncertainty of the acquired data. The temperature precision of the fs-LIGS technique was investigated by recording 100 single-shot signals from nitrogen gas at two temperatures, 373 and 673 K. The results are summarized in Fig. 4.14. The model, described in section 3.4.2, was fitted to each single-shot recording and the retrieved oscillation frequencies and corresponding evaluated temperatures are plotted in histograms, as shown in panels a) and b). As can be seen, the histograms indicate that the data follows normal distributions. The standard deviation, i.e. the uncertainty, increases from merely 3 K, at 373 K (Fig. 4.14a), to 41 K, at 673 K (Fig. 4.14b). Example of single-shot LIGS signals for the corresponding temperatures are presented in Fig. 4.14c.
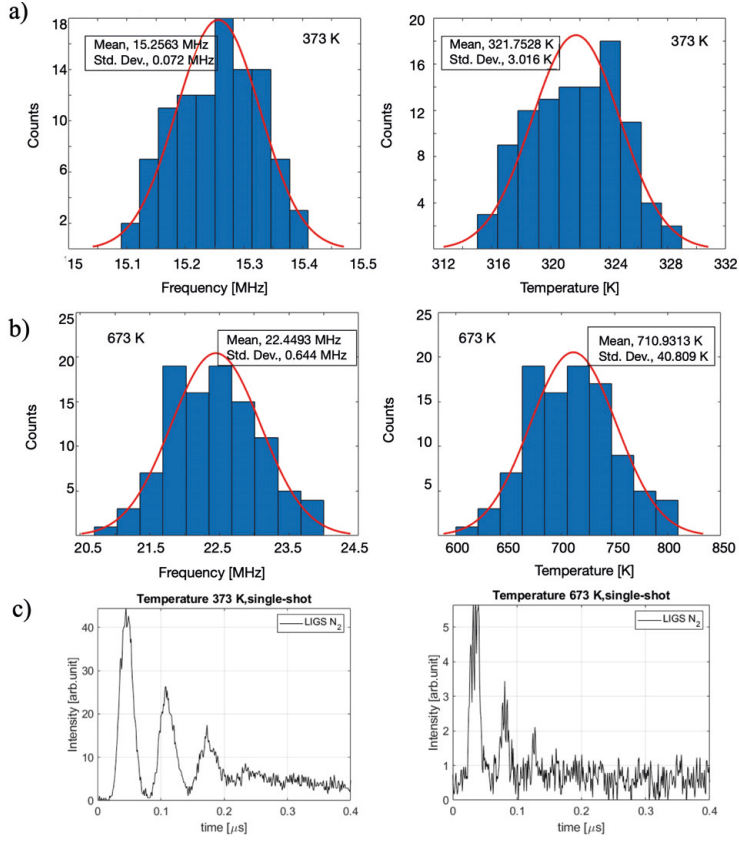
Figure 4.14. Histogram of evaluated oscillation frequencies (left) and temperatures (right) obtained for 100 single-shot LIGS measurements in N_2 gas at a) 373 K and b) 673 K, respectively. c) Corresponding single-shot LIGS signals recorded in N_2 gas at 700 μJ laser pulse energy at 373 K (left) and 673 K (right).

5 Summary and future perspectives

The aim of the work covered in the thesis project was to develop new and improve already existing laser-based diagnostic techniques based on ultrafast laser excitation. The results provide valuable insights for research on gas-phase phenomena. This chapter is a summary of the main contributions of the developed techniques, presented in papers I-VI. Future perspectives for the developed techniques are discussed in the chapter as well.

Femtosecond two-photon laser-induced fluorescence

The two-photon fs-LIF technique based on pulses of very high peak power, yet with relatively low pulse energy, provides an excellent multi-photon excitation mechanism, virtually free from photolytic interferences. Despite using a laser with broad spectral bandwidth for a narrow atomic/molecular transition, the excitation is efficient due to a large number of combinations of photon pairs driving the transition. These capacities of the fs-two-photon LIF technique were first tested and demonstrated in the work presented in paper I, in which two-photon excited fluorescence of the CO molecule in CH_4/air flames was measured. As discussed in the paper, deep-UV laser excitation pulses, if focused by a spherical lens, might introduce a loss mechanism due to photoionization. The laser beam intensity in the vicinity of the beam focus is high enough to cause ionization, resulting in a loss of excited CO molecules, manifested by a dip in the recorded fluorescence radial profiles. However, this issue is not observed when performing 2D imaging of atomic trace species using a laser sheet. Measurement results, presented in section 4.1.2, of simultaneous interference-free femtosecond LIF imaging of H and O atoms, demonstrate that fs two-photon LIF is an excellent tool for visualizing these species in turbulent flames. It is even demonstrated that the species concentrations can be quantified through calibration measurements in well-characterized laminar flames.

The technique has great potential to be applied for measuring different atomic species and molecules in industrial combustion chambers, for example in new combustion devices based on renewable fossil-free fuels, such as bio-fuels, hydrogen gas, and ammonia. A major challenge with the technique is the aforementioned potential photodissociation of molecules containing the species of interest, which might lead to false-positive measurement results. Up to now, photolytic interference has been assessed by studying the spatial shape of the

fluorescence signal, often recorded in a laminar flame. If the normalized fluorescence profile remains the same for laser pulse energies up to a certain value (see Fig. 4.1b), then the detection is deemed photolysis-free for pulse energies below that upper limit. Even though, this strategy checks a necessary condition that needs to be fulfilled for photolysis-free detection, it is not a complete proof. For example, if the precursor molecule, is spatially overlapping with the species to be measured, then the fluorescence profile will not change even if the species of interest is produced by photolysis. Although this complication can be remedied by confirming that the profile, in each point, follows a quadratic dependence on the laser pulse energy, a better understanding of photolytic effects in fs two-photon LIF is needed. As a potential future experiment, sketched in Fig. 5.1, a pump-probe study with one weak laser pulse tuned on-resonance ($h\nu_{on}$), i.e. the probe, and another laser pulse tuned slightly off-resonance ($h\nu_{off}$), i.e. the pump, can be performed. The off-resonance pump will then be able to photodissociate the precursor molecule (AB), but not excite the species of interest (A). Now, the pump laser pulse energy is gradually increased. As long as the fluorescence signal from A, obtained by the probe pulse, stays the same, no photolytical production of the species of interest (A) is taking place. By varying the delay between the pump and probe pulse, it is possible to measure the time (τ_{ph}) it takes for the photodissociation process to produce the fragment interfering with the species of interest. If this time is found to be larger than the duration of the fs pulse, then that could be the main reason why photolytical interference usually is not a problem in fs two-photon LIF (but definitely for nanosecond excitation).
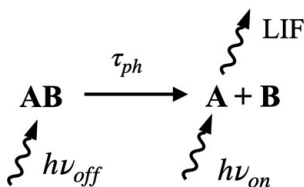

Figure 5.1. Schematic representation of a potential pump-and-probe LIF experiment. AB is the precursor molecule, while A and B are two fragments created by photodissociation. A is the species of interest, i.e. the atom one wants to measure. The probe laser pulse induced fluorescence from the fragment A.

Femtosecond two-photon excited lasing

A coherent backward-directed signal beam that carries an atomic fingerprint from a remote measurement region straight back to the detector is demonstrated in the fs-backward lasing studies, allowing for single-ended diagnostics. The overall goal of this research is to develop a method, which can be applied for remote-species

detection, such as gas leakages, atmospheric pollutants, and other hazardous species. Development of backward lasing based on two-photon excitation for stand-off measurements of H atoms in flames is presented in papers II-IV. Paper II covers the first results of H atom lasing observed in the backward direction. Here it was discovered that the lasing effect has a pump laser energy threshold for both the forward and backward signals, low divergence, lasing pulse energy on the pJ scale, and lasing pulse duration on the ps scale. Paper III discusses a possible gain mechanism responsible for the lasing effect of atomic hydrogen. The results show that the bandwidth of the forward lasing pulse is significantly broader compared to the backward lasing pulse, and the forward lasing signal is found to be about one order of magnitude stronger than the backward lasing signal. This is explained by the traveling wave excitation in the forward direction attributed to the pencil-shaped gain medium. Paper III, published in 2019, is based on the hypothesis that ASE is the main mechanism responsible for lasing. However, in very recent studies, presented in chapter 4.2.1, it is observed that the time delay of the lasing pulse is inversely proportional to the number density of interacting atoms. These new results thus suggest that superfluorescence plays a significant role in the mechanisms responsible for lasing. Paper IV presents an application of the backward lasing technique. Spatially-resolved single-shot H-atom distributions were observed with a backward-lasing approach, having the detector located ~2 m away from the measurement region. A highest spatial resolution of 1.6 mm was achieved by temporally resolving the backward directed lasing signal.

Even though the developed backward-lasing technique is capable of delivering valuable qualitative measurements in environments with limited optical access, there is still a desire for quantitative information. Quantification is quite challenging since the signal depends nonlinearly on a number of things, such as the number of excited atoms, laser pump energy and pulse duration. Quantification, thus requires more thorough studies of the lasing generation mechanism and gain dynamics. Results presented in papers II-IV are only about H-atom lasing. Work on detection of oxygen atoms with backward lasing has also been reported in papers related to this project, but not included in the thesis (papers VII and XI). It is of great interest to continue the development of the technique for detection of other species accessible with two-photon pumping, such as nitrogen and chlorine atoms, which are both important species in combustion and atmospheric chemistry. It would also be interesting to investigate backward lasing based on laser filamentation. In fact, such experiments are currently planned in our research group. Another interesting idea on backward lasing is to study what happens if the fs laser pulse is interacting with a levitated liquid droplet, suspended by a standing acoustic wave. This could potentially open up for stand-off detection of bio-aerosols.

Hybrid ns/fs coherent Anti-Stokes Raman scattering

As presented in paper V, a novel CARS concept, namely hybrid femtosecond/nanosecond rotational CARS has been developed and demonstrated. The rotational Raman coherences are excited by broadband fs laser pulses, which, in contrast to previous work based on picosecond excitation [67], allows excitation of the full manifold of Raman coherences on a single-shot basis. The excited Raman coherences are then probed by a nanosecond laser pulse, generating a CARS signal, which is dispersed by a spectrograph and detected by a streak camera, hence resolved simultaneously in both the time and frequency domain. The time-resolved Raman coherences allow measurements of Raman linewidth in-situ in a single-shot acquisition, allowing for single-shot thermometry based on simultaneously measured Raman linewidths, instead of relying on simulated linewidths or crude assumptions in cases when the chemical composition is not known or linewidth models are lacking. In addition to measurements in pure N_2, the versatility of the technique was also demonstrated through measurements in ambient air. At high fs laser pulse energies, Stark effect was clearly observable.

An intuitive next step is to apply the technique for thermometry in various gas mixtures. Recent results from rotational CARS thermometry using the hybrid fs/ns scheme are presented in one of the works related to this project, but not included in the thesis (paper X) [63]. In the future, it is of fundamental interest to study the dynamics of the Stark-splitted spectral lines, in experiments where a homogeneous external electric field is applied across the probe volume. Another potential experiment can be ultrafast RCARS thermometry, i.e. generating several RCARS spectra with one probe pulse in a single-shot acquisition (see Fig. 5.2) by using two or more pairs of fs pump/Stokes photons with a separation between the pairs of ~ 300-500 ps. This would allow us to study extremely fast non-repetitive dynamics. Another very interesting possible project would be to test whether a CARS signal can be generated in the backward direction, using a combination of forward-directed laser pulses and a backward lasing pulse. For example, the backward lasing signal generated from a filament could perhaps be used as the Stokes pulse, while forward-propagating laser pulses serve as pump and probe, generating a CARS signal in the backward direction as long as the phase-matching condition is maintained.
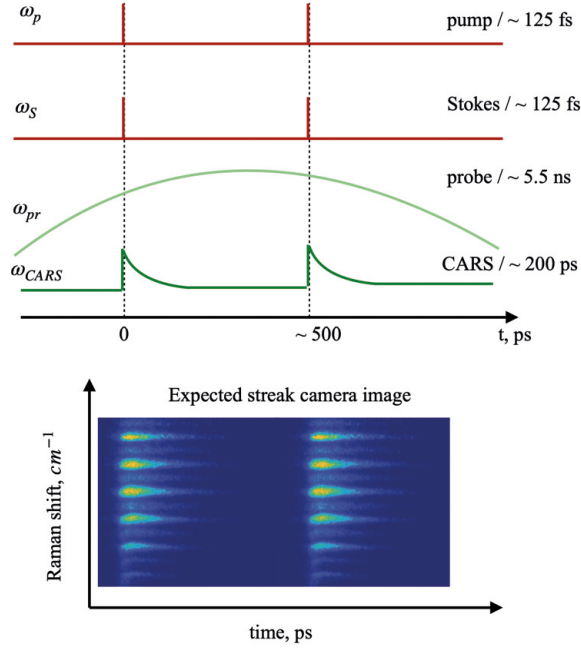
Figure 5.2. Principle of ultrafast RCARS.

Femtosecond laser-induced grating spectroscopy

Femtosecond laser-induced grating spectroscopy, presented in paper VI, allows studies of the thermodynamic properties of a gaseous medium. The concept was investigated in a heated N_2 gas flow with varying temperatures. The grating was formed by crossing two 800-nm wavelength laser pulses. The oscillation frequency of the generated acoustic wave, detected in a single-shot acquisition, is directly linked to the gas temperature. The results show that the method works very well for thermometry in nitrogen. It was found that the temperature measurement uncertainty increases from 1 K up to 90 K for temperatures ranging from 295 K to 750 K respectively. This is due to the fact that with increased temperature the thermal diffusion happens faster, meaning that less oscillation peaks in the thermal LIGS signal can be observed. Furthermore, it was discovered that increasing the laser pulse energies above the ionization threshold substantially changes the shape of the LIGS signal and results in the generation of a plasma grating.

The demonstrated fs-LIGS technique opens the door to a multitude of fundamental molecular studies as well as applications in turbulent reactive flows and high-pressure combustion processes. It would be interesting to investigate the applicability of the technique at elevated pressures as well as for pressures below 1 atm. The results, presented in paper VI, were obtained under quite favourable conditions with high concentration of N_2 in the measurement volume, which obviously was beneficial for driving an efficient 8-photon excitation. However, at flame temperatures ($\sim$ 2000 K), it might be necessary to use a more efficient excitation pathway, e.g. two-photon excitation, which is feasible with the present fs-laser system, since it provides tuneable radiation in the UV regime. Hence, such measurement conditions should be tested in future work.

Appendix A. Laser system.

Ultra-short laser pulses are exceptional and they possess a number of exciting features, which are very useful in modern laser diagnostic techniques. More than twenty years of continuous development and progress following the first laser working in the picosecond regime led to the realization of the first laser able to produce intense light pulses with duration on the femtosecond time scale [90]. This major advance required that researchers needed to find a solution to problems associated with going from pico- to femtosecond regime, namely the damage threshold of optical components of the laser, self-focusing and other non-linear effects that can change the characteristics of the laser pulse. Donna Strickland and Gérard Mourou removed these obstacles by using a technique called chirped pulse amplification (CPA) [91]. Periodic trains of ultra-short pulses, generated by a mode-locked laser are stretched, then amplified, and finally compressed back to their original pulse duration. In this way, the energy may be increased from nano-Joule to milli-Joule per pulse.

In this chapter the femtosecond laser system used in the present thesis work is described in detail. The "heart" of the laser system is a Ti:Sapphire laser, producing intense 125-fs laser pulses at 10 Hz repetition rate using CPA technique. This chapter will provide a guidance for somebody working with the similar laser system.

Femtosecond laser

A schematic overview of the whole laser system is shown in Fig. A.1. The laser system was installed in our laboratory in 2015 and I was the first PhD student to work with it.

The left-hand side of the system, shown in Fig. A.1a, corresponds to units involved in the generation of 125-fs laser pulses of 800-nm wavelength, and consists of two lasers and an amplifier. The first one, to the left, is a pump laser, providing nanosecond pulses at 10 Hz pulse repetition rate. This laser is an Nd:YAG laser (Innolas, SpitLight 600), generating pulses of 532 nm laser wavelength and 245 mJ energy per pulse. The second laser serves the role of oscillator, or seed laser. This mode-locked Ti.Sapphire laser (Coherent, Vitesse) produces sub-100 fs pulses of 800 nm wavelength with 80 MHz repetition rate and 250 mW average power.

The core of the fs-laser system is an amplifier (Coherent, Hidra). The amplifier has two amplification stages: a regenerative amplifier and a multi-pass amplifier. The Hidra also comprises a grating stretcher, internal and external compressor.
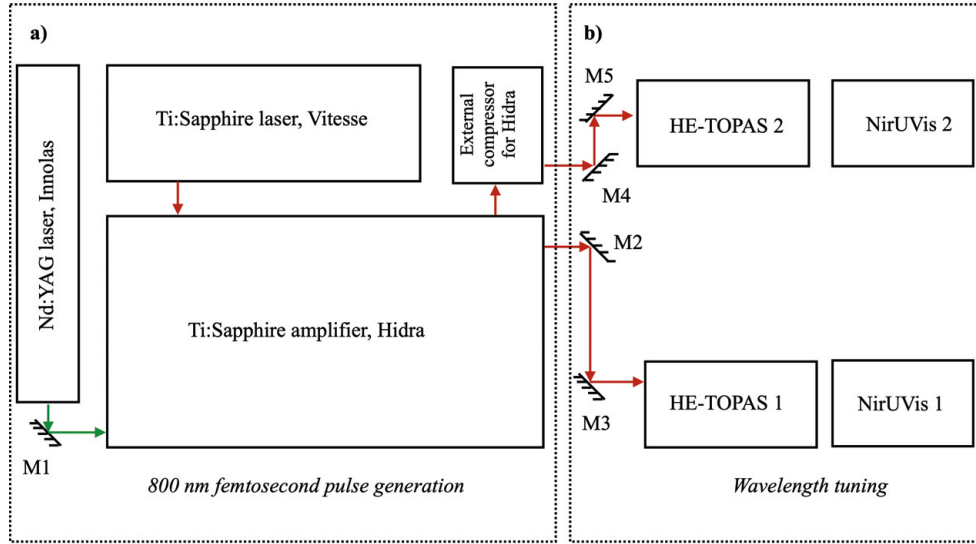

Figure A.1. Schematic overview of the femtosecond laser system. a) Part of the system where 125-fs laser pulses of 800 nm wavelength are generated. b) Part of the system used for wavelength tuning in the range from 190 to 1600 nm. M1-5 designate mirrors.

The right-hand side of the system, shown in Fig. A.1b, consists of two identical high energy traveling-wave optical parametric amplifiers (HE-TOPAS, Light Conversion) and frequency mixing units, NirUVis (frequency mixing stages assembled in monolithic housing). The tuning range of HE-TOPAS is from 190 to 1600 nm. The UV wavelengths used in the current project are generated by second harmonic and sum frequency generation in the NirUVis unit. Detailed processes inside HE-TOPAS and NirUVis are introduced later in the appendix.

Nd:YAG laser

The laser rods in the oscillator and amplifier are pumped by a flash lamp. High-energy nanosecond laser pulses are achieved through Q-switching. The Q-switch is based on a Pockels cell, which contains a KD*P (potassium dideuterium phosphate) crystal, and a polariser. The polariser is a plate mounted at Brewster angle, positioned between a quarter-wave plate and the oscillator rod (neodymium-doped yttrium aluminium garnet, Nd:YAG) inside the resonator [92]. With a static voltage

applied to the crystal the Q-factor is kept low, meaning that the resonator is blocked and a large population inversion is created in the pumped laser rod. When the voltage is abruptly lowered, the Q-factor is rapidly increased, resulting in a short and intense laser pulse. The voltage is controlled by the 5kV electronics trigger box, it also controls the shutter interlock of the laser.

The amplification chamber of the laser is based on another Nd:YAG rod, pumped by the same flash lamp, which amplifies the 1064-nm pulse from the resonator. Optimum temperature condition for the rods and the flash lamp is provided by a flow of deionized water.

A combination of mirrors inside the laser provides multiple amplification and the curvature of the resonator mirrors ensures a stable single-mode collimated output.

The second-harmonic radiation at 532 nm wavelength is achieved by a nonlinear LBO (lithium triborate) crystal. The crystal is placed inside a temperature-controlled chamber. With a small screw on the top of the crystal chamber it is possible to manually vary the angle orientation of the crystal to optimize phase-matching and output energy.

The 532-nm output beam, with a smooth Gaussian profile, is then sent to pump the two Ti:Sapphire crystals in the fs-amplifier, i.e. the Hidra. For most of the experiments the Nd:YAG laser was internally triggered. The output energy was kept around 245 mJ. If the output of the Hidra was not high enough, it was possible to boost it up by increasing the voltage applied to the flash lamp.

Ti:Sapphire laser, Vitesse

The Ti:Sapphire laser (Vitesse) is compact, and it produces seed pulses for the Ti:Sapphire amplifier (Hidra). A schematic overview is shown in Fig. A.2. The system includes a power supply, Verdi laser head and a Verdi-pumped ultra-fast (VPUF) laser head as a cavity for producing the seed beam.

Light transmitted through an optical fiber from a laser diode module, located inside the power supply, is used to pump the Verdi laser head. The major optical elements of the Verdi laser head are two crystals: a Nd:YVO$_4$ (neodymium-doped yttrium orthovanadate) crystal providing the gain medium and an LBO crystal, used for frequency- doubling. Nd:YVO$_4$ gives a strong emission centered at 1064 nm, which is collinear with the second harmonic wavelength at 532 nm generated at the LBO crystal. The continuous wave output laser beam at 532 nm from the Verdi is then directed into the VPUF laser head cavity, where it pumps a Ti:Sapphire crystal (Ti^{3+}:Al$_2$O$_3$) positioned inside a cavity. Kerr-lens mode-locking together with negative dispersion mirrors (NDM), compensating for dispersion, provide sub-100 fs laser pulses [93]. The size of the beam is kept small and controlled by

a slit so that only the high intensity mode-locked pulses will pass through, while the low-intensity continuous wave beam will be cropped at the edges [94].
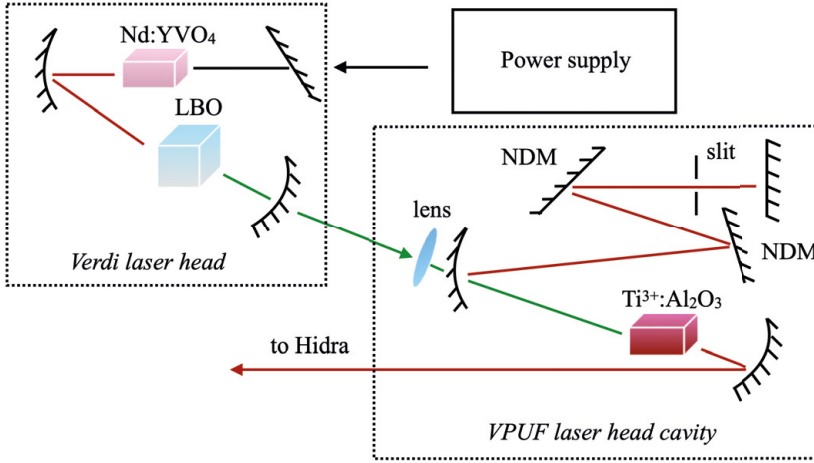

Figure A.2. Generic schematic overview of a Vitesse diode-pumped, modelocked Ti:Sapphire laser, for the actual cavity design refer to [94]. NDM – negative dispersion mirrors.

Kerr effect implies that the amplifying medium in the laser is nonlinear and its refractive index is a function of intensity: $n = n_0 + n_2 I$, where n_2 is the nonlinear refractive index. If $n_2 > 0$, the amplifying medium behaves like a converging lens and focuses the beam along its direction of propagation [95]. This phenomenon is also known as self-focusing. Since the laser intensity is time-dependent, $I(t)$, the refractive index is also changing as a function of time, which leads to self-modulation. The spectrum gets broader and therefore the pulse duration gets shorter. As the pulse is travelling inside the cavity and passes through the crystal it undergoes group velocity dispersion (GDV), which tends to chirp the pulse. This chirping is compensated by the NDMs, which provide negative total dispersion [94].

The resulting ultrashort laser pulses are directed into the Ti:Sapphire laser amplifier system, Hidra.

Ti:Sapphire laser amplifier system

The Ti:Sapphire laser amplifier has three stages: pulse stretching, amplification, and a pulse compression. The basic CPA procedure is described in Fig. A.3 below. A short pulse is stretched in time by a grating and a curved mirror to reduce the peak power, then amplified in an amplifier, and finally recompressed to its original duration using a compressor.
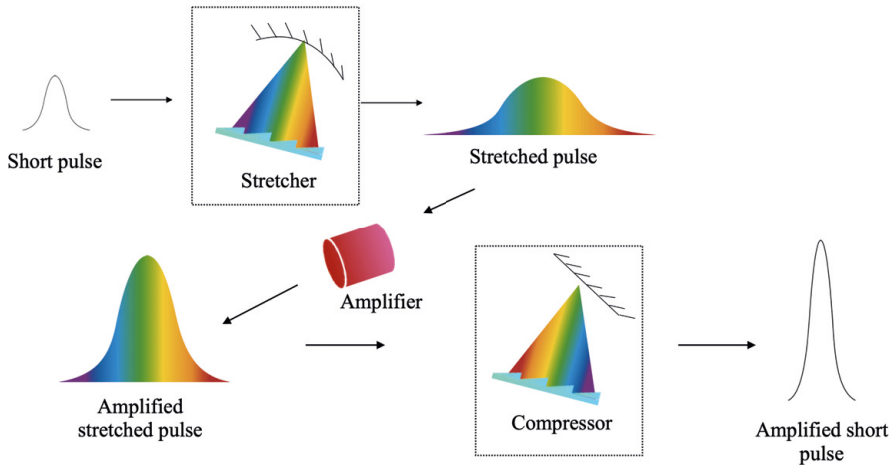

Figure A.3. Overview of the basic principle of CPA. The descriptions of the pulse compressor and pulse strecher are schematic in this figure and thus somewhat simplified.

Pulse stretching

At the further amplification stage, it is critical to keep the peak power of the laser pulse at a level low enough that non-linear effects do not affect the temporal and spatial profile of the pulse. For this purpose, the laser pulses (few nanojoules of 800 nm wavelength) coming from the Vitesse laser are stretched before amplification. The Hidra pulse stretcher consists of a grating, a retro-reflector, and a large curved mirror. After going through a Faraday isolator, the input pulse hits the grating, which spatially disperses the optical frequency spectrum of the pulse so that the low-frequency (red) components travel ahead of the high-frequency (blue) components. The pulse is now stretched in time by being "positively chirped". The mirror and the retro-reflector work in pair in order to place the beam correctly on the grating. A double-pass through the system is required in order to ensure that the spatial profile of the beam is reconstructed. The vertical displacement of the beam is showed in Fig. A.4. Now the stretched pulse is ready to enter the amplification stage.
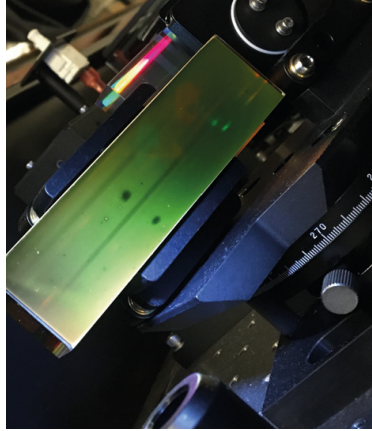
Figure A.4. Photo of the stretcher grating. A short pulse beam (the lowerest circle) and a spatially reconstructed beam as we see at the stretcher grating with their spectrally dispersed representation (showed as lines). A vertical retro-reflector moves the spatially extended beam slightly upwards.

Pulse amplification

Three years after publishing the ground-breaking paper on CPA the same authors presented three major requirements on the amplification medium. Firstly, the bandwidth of the amplifier medium must be large enough to assist the full spectrum of the short pulse [96]. The second requirement is that the laser intensity of the short pulse should be near the saturation level of the amplifier medium. Finally, the peak intensity within the amplifier has to stay below a critical level to avoid generating unwanted nonlinear effects [90]. These requirements made Ti:Sapphire an attractive amplifier medium.

In a Ti:Sapphire crystal ($Ti^{3+}:Al_2O_3$), Ti^{3+} ions replace Al^{3+} ions in an Al_2O_3 crystal. The energy level diagram of Ti^{3+} ions in Al_2O_3 has four levels [96]. Coupling of the electronic energy levels of the Ti^{3+} ions with vibrational energy levels of the surrounding sapphire lattice is important for $Ti^{3+}:Al_2O_3$ to operate properly as an active laser medium. The process is complicated and very well described in a paper by Walla and Sanchez [97]. The energy level structure of $Ti^{3+}:Al_2O_3$ allows efficient pumping with light in the visible wavelength range (400-600 nm), resulting in emission ranging from roughly 600 to 1000 nm, peaking at 790 nm. In our case, the pumping wavelength is 532 nm. In the current laser system, only a small portion of the Ti: Sapphire crystal rod is pumped. It is done in order to homogeneously distribute the heat produced in the pumping region over the whole crystal to avoid overheating and too large output power. The crystal is, as well, cut at the Brewster's angle to minimize losses due to reflection [97]. Additional cooling to the crystal is provided by a flow of deionized water.

The design of the amplifier was customized for the research requirements of the Combustion Physics femtosecond laboratory and is schematically shown in Fig. A.5.
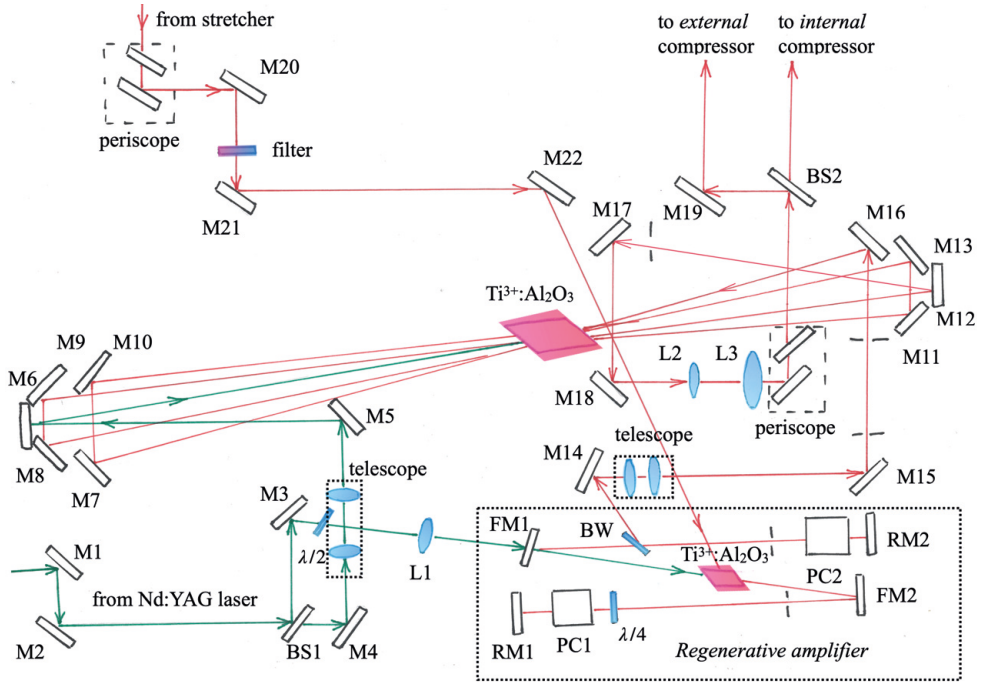

Figure A.5 Optical components and beam paths inside the Ti:Sapphire amplifier, Hidra. M1-21 mirrors; BS1,2 beam splitters; PC1,2 Pockells cells; RM1,2 resonator mirrors; FM1,2 folding mirrors; BW- Brewster window.

In the Hidra amplification system multi-pass linear amplifiers are used. These amplifiers rely on multiple passages through a medium, Ti:Sapphire, that has been pumped into population inversion in order to exhibit stimulated emission. Two multi-pass amplification configurations are present in the system.

The first configuration is called a regenerative amplifier, and is shown in the lower right corner of Fig. A.5. This configuration resembles a resonator since the active medium (a Ti:Sapphire rod) is placed between two resonator mirrors RM1 and RM2. The seed 800 nm pulse, which is coming from the stretcher, is injected into the cavity by mirror M22. In the beginning the Pockels cell PC1 is deactivated and the pulse is not amplified, it is just travelling one roundtrip in the amplifier and then leaves through reflection at the Brewster window (BW). A fraction of the green 532 nm pump pulse coming from the Nd:YAG laser is focused onto the $Ti^{3+}:Al_2O_3$ rod by lens L1 to optically pump it, at this time Pockels cell PC1 is activated, and

allows a single seed pulse to be captured, circulate, and get amplified inside the cavity. After a number of round trips, a voltage change is abruptly applied to the second Pockels cell PC2, changing the polarization of the pulse, which then is ejected from the cavity at BW [98]. Now the amplified laser pulse is on its way to the second multi-pass amplification stage.

The timing and switching of the Pockels cells require precise and fast electronics. A synchronization and delay generator (SDG) provides precise timing required for the Pockels cells in the regenerative amplification stage [98]. It also synchronizes three systems: Innolas, Vitesse and Hidra, and provides output trigger pulses. Delay knobs on the SDG control the two Pockels cells (PC1 and PC2) separately, and it is hence possible to manually change the number of roundtrips in the regenerative amplifier cavity by changing the delay for PC2. In this way the laser output power can be varied. A limiting factor for the maximum laser output might be gain narrowing, which the system experiences with a significant amount of amplification roundtrips. The consequence of this is that the wavelengths in the central part of the envelope experience more amplification compared to the wings. Synchronization and delay generator also has an option of changing the delays for both PC1 and PC2 an equal amount at the same time, i.e. keeping the difference between the PC1 delay and the PC2 delay the same. This option is called "universal delay". In the CARS experiments we used this option to optimize synchronization between the fs-laser and other devices in the setup, such as another Nd:YAG laser and a streak camera. The drawback of using a too large "universal delay" is reduced laser output energy and reduced bandwidth of the pulse. The reason for the lower output energy is mainly that the single-pass gain (in regenerative amplifier) of the Ti:Sapphire crystal is lower after a too long "universal delay".

In the second amplification stage, the so-called multi-pass amplifier, the pulse passes through the amplification medium several times. The remaining fraction of the green 532 nm pump pulse, i.e. the light transmitted through BS1, is via reflection on mirror M5 directed onto the Ti:Sapphire rod, as can be seen in Fig. A.5. This geometry requires very precise alignment, since the distance from mirrors on one end to mirrors on the other end is approximately one meter. Any potential thermal or mechanical fluctuations might hence cause misalignment.

Finally, the amplified pulse reflects from M12 and goes to the large lens L3 before the periscope, and at this stage the laser pulse energy reaches around 80 mJ. After the periscope the beam is divided by the beam splitter BS2, sending beams, each with about half the incident pulse energy, to an internal compressor and an external compressor, respectively.

Pulse compression

The Hidra has two identical compressors, one internal and one external, which consist of a grating, two retro-reflectors, and mirrors for alignment, see the sketch of the external compressor in Fig. A.6. The principle is opposite to pulse stretching. Now the grating is configured in a way that the high-frequency components (blue) travel a shorter path compared to the low-frequency components (red). In this way the pulse recovers its original phase and amplitude. The initial bandwidth is recovered as well. The retro-reflectors are displacing the beam in the horizontal and vertical direction on the grating. It is important to obtain double-passing throughout the grating to achieve a circular beam profile at the exit. Properly aligned, the output pulse is Fourier transform limited and obeys the relation between the laser pulse duration τ_l (at FWHM) and the spectral bandwidth $\Delta\nu$ for a Gaussian pulse [98]:

$$\Delta\nu \cdot \tau_l > 0.441$$

Due to unstable conditions in the lab, the pulse may experience changes, such as becoming slightly chirped (increasing the pulse duration). This issue can sometimes be mitigated by slightly adjusting retro-reflector 2.
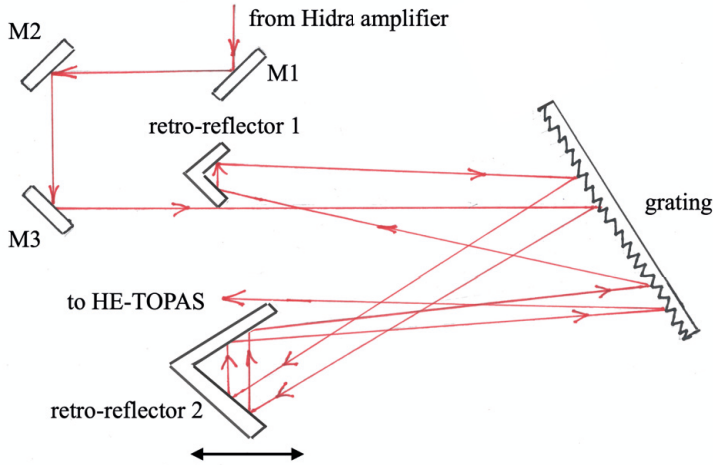

Figure A.6. Sketch of optical components in the external compressor of the Hidra. Retro-reflector 2 can be moved in the horizontal direction to ensure the best compression of the pulse.

HE-TOPAS

The pump pulse coming from the internal compressor is now directed by the mirrors M2 and M3 (see Fig. A.1) into the optical parametric amplifier HE-TOPAS 1. Similarly, the pulse coming from the external compressor is directed by mirrors M4 and M5 into HE-TOPAS 2.

Optical parametric amplification is a non-linear optical amplification process, in which a strong signal and idler beam are created by sending a weak signal beam into a nonlinear crystal while pumping it with an intense pump beam. The HE-TOPAS is slightly different from the commonly used OPA, as it utilizes a white light continuum (WLC) for a three-stage parametric amplification in nonlinear crystals.

The basic configuration of the HE-TOPAS consists of several stages: pump beam delivery (HE-PO), seed generator of high-power amplification stage (HE-SG), seed expander-collimator for high power stage (HE-EC), and high-power amplification stage (HE-PA), as schematically illustrated in Fig. A.7.
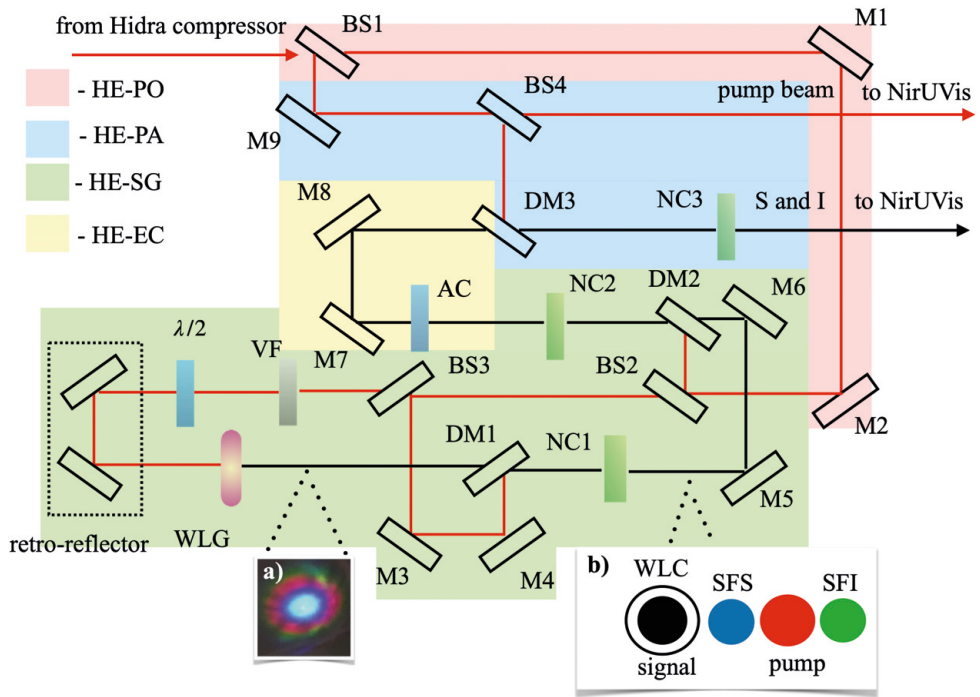
Figure A.7. A simplified sketch of optical components and beam paths in the HE-TOPAS [99]. a) A photograph of WLC observed on a paper. b) Arrangement of the output beams after NC1.

At the first stage (HE-PO), a horizontally polarized 800 nm pump beam is coming from the Hidra compressor. It is not recommended to deliver more than 30 mJ of the pump energy to the HE-TOPAS. Hence, the pump pulse energy was kept below this value for all experiments. About 90 % of the pump pulse energy is reflected by the beam-splitter BS1 into the HE-PA stage, and around 300 µJ of pulse energy is transmitted to pump the HE-SG stage. In this stage, another beam splitter, BS2, reflects around 80% of the beam energy to go to the second amplification stage, while around 30µJ is transmitted to generate a WLC in a Sapphire plate (labelled WLG, which stands for white-light generation, in Fig. A.7).

It is worth mentioning that before the WLC generation stage, a fraction of the pump beam is reflected by a third beam splitter, BS3, to pump a pre-amplification stage. The white light continuum generation stage uses a variable density filter, VF, to adjust the pump beam intensity. The horizontal polarization is rotated by a half-wave plate in order to generate vertically polarized white light. It should be noted that optimal WLC generation requires that the pump pulse is transform-limited, and its intensity should not be too high. If these requirements are fulfilled, the WLC will look similar to the one in Fig. A.7a.

The white light intersects non-collinearly with the pump beam in the first non-linear crystal NC1. As a result of this interaction, a signal beam, a residual pump beam, and an idler beam is generated. Only the IR part (1100-1600 nm) of the WLC is used for the pre-amplification. The signal, or in other words, the amplified WLC, has a wavelength corresponding to the WLC wavelength overlapped with the pump pulse. The signal wavelength can be changed by adjusting the delay and the crystal angle for optimum phase-matching. All the procedures for adjusting crystal angles and delays are executed in the software. Figure A.7b schematically illustrates the output beams after the non-linear crystal NC1. The signal lies on top of the WLC, but is still visible to the naked eye, since the observable spot corresponds to the second harmonic of the signal. The spot between the signal and the pump is the sum frequency of the signal (SFS) and the spot to the right of the pump is the sum frequency of the idler (SFI). All the residual spots and the pump are blocked by a beam blocker. Only the signal beam goes to the next stage, where it is collimated before entering the second amplification stage.

The purpose of the second amplification stage is to amplify the signal beam produced in the pre-amplification stage by using a pump beam, reflected by beam splitter BS2. The energy can be increased from around $3\,\mu J$ to tens of µJ. Both signal and pump beam enter the non-linear crystal NC2 collinearly to amplify the signal. The phase-matching angle of the crystal is adjusted in the computer software.

Signal and idler beams received at the previous amplification stage are used as seeds for the high-power amplification stage (HE-EC). The two pulses are separated in time by 1 ps using an anisotropic crystal AC. This birefringent crystal has different refractive index depending on the polarization. Depending on selected

configuration, either the signal or the idler is used as seed for the last high-power amplification stage.

At the final high-power amplification stage (HE-PA), the 800 nm pump beam, previously reflected from beam splitter BS1, is used to amplify the seed beam coming from the HE-EC. Both beams collinearly enter the third non-linear crystal NC3. At the exit of the HE-TOPAS, both a signal (S) and an idler (I) beam is present. The output pulse energy varies depending on the wavelength, reaching a maximum of 7 mJ at around 1500 nm. Similar to the previous stages, the phase matching angle and the delay for the crystal NC3 is adjusted in the software. A beam splitter BS4 reflects 80% of the energy and transmits 20 %. The transmitted part of the 800 nm pump beam is used for sum frequency generation and deep UV (DUV) generation in the NirUvis unit, to be described in the next section.

NirUVis

The NirUVis unit (frequency mixing stages assembled in monolithic housing) extends the wavelength tunability of the HE-TOPAS. It is possible to use frequency doubling (SHG) and sum frequency generation (SFG) to generate wavelengths in the visible, UV and DUV range.

The unit consists of three BBO (barium borate, beta-BaB_2O_4) crystals, which are used for the second-harmonic and sum-frequency generation, and wavelength separators (WS), located between the crystal housings. The main purpose of the wavelength separators is to displace the beam either vertically or horizontally depending on the polarization (s or p) and enhance the contrast of the central wavelength within the range where the WS is used. It is very important to pick the WS corresponding to the correct wavelength range and interaction. The number of wavelength separators used in the NirUVis unit is dependent on the particular interaction processes used to generate the desired wavelength. Maximum three WS can be used.

The output port of the NirUVis has four exists, their position varies vertically and horizontally. The position of the output port can be adjusted depending on the requested wavelength, in this case the other outputs will be blocked.

As an example, the procedure of receiving the most commonly used wavelength in the present experiments, i.e. 205 nm, is described below.

The process is divided into three wavelength mixing stages, as illustrated in Fig. A.8. In the first stage a sum frequency (SF) beam is generated by mixing the residual 800 nm pump beam from the HE-TOPAS output and the HE-TOPAS output signal beam in a crystal. An appropriate wavelength separation module (WS1), having the SF wavelength in the centre of its operational wavelength range,

is used after the mixing. In the second stage, the resulting beam is frequency doubled and another WS (WS2), having a different operational wavelength range, is used. Finally, in the third stage, a 205 nm beam is generated by mixing the 800 nm pump laser beam and the frequency doubled beam generated in the previous stage. A third WS (WS3) is used after the mixing, providing a 205-nm laser pulse of with vertical polarization. The phase-matching angles of the crystals and the delay stage movements for the 800 nm pump beams for correct time overlap are controlled in the software.
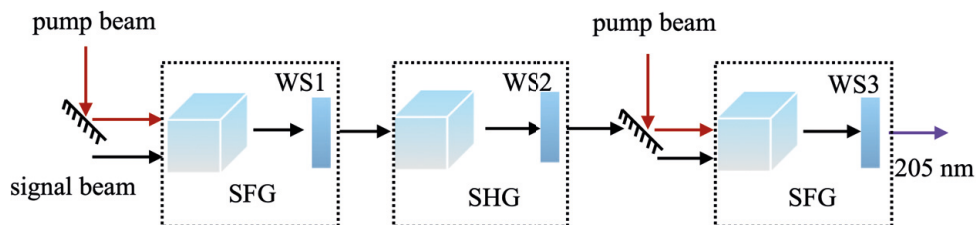
Figure A.8. A simplified sketch of optical components and beam paths when generating 205 nm beam in the NirUVis [100]. SHG – second harmonic generation, SFG – sum frequency generation.

Acknowledgements

Igor Buzuk, thank you for always finding solutions to the problems with my computers. *Mattias Richter,* thank you for the supportive conversations and for giving me a chance to teach, for several years in a row, one and only laboratory exercise "OH PLIF". *Alexander Konnov*, thank you for supporting me at the beginning of my time at the division.

I would like to thank the most positive and versatile research group *Boboodod*: *Kajsa Larsson, Elin Malmquist, Jim Larsson, and Pengji Ding.* I feel like we did all the possible research from fauna to flame and from femtosecond lasers to piglets. Our group meetings were so enjoyable.

Elin, I admire your erudition and ability to contribute to any conversation and thank you for being the first person to introduce me to the basement lab. *Jim,* I think that your project about piglets was the most exciting at the division. Thanks for organising fun movie/pizza evenings at your place. *Kajsa,* thanks for giving me the tableware during my hard times when I didn't have any dishes or furniture in my apartment.

"*Pengji*, you always talk about this physics". My best postdoc, destiny blessed me to work with a pure, kind, smart, and funny person as you are. Most of my PhD studies happened during the work with you and it was a very amusing time.

In the new *Boboodod* group: *Ali Hosseinnia, Meena Raveesh, Armand Dominguez* we all have something in common – ultra-short laser diagnostics. I enjoyed fruitful and sometimes challenging discussions during our group meetings. *Meena and Armand,* you are at the beginning of your journey and I can foresee how many amazing discoveries you will make. Enjoy the ride and don't forget to enjoy your life as well. *Ali*, thank you for introducing me to CARS and taking professional pictures of me being a scientist. I liked our serious (maybe not) chats about everything and nothing. *Guys*, I wish I could have worked more with you in the lab.

I would also like to thank my other co-workers: *Dina Hot, Anna-Lena Sahlberg, Davide Del Cont-Bernard, Andreas Ehn, Zhongshan Li, Per-Erik Bengtsson and Christian Brackmann* for a good collaboration, for your professionalism and dedication.

Dina, you are a very caring person, thank you for your help and support. I still think sometimes that I would hear your voice in the corridor: "Hi Maria! How are you?"… *Anna-Lena*, thank you for sharing your knowledge about LIGS with me. *Christian,* thank you for always finding a time for the discussions with me about LIF (and not only), for being open and willing to help.

Andreas, when I first came to the division and took the "Laser-based combustion diagnostics" course with you as a supervisor I thought that you are a serious person …well; please take care of the parrot when I'm not here. Thank you for that mini chocolate/s from the box, it was delicious. *Edouard Berrocal*, thank you for having interesting (sometimes silly) discussions with me during the late working hours and

… for the unforgettable parties. I admire your dedication to the research and amazing ways of presenting it.

My wonderful friend *Yupan*, I can be that crazy only because you are by my side, can't wait to have more adventures with you.

Giota, my dear officemate, thank you for giving me a chance of using the office and your table all for myself…but it feels lonely here without you.

I would like to thank the extraordinary gang, my great friends: *Marco, Manu, Haisol,* and *Saeed* for all the adventures we had and for reminding me that there is a lot of fun and joy outside the work.

I would like to thank the wonderful people and colleagues

Sven-Inge Möller, Mikkel Brydegaard, Frederik Ossler, Johan Zetterberg, Elias Kristensson, Elna Heimdal Nilssson, Sandra Török, Alexios Matamis, Liza Rämish, Arman Subash, Karolina Dorozynska, Xin Lui, Christian Binder, Ludovica Luise, Christoffer Pichler, Gianluca Capriolo, Adrian Roth, Sebastian Pfaff, Kailun Zhang, Vladimir Alekseev, Sebastian Nilsson, David Sanned, Meng Li, Vassily Kornienko, Jonas Ravelid, Hampus Månefjord, Sabrina Gericke, Saga Bergqvist, Jundie Chen, Zhiyong Wu, Yue Qui, Qingshuang Fan, Shen Li, Henrik Feuk, David Frantz, David Andersson, Ruike Bi, Thi Kim Cuong Le, Jacobo Salvador, Mehdi Stiti, Wubin Weng, Torsten Methling, Moah Christensen, Zhenkan Wang, Jinlong Gao and Fahed Abou Nada

and the others for providing me help and support in variable ways, either having a conversation with me, lending equipment to me, or making me smile. You all filled up my time here with joy, laughter, and excitement. To some of you I should express a special gratitude but in this case this acknowledgement will never end.

Dasha, the person, who has been by my side since the very first day when I stepped my foot on the platform at Lund C. I'm glad that we share a passion for Massimo Dutti and Aperol Spritz. Thank you for your massive support and endless friendship.

Robert, you are probably sleeping right now and we will see each other only in a few days but thank you very much for your patience, love, encouragement, and enormous support during this journey.

Warm gratitude to my *Mother,* who has sacrificed a lot to give me a good education and taught me a life decisions analysis. *Мама,* спасибо за веру в меня, любовь и душевую поддержку!

References

1. *They found hidden patterns in the climate and in other complex phenomena*, in *The Nobel prize in Physics 2021, popular science background* S. Gustavsson, Editor. 2021, The Royal Swedish Academy of Sciences.
2. NOAA *State of the Climate: Global Climate Report for Annual 2020*. 2021.
3. *Sustainable development*. Department of economics and social affairs, sustainable development, the 17 goals; Available from: https://sdgs.un.org/goals.
4. *Adoption of the Paris Agreement*. 2015, United Nations.
5. Eckbreth, A.C., *Laser diagnostics for combustion temperature and species*. 1996: Gordon and Breach Publishers SA.
6. Boyd, R.W., *Chapter 1 - The Nonlinear Optical Susceptibility*, in *Nonlinear Optics (Third Edition)*, R.W. Boyd, Editor. 2008, Academic Press: Burlington. p. 1-67.
7. Ruchkina, M., et al., *Two-photon-excited fluorescence of CO: experiments and modeling.* Optics Express, 2019. **27**(18): p. 25656-25669.
8. Kohse-Höinghaus, K., *Laser techniques for the quantitative detection of reactive intermediates in combustion systems.* Progress in Energy and Combustion Science, 1994. **20**(3): p. 203-279.
9. Crosley, D. and G. Smith, *Laser-Induced Fluorescence Spectroscopy For Combustion Diagnostics.* Optical Engineering, 1983. **22**(5): p. 225545.
10. Aldén, M., et al., *Two-photon excitation of atomic oxygen in a flame.* Optics Communications, 1982. **42**(4): p. 244-246.
11. Aldén, M., et al., *Single-pulse laser-induced OH fluorescence in an atmospheric flame, spatially resolved with a diode array detector.* Applied Optics, 1982. **21**(7): p. 1236-1240.
12. Aldén, M., et al., *Imaging laser-induced fluorescence of oxygen atoms in a flame.* Applied Optics, 1984. **23**(19): p. 3255-3257.

13. Aldén, M., et al., *Three-photon-excited fluorescence detection of atomic hydrogen in an atmospheric-pressure flame.* Optics Letters, 1984. **9**(6): p. 211-213.

14. Jonsson, M., et al., *Simultaneous one-dimensional fluorescence lifetime measurements of OH and CO in premixed flames.* Applied Physics B, 2014. **115**(1): p. 35-43.

15. Bradshaw, J. and D.D. Davis, *Sequential two-photon-laser-induced fluorescence: a new method for detecting atmospheric trace levels of NO.* Optics Letters, 1982. **7**(5): p. 224-226.

16. Kulatilaka, W.D., et al., *Photolytic-interference-free, femtosecond, two-photon laser-induced fluorescence imaging of atomic oxygen in flames.* Applied Physics B, 2016. **122**(2): p. 26.

17. Frank, J.H., et al., *Comparison of nanosecond and picosecond excitation for two-photon laser-induced fluorescence imaging of atomic oxygen in flames.* Applied Optics, 2004. **43**(12): p. 2588-2597.

18. Goldsmith, J.E.M., *Photochemical effects in two-photon-excited fluorescence detection of atomic oxygen in flames.* Applied Optics, 1987. **26**(17): p. 3566-3572.

19. Goldsmith, J.E.M., *Two-step saturated fluorescence detection of atomic hydrogen in flames.* Optics Letters, 1985. **10**(3): p. 116-118.

20. Kulatilaka, W.D., et al., *Comparison of nanosecond and picosecond excitation for interference-free two-photon laser-induced fluorescence detection of atomic hydrogen in flames.* Applied Optics, 2008. **47**(26): p. 4672-4683.

21. Kulatilaka, W.D., et al., *Analysis of 205-nm photolytic production of atomic hydrogen in methane flames.* Applied Physics B, 2009. **97**(1): p. 227-242.

22. Kulatilaka, W.D., et al., *Photolytic-interference-free, femtosecond two-photon fluorescence imaging of atomic hydrogen.* Optics Letters, 2012. **37**(15): p. 3051-3053.

23. Kulatilaka, W.D., J.R. Gord, and S. Roy, *Femtosecond two-photon LIF imaging of atomic species using a frequency-quadrupled Ti:sapphire laser.* Applied Physics B, 2014. **116**(1): p. 7-13.

24. Goldsmith, J.E.M., *Photochemical effects in 205-nm, two-photon-excited fluorescence detection of atomic hydrogen in flames.* Optics Letters, 1986. **11**(7): p. 416-418.

25.   Brackmann, C., et al., *Picosecond excitation for reduction of photolytic effects in two-photon laser-induced fluorescence of CO.* Proceedings of the Combustion Institute, 2013. **34**(2): p. 3541-3548.

26.   Richardson, D.R., S. Roy, and J.R. Gord, *Femtosecond, two-photon, planar laser-induced fluorescence of carbon monoxide in flames.* Optics Letters, 2017. **42**(4): p. 875-878.

27.   Stauffer, H.U., et al., *Laser-induced fluorescence detection of hydroxyl (OH) radical by femtosecond excitation.* Optics Letters, 2011. **36**(10): p. 1776-1778.

28.   Bradshaw, J.D., M.O. Rodgers, and D.D. Davis, *Sequential two-photon laser-induced fluorescence: a new technique for detecting hydroxyl radicals.* Applied Optics, 1984. **23**(13): p. 2134-2145.

29.   Wang, Y., C. Capps, and W.D. Kulatilaka, *Femtosecond two-photon laser-induced fluorescence of krypton for high-speed flow imaging.* Optics Letters, 2017. **42**(4): p. 711-714.

30.   Li, B., et al., *Strategy of interference-free atomic hydrogen detection in flames using femtosecond multi-photon laser-induced fluorescence.* International Journal of Hydrogen Energy, 2017. **42**(6): p. 3876-3880.

31.   Yao, J., et al., *High-brightness switchable multiwavelength remote laser in air.* Physical Review A, 2011. **84**(5): p. 051802.

32.   Hemmer, P.R., et al., *Standoff spectroscopy via remote generation of a backward-propagating laser beam.* Proceedings of the National Academy of Sciences, 2011. **108**(8): p. 3130.

33.   Sprangle, P., et al., *Remotely induced atmospheric lasing.* Applied Physics Letters, 2011. **98**(21): p. 211102.

34.   Liu, Y., et al., *Self-seeded lasing in ionized air pumped by 800 nm femtosecond laser pulses.* Optics Express, 2013. **21**(19): p. 22791-22798.

35.   Mysyrowicz, A., et al., *Lasing without population inversion in N2+.* APL Photonics, 2019. **4**(11): p. 110807.

36.   Zhang, X., et al., *Backward lasing of singly ionized nitrogen ions pumped by femtosecond laser pulses.* Applied Physics B, 2020. **126**(3): p. 53.

37.   Dogariu, A., et al., *High-Gain Backward Lasing in Air.* Science, 2011. **331**(6016): p. 442-445.

38.   Traverso, A.J., et al., *Coherence brightened laser source for atmospheric remote sensing.* Proceedings of the National Academy of Sciences, 2012. **109**(38): p. 15185.

39.   Laurain, A., M. Scheller, and P. Polynkin, *Low-Threshold Bidirectional Air Lasing.* Physical Review Letters, 2014. **113**(25): p. 253901.

40.   Ding, P., et al., *Lasing dynamics of neutral nitrogen molecules in femtosecond filaments.* Physical Review A, 2016. **94**(4): p. 043824.

41.   Couairon, A. and A. Mysyrowicz, *Femtosecond filamentation in transparent media.* Physics Reports, 2007. **441**(2): p. 47-189.

42.   Rothenberg, J.E., *Space–time focusing: breakdown of the slowly varying envelope approximation in the self-focusing of femtosecond pulses.* Optics Letters, 1992. **17**(19): p. 1340-1342.

43.   Goldsmith, J.E.M., *Two-photon-excited stimulated emission from atomic hydrogen in flames.* Journal of the Optical Society of America B, 1989. **6**(11): p. 1979-1985.

44.   Westblom, U., P.E. Bengtsson, and M. Aldén, *Carbon atom fluorescence and C2 emission detected in fuel-rich flames using a UV laser.* Applied Physics B, 1991. **52**(6): p. 371-375.

45.   Westblom, U., et al., *Properties of laser-induced stimulated emission for diagnostic purposes.* Applied Physics B, 1990. **50**(6): p. 487-497.

46.   Ruchkina, M., et al., *Single-shot, spatially-resolved stand-off detection of atomic hydrogen via backward lasing in flames.* Proceedings of the Combustion Institute, 2019. **37**(2): p. 1281-1288.

47.   Ding, P., et al., *Femtosecond two-photon-excited backward lasing of atomic hydrogen in a flame.* Optics Letters, 2018. **43**(5): p. 1183-1186.

48.   Ding, P., et al., *Gain mechanism of femtosecond two-photon-excited lasing effect in atomic hydrogen.* Optics Letters, 2019. **44**(9): p. 2374-2377.

49.   Gross, M. and S. Haroche, *Superradiance: An essay on the theory of collective spontaneous emission.* Physics Reports, 1982. **93**(5): p. 301-396.

50.   Dicke, R.H., *Coherence in Spontaneous Radiation Processes.* Physical Review, 1954. **93**(1): p. 99-110.

51.   Bonifacio, R. and L.A. Lugiato, *Cooperative radiation processes in two-level systems: Superfluorescence.* Physical Review A, 1975. **11**(5): p. 1507-1521.

52.   Polynkin, P. and Y. Cheng, *Air Lasing.* 2018: Springer International Publishing.

53. Ding, P., et al., *Femtosecond laser-induced quantum-beat superfluorescence of atomic oxygen in a flame.* Physical Review A, 2021. **104**(3): p. 033517.

54. Yuan, L., et al., *Theoretical analysis of the coherence-brightened laser in air.* Physical Review A, 2013. **87**(2): p. 023826.

55. Raman, C.V., *A new radiation.* Indian Journal of Physics, 1928. **2**: p. 387-398.

56. Svanberg, S., *Radiation and Scattering Processes*, in *Atomic and Molecular Spectroscopy: Basic Aspects and Practical Applications*, S. Svanberg, Editor. 2004, Springer Berlin Heidelberg: Berlin, Heidelberg. p. 41-70.

57. W.Boyd, R., *Nonlinear optics*. 2008: Academic Press.

58. Shen, Y.R., *The principles of nonlinear optics*. 1984, New York: John Wiley & Sons. 576.

59. Barrett, J.J., *Generation of coherent anti-Stokes rotational Raman radiation in hydrogen gas.* Applied Physics Letters, 1976. **29**(11): p. 722-724.

60. Eckbreth, A.C. and T.J. Anderson, *Simultaneous rotational coherent anti-Stokes Raman spectroscopy and coherent Stokes Raman spectroscopy with arbitrary pump–Stokes spectral separation.* Optics Letters, 1986. **11**(8): p. 496-498.

61. Aldén, M., P.-E. Bengtsson, and H. Edner, *Rotational CARS generation through a multiple four-color interaction.* Applied Optics, 1986. **25**(23): p. 4493-4500.

62. Kulatilaka, W.D., et al., *Direct measurement of rotationally resolved H2 Q-branch Raman coherence lifetimes using time-resolved picosecond coherent anti-Stokes Raman scattering.* Applied Physics Letters, 2010. **97**(8): p. 081112.

63. Hosseinnia, A., et al., *Single-shot fs/ns rotational CARS for temporally and spectrally resolved gas-phase diagnostics.* Proceedings of the Combustion Institute, 2021. **38**(1): p. 1843-1850.

64. Roy, S., T.R. Meyer, and J.R. Gord, *Broadband coherent anti-Stokes Raman scattering spectroscopy of nitrogen using a picosecond modeless dye laser.* Optics Letters, 2005. **30**(23): p. 3222-3224.

65. Kliewer, C.J., et al., *Picosecond time-resolved pure-rotational coherent anti-Stokes Raman spectroscopy in sooting flames.* Proceedings of the Combustion Institute, 2011. **33**(1): p. 831-838.

66. Miller, J.D., et al., *Single-shot gas-phase thermometry using pure-rotational hybrid femtosecond/picosecond coherent anti-Stokes Raman scattering.* Optics Express, 2011. **19**(16): p. 15627-15640.

67. Nordström, E., et al., *Raman linewidth measurements using time-resolved hybrid picosecond/nanosecond rotational CARS.* Optics Letters, 2015. **40**(24): p. 5718-5721.

68. Hosseinnia, A., et al., *Simultaneous temporally and spectrally resolved Raman coherences with single-shot fs/ns rotational CARS.* Optics Letters, 2020. **45**(2): p. 308-311.

69. Farrow, R.L., P.L. Mattern, and L.A. Rahn, *Comparison between CARS and corrected thermocouple temperature measurements in a diffusion flame.* Applied Optics, 1982. **21**(17): p. 3119-3125.

70. Ruchkina, M., et al., *Laser-induced thermal grating spectroscopy based on femtosecond laser multi-photon absorption.* Scientific Reports, 2021. **11**(1): p. 9829.

71. Stampanoni-Panariello, A., B. Hemmerling, and W. Hubschmid, *Temperature measurements in gases using laser-induced electrostrictive gratings.* Applied Physics B, 1998. **67**(1): p. 125-130.

72. Luers, A., et al., *Flame thermometry using laser-induced-grating spectroscopy of nitric oxide.* Applied Physics B, 2018. **124**(3): p. 43.

73. Latzel, H., et al., *Thermal grating and broadband degenerate four-wave mixing spectroscopy of OH in high-pressure flames.* Applied Physics B, 1998. **67**(5): p. 667-673.

74. Cummings, E.B., *Laser-induced thermal acoustics: simple accurate gas measurements.* Optics Letters, 1994. **19**(17): p. 1361-1363.

75. Cummings, E.B., et al., *Measurement of gas-phase sound speed and thermal diffusivity over a broad pressure range using laser-induced thermal acoustics.* Optics Letters, 1995. **20**(14): p. 1577-1579.

76. Eichler, H., G. Salje, and H. Stahl, *Thermal diffusion measurements using spatially periodic temperature distributions induced by laser light.* Journal of Applied Physics, 1973. **44**(12): p. 5383-5388.

77. Kiefer, J., et al., *Local fuel concentration measurements for mixture formation diagnostics using diffraction by laser-induced gratings in comparison to spontaneous Raman scattering.* Journal of Raman Spectroscopy, 2008. **39**(6): p. 711-721.

78. Stampanoni-Panariello, A., et al., *Gas phase diagnostics by laser-induced gratings I. theory.* Applied Physics B, 2005. **81**(1): p. 101-111.

79. Edwards, M., A. Dogariu, and R. Miles, *Simultaneous Temperature and Velocity Measurement in Unseeded Air Flows with FLEET*, in *51st AIAA Aerospace Sciences Meeting including the New Horizons Forum and Aerospace Exposition*. 2013, American Institute of Aeronautics and Astronautics.

80. Hemmerling, B. and D.N. Kozlov, *Collisional relaxation of singlet $O_2(b1\Sigma+g)$ in neat gas investigated by laser-induced grating technique.* Chemical Physics, 2003. **291**(3): p. 213-242.

81. Kozlov, D.N., et al., *Determination of Physicochemical Parameters of Ionic Liquids and Their Mixtures with Solvents Using Laser-Induced Gratings.* The Journal of Physical Chemistry B, 2011. **115**(26): p. 8528-8533.

82. Ariunbold, G.O., et al., *Observation of picosecond superfluorescent pulses in rubidium atomic vapor pumped by 100-fs laser pulses.* Physical Review A, 2010. **82**(4): p. 043421.

83. Thompson, J.V., et al., *Pulsed cooperative backward emissions from non-degenerate atomic transitions in sodium.* New Journal of Physics, 2014. **16**(10): p. 103017.

84. Maki, J.J., et al., *Influence of collisional dephasing processes on superfluorescence.* Physical Review A, 1989. **40**(9): p. 5135-5142.

85. Hosseinia, A., *On the use of rotational CARS on polyatomics in time domain*. 2020, Lund University.

86. Rahn, L.A., et al., *Observation of an Optical Stark Effect on Vibrational and Rotational Transitions.* Physical Review Letters, 1980. **45**(8): p. 620-623.

87. Farrow, R.L. and L.A. Rahn, *Optical Stark Splitting of Rotational Raman Transitions.* Physical Review Letters, 1982. **48**(6): p. 395-398.

88. Kiefer, J. and P. Ewart, *Laser diagnostics and minor species detection in combustion using resonant four-wave mixing.* Progress in Energy and Combustion Science, 2011. **37**(5): p. 525-564.

89. Jarnac, A., et al., *Study of laser induced plasma grating dynamics in gases.* Optics Communications, 2014. **312**: p. 35-42.

90. Maine, P., et al., *Generation of ultrahigh peak power pulses by chirped pulse amplification.* IEEE Journal of Quantum Electronics, 1988. **24**(2): p. 398-403.

91. Strickland, D. and G. Mourou, *Compression of amplified chirped optical pulses.* Optics Communications, 1985. **55**(6): p. 447-449.

92.   InnoLas, *Original user Manual, SplitLight 400 and 600*. 2018: InnoLas Laser GmbH.

93.   Spence, D.E., P.N. Kean, and W. Sibbett, *60-fsec pulse generation from a self-mode-locked Ti:sapphire laser.* Optics Letters, 1991. **16**(1): p. 42-44.

94.   Coherent, *Operator's manual, Vitesse diode-pumped, modelocked Ti:Sapphire laser*. Coherent Inc.

95.   Ducasse, A., C. Rullière, and B. Couillaud, *Methods for the Generation of Ultrashort Laser Pulses: Mode-Locking*, in *Femtosecond Laser Pulses: Principles and Experiments*, C. Rullière, Editor. 2005, Springer New York: New York, NY. p. 57-87.

96.   Renk, K.F., *Titanium–Sapphire Laser*, in *Basics of Laser Physics: For Students of Science and Engineering*, K.F. Renk, Editor. 2017, Springer International Publishing: Cham. p. 77-82.

97.   Wall, K.F. and A. Sanchez, *Titanium sapphire lasers.* Lincoln Laboratory Journal, 1990. **3**: p. 447.

98.   Coherent, *Operator's manual Hidra, Ti:Sapphire amplifier with pulse stretcher and compressor*. Coherent Inc.

99.   Conversion, L., *High Energy Travelling-Wsve Optical Parametric Amplifier of White-Light Continuum*. Light Conversion.

100.   Conversion, L., *Near-IR,UV, DUV, VIS generator for High energy TOPAS-Prime series devices*. Light Conversion.